178

HIGH ENERGY NEUTRINO AND ANTINEUTRINO INTERACTIONS IN A NEON FILLED BUBBLE CHAMBER

by

Raymond Beuselinck

A thesis presented for the degree of Doctor of Philosophy of the University of London

The Blackett Laboratory,
IMPERIAL COLLEGE OF SCIENCE AND TECHNOLOGY,
London SW7 2AZ

November 1979

ABSTRACT

High Energy Neutrino and Antineutrino Interactions in a Neon Filled Bubble Chamber.

R. Beuselinck.

Results are presented on the analysis of 1100 neutrino and 270 antineutrino induced charged current events in the energy range 20 - 200 GeV. The data were taken between January and July 1977 by a collaboration between Aachen, Bonn, CERN, Imperial College, Oxford and Saclay (ABCLOS) in the Big European Bubble Chamber (BEBC) filled with a 74% mole Ne/H_2 mixture exposed to the CERN SPS narrow band neutrino beam operating at a transport momentum of 200 $\pm$ 10 GeV/c. BEBC was equipped with a single plane external muon identifier (EMI) having 100% geometrical acceptance for muons of momentum above 5 GeV/c and an electronic efficiency of 97.5%.

The author's work on the EMI on-line software and the technique of momentum improvement of muons using the EMI data in addition to the measurements of the bubble chamber film is described. The production of di-lepton events is interpreted as being due to charm production and decay. Results of a study of the hadronic jets of normal charged current events are presented in terms of evidence for quark properties. Comparison is made with the jet parameterisation of Field and Feynman.

Contents

Figures

1.1 Kinematics of neutrino interactions.

a) Inelastic scattering process. (k,k' are the incident and final lepton 4-momenta, q = k-k', p = target 4-momentum, θ = laboratory scattering angle of the lepton.)

b) Kinematic boundaries for neutrino interactions showing lines of constant x (= $q^2/2M_N\nu$) and constant hadronic mass.

2.1 General features of the SPS narrow band neutrino beam line.

2.2 Bending and focussing elements of the narrow band neutrino beam.

2.3 Correlation of event energy with distance from the beam axis. The solid curves show the expected correlation between event energy and radial displacement in BEBC for the two cases of ν_π and ν_K events. The dotted curves indicate the regions in which 95% of the events should lie. The points show the values obtained for the CC data sample after correction for missing neutral energy.

2.4 Neutrino beam spectra (arbitrary units).

a) Narrow band ν beam from 200 GeV/c parents.

b) Wide band ν and $\bar{\nu}$ beams from 400 GeV/c primaries.

3.1 a) Fractional momentum error of measured tracks.

b) Residuals of measured tracks.

3.2 Vertex type definitions used in the GST representation of the data.

4.1 Location of the External Muon Identifier (EMI).

4.2 Arrangement of individual EMI chambers.

a) Location and orientation of different types of EMI chamber. Chamber types A,B and C are respectively low resolution, medium resolution and high resolution.

b) Relative spatial resolution of the three EMI chamber types.

4.3 Orientation of the sense planes in an EMI chamber.

4.4 Correlation of EMI main buffer and individual chamber buffers for a hypothetical beam spill.

4.5 EMI main buffer - chamber buffer synchronisation.

4.6 Relationship of separate tasks in the EMI on-line software.

4.7 Main features of the EMI voltage monitoring hardware.

4.8 EMI monitoring system control codes.

4.9 EMI monitoring reference table format.

4.10 General flow chart of EMI voltage monitoring program.

4.11 Monte-carlo prediction of false dimuons due to CC events with a hadron wrongly identified as a muon.

a) Neutrinos

b) Antineutrinos

4.12 Variation of momentum error $\Delta p/p^2$ ($\equiv\Delta(1/p)$) with track length for tracks leaving the visible chamber volume.

4.13 Final corrected muon momentum versus initial well measured muon momentum for through-going tracks above 40 GeV/c whose momenta have been shifted to simulate a measurement of only 50 cm of track length according to $1/p_1 = 1/p_o + \Delta 1/p_1$, $\Delta 1/p_1 = 0.007$.

4.14 As for 4.13 with $1/p_1 = 1/p_o - \Delta 1/p_1$.

4.15 As for 4.13 for tracks above 5 GeV/c.

4.16 As for 4.13 with $p_1 = p_o$, $\Delta p_1 = \Delta p_o$.

4.17 Results of the Momentum correction technique for muons in the CC data sample with initial momentum error, $\Delta p > 10$ GeV/c.

a) Δp versus p before correction.

b) Δp versus p after correction.

5.1 Possible production mechanisms for di-lepton events.

a) Neutral heavy lepton production.

b) Direct production of W boson by electromagnetic process.

c) Production and decay of a charmed hadron.

5.2 a) Effective mass distribution of the two muons for opposite sign dimuon events.

b) Momentum of leading muon versus the momentum of the additional lepton.

c) Visible energy of the di-lepton events.

d) Momentum of the second lepton versus the azimuthal angle difference of the two leptons in a plane perpendicular to the beam direction.

5.3 Transverse momentum distributions of the leptons with respect to the sum of the measured hadrons. (Note the differing horizontal scales in a) and b)).

a) Leading muon. The dotted histogram is the distribution obtained from all CC events normalised to the same number of entries.

b) Second lepton. The dotted histogram is the distribution from CC events of the transverse momentum of individual hadrons with respect to the sum of the measured hadrons.

5.4 x and y distributions of opposite sign di-lepton events. The dotted histograms are the corresponding distributions for CC events.

a) y distribution for neutrinos.

b) y distribution for antineutrinos.

c) x distribution for neutrinos.

d) x distribution for antineutrinos.

6.1 Quark jet generation scheme of Field and Feynman.

6.2 Cos(θ) distribution of protons in the lab frame. (θ is the angle between the proton momentum and the measured hadron direction).

a) Momenta less than 300 MeV/c.

b) Momenta greater than 300 MeV/c.

6.3 Prodution of oppositely moving jets in the Breit frame.

6.4 Momentum of the forward jet in the Breit frame versus $\sqrt{Q^2}$.

a) Neutrinos.

b) Antineutrinos.

6.5 Forward jet momentum in the Breit frame.

a) Neutrinos.

b) Antineutrinos.

6.6 Distribution of charge in the forward jet in the Breit frame versus z. ($z_i = 2p_{Li}/\sqrt{Q^2}$ for particle i). The solid curves are the prediction of Field and Feynman.

a) Neutrinos.

b) Antineutrinos.

6.7 Weighted charge distributions in the Breit frame. ($Q_w(p) = \Sigma_i z_i^p q_i$)

a) Neutrinos, p = 0.2

b) Neutrinos, p = 0.5

c) Antineutrinos, p = 0.2

d) Antineutrinos, p = 0.5 .

6.8 As for 6.7 but in the lab frame for events with corrected hadronic energy between 5 and 40 GeV.

Tables.

5.1 Characteristics of multi-lepton events.
The quantities $x_{vis} = Q^2/2ME_H$, $y_{vis} = E_H/E_{vis}$ are based on the measured hadron energy and total energy $E_{vis} = E_H + E_\mu$. $\Delta\phi$ is the difference of lepton azimuths around the neutrino beam direction. $P_{2T\mu\nu}$ is the momentum of the second lepton perpendicular to the μ-ν plane. No μ^-e^- event was found.

5.2 Di-lepton rates relative to CC production.

6.1 Comparison of event charge distribution for neutrino events with the jet model predictions of ref. 39 for a u quark jet. The charges for the data sample correspond to the particles going forward in the Breit frame. A cut of $z \geq 0.1$ is imposed for comparison with the prediction. ($z = 2P_L/\sqrt{Q^2}$).

6.2 As for 6.1 but for antineutrino data and d quark jet predictions.

6.3 Comparison of weighted charge predictions of ref. 39 with results obtained in the Breit frame forward jet and for tracks in the lab frame in events with $5 \leq E_H \leq 40$ GeV both with and without a z cut. ($Q_W(p) = \sum_i z_i^p q_i$. In the lab frame $z_i = E_i/E_H$).
a) neutrinos.
b) antineutrinos.

CHAPTER I

I.1 Introduction

A collaboration between Aachen, Bonn, CERN and Oxford (ABCO) was formed in 1974 to study the properties of high energy neutrino and antineutrino interactions in the Big European Bubble Chamber (BEBC). The collaboration proposed experiments using the CERN SPS narrow band and wide band neutrino beams in BEBC filled with a Ne/H_2 mixture and pure hydrogen respectively. The principal physics aims of the narrow band experiment were to measure the cross-sections for neutrino and antineutrino interactions as a function of energy for both charged and neutral current interactions. Also it was proposed to study the distributions of the usual inclusive variables used to describe neutrino interactions in order to search for anomalous phenomena, for example the high y anomaly reported by the HPWF group.[1] The complementary aims of the hydrogen proposal were to study the properties of the final state hadrons produced in neutrino interactions with high statistics and high resolution, one of the main hopes being to discover charmed particle production, particularly of charmed baryons, in a bubble chamber.

In 1976 a separate proposal by Imperial College and Saclay to study the differences between neutrinos produced from the decay of pions and kaons at a common energy was approved and the two collaborations were merged to form the ABCLOS collaboration. The Imperial College-Saclay proposal required two narrow band runs at different energies

in order to provide an overlap of events from ν_π and ν_K at a common energy. The low energy run has still not taken place but is now interesting from the point of view of tying down the behaviour of the total cross-section between PS energies and SPS energies.[2,3]

The data reported here were taken between January and July 1977 using the narrow band beam operating at 200 ± 10 GeV/c transport momentum. The integrated SPS intensity at that time was a factor of 10 smaller than that anticipated in the proposals leading to a corresponding reduction in statistics. However, the physics results have generally been better than had initially been expected, notably the determination of the nucleon structure functions and tests of Quantum Chromodynamics (QCD).[4] The collaboration, with the addition of Demokritos, is currently analysing new data at the same energy taken in 1978-1979.

The rest of this Chapter reviews the reasons for doing neutrino physics, kinematic definitions and variables and the standard parton model predictions for neutrino interactions. The following chapters deal with the experimental conditions of the beam and BEBC and the processing of the data from scanning the film to the exchange of data between laboratories. Details of the external muon identifier (EMI) and the author's work on the on-line software and the use of the EMI information to improve muon momentum determination are discussed. Di-lepton events are interpreted as being due to the production and semi-leptonic decay of charmed particles. Properties of the hadronic system

of charged current events are interpreted as evidence for quark properties.

I.2 Reasons for Studying Neutrino Interactions

Knowledge of the properties of the Weak Interaction come from four sources. They are : the decay of stable particles, μ-capture, parity violation experiments in atoms and nuclei and neutrino interactions. Of these processes only neutrino interactions allow the study of weak interactions in the high energy ranges of present day accelerators. This study is important for a number of reasons.

It is well known that the "conventional" theory of Weak Interactions involving 4-fermion interaction at a point[5] necessarily predicts a cross-section proportional to the incoming neutrino energy which must violate the unitarity bound. This problem can be solved in a renormalizable gauge theory[6] where the weak interaction proceeds by the exchange of a massive virtual intermediate vector boson. At sufficiently high energies the effect of the propagator term must become apparent and the intermediate vector boson should eventually be observed (though current estimates of the mass make it more likely to be discovered in colliding beam machines).

In present day weak interaction theory the leptonic vertex is believed to be understood, allowing the interaction at the hadronic vertex to be written as a structure function depending on only two invariants constructed from the target and current momenta and the spin state of the intermediate vector boson. This situation is much simpler than that

occurring in hadron-hadron collisions where the observed final state particles can come from either of two vertices taking part in strong interactions. Thus neutrino interactions are a good place to probe the structure of hadrons.

The unified gauge theory of Weinberg and Salam[6] predicted the existence of neutral current interactions. These were subsequently discovered in neutrino interactions[7] and more recent experiments have attempted to determine the space-time structure of the neutral current.

One may also expect to observe new thresholds for production of heavy quarks at higher energies. Such contributions are expected to add an extra term to the effective Lagrangian appearing first at low x values and high y corresponding to production off the quark-antiquark sea just above threshold. (y and x are the usual scaling variables defined in section I.3 below). Antineutrino interactions are most suitable for looking for these effects due to the suppression of the valence quark contribution at high y.

I.3 Kinematics of Neutrino Scattering

The general deep inelastic neutrino scattering process is illustrated in Fig. (1.1a). Here k and k' represent the 4-momenta of the incident and scattered lepton, and q and p the 4-momenta of the exchanged vector boson and target nucleon respectively. In present weak interaction theory the matrix element for such a process can be written as the product of two currents for the leptonic and hadronic

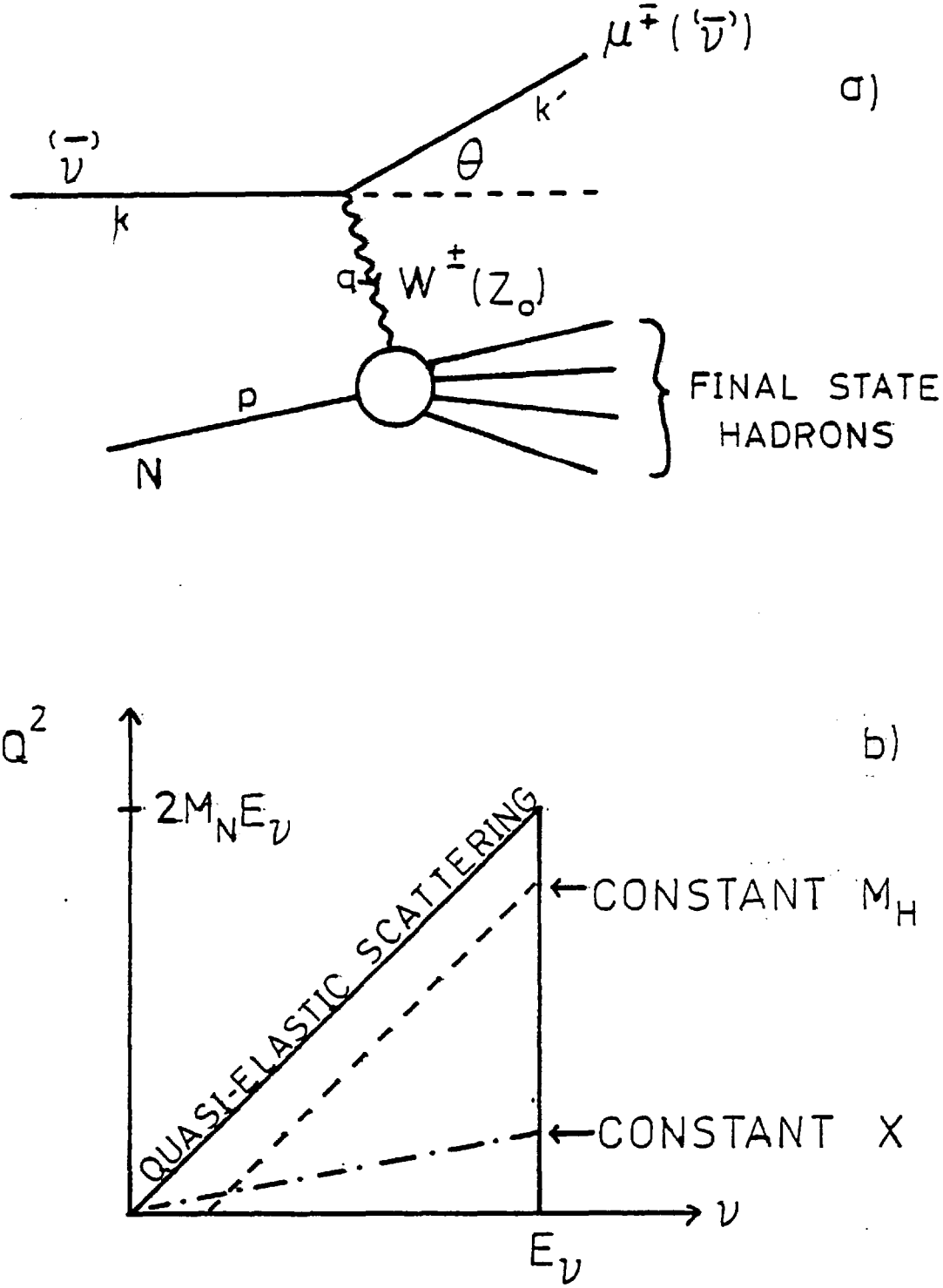
a)
$\mu^{\mp}$ ($\bar{\nu}$)
k'
θ
$\overset{(-)}{\nu}$
k
q
$W^{\pm}$ (Z_o)
p
N
FINAL STATE HADRONS
b)
Q^2
$2M_N E_\nu$
QUASI-ELASTIC SCATTERING
CONSTANT M_H
CONSTANT X
ν
E_ν

FIG. 1.1

vertices with an additional propagator factor for the exchanged boson. Thus the unknown properties of the hadronic vertex can be factorized out and can only depend upon the 4-vectors q and p and the spin states of the current and nucleon. Two Lorentz invariants can be constructed from q and p. They are normally chosen as:

$$Q^2 = -q^2 = -(k - k')^2 \quad , \tag{1.1}$$

$$\nu = \frac{p.q}{M_N} \quad , \tag{1.2}$$

where M_N is the nucleon mass. In the limit of zero lepton masses and when no polarizations are observed the differential cross-section for charged current interactions can be written in terms of these invariants and three factors, $W_i(Q^2,\nu)$, as :

$$\frac{d^2\sigma^{\nu,\bar{\nu}}}{dQ^2 d\nu} = \frac{G^2}{2\pi} \cdot \frac{E_\mu}{E_\nu} \left[2W_1^{\nu,\bar{\nu}} \sin^2\frac{\theta}{2} + W_2^{\nu,\bar{\nu}} \cos^2\frac{\theta}{2} \mp W_3^{\nu,\bar{\nu}} \frac{E_\nu + E_\mu}{M_N} \sin^2\frac{\theta}{2} \right], \tag{1.3}$$

where G is the Fermi coupling constant and E_ν, E_μ and θ are respectively the laboratory energies of the incoming neutrino and outgoing muon and the laboratory scattering angle of the muon. From Equations (1.1) and (1.2) it can be seen that :

$$\nu = E_\nu - E_\mu \quad , \tag{1.4}$$

the energy transfer in the laboratory frame, and the invariant mass of the hadronic final state is given by :

$$M_H^2 = (p+q)^2 = M_N^2 + 2M_N\nu - Q^2 \quad . \qquad (1.5)$$

I.3.1 The Scaling Hypothesis

Bjorken conjectured[8] that at very high energies (Q^2, $\nu \to \infty$) any intrinsic masses become negligible and the cross-sections should not depend on them; they should be independent of scale. Therefore the structure functions, W_i, should become independent of Q^2 and ν and depend only on some dimensionless variable. He took as the appropriate variable :

$$x = \frac{Q^2}{Q^2(\nu)_{max}} = \frac{Q^2}{2M_N\nu} \quad , \qquad (1.6)$$

and predicted that as Q^2, $\nu \to \infty$ with x remaining finite :

$$M_N W_1(Q^2,\nu) \to F_1(x) \quad , \qquad (1.7a)$$

$$\nu W_2(Q^2, \nu) \to F_2(x) \quad , \qquad (1.7b)$$

$$\nu W_3(Q^2, \nu) \to F_3(x) \quad . \qquad (1.7c)$$

In currently accessible energy ranges scaling is only an approximation to the behaviour of the structure functions.[4]

Fig. (1.1b) shows the allowed kinematic region for the process described by Fig. (1.1a) in terms of the variables Q^2 and ν. From Equation (1.5) the maximum possible Q^2 for a given value of ν occurs when $M_H = M_N$ and the reaction is quasi-elastic. This corresponds to $x = 1$ in Equation (1.6).

For a constant value of M_H events lie on a line parallel to the boundary joining $Q^2 = 0$ and $Q^2 = 2M_N E_\nu$. From Equation (1.4) :

$$\nu_{MAX} = E_\nu \quad , \tag{1.8}$$

and we can define another dimensionless variable, y, by :

$$y = \frac{\nu}{\nu_{MAX}} = \frac{E_\nu - E_\mu}{E_\nu} \quad . \tag{1.9}$$

Assuming the validity of the scaling hypothesis and using Equations (1.6) to (1.9), Equation (1.3) can be re-written in terms of x and y and the dimensionless structure functions $F_i(x)$ as :

$$\frac{d^2\sigma}{dxdy} = \frac{G^2 M_N E_\nu}{\pi} \left[xy^2 F_1(x) + (1-y) F_2(x) \mp (y - \frac{y^2}{2}) x F_3(x) \right], \tag{1.10}$$

where a term involving $\frac{M_N}{S}$ is neglected ($S = (p+k)^2$).

I.4 The Parton Model

The parton model was originally proposed by Feynman[9] in order to explain the apparent scaling observed in deep inelastic electron scattering. In this model a nucleon is supposed to consist of a number of quasi-free point constituents which, being points, give rise to no scale in scattering processes.

If a nucleon is assumed to consist of n partons where m_i is the mass of the ith parton and ζ_i is the fraction of the

longitudinal momentum of the nucleon which it carries, then its 4-momentum can be written as :

$$P_i = (\sqrt{(\zeta_i p)^2 + p_{Ti}^2 + m_i^2}, \underline{p}_{Ti}, \zeta_i p) \quad , \tag{1.11}$$

where p is the total momentum of the nucleon. If no other constituents are involved then the ζ_i and $\underline{p}_{Ti}$ must satisfy the following relations :

$$\sum_{i=1}^{n} \zeta_i = 1 \quad , \tag{1.12}$$

$$\sum_{i=1}^{n} \underline{p}_{Ti} = \underline{0} \quad . \tag{1.13}$$

If $\zeta_i p$ is large compared with the parton masses and transverse momenta Equation (1.11) becomes :

$$P_i = (\zeta_i p, \underline{0}, \zeta_i p) \quad . \tag{1.14}$$

An important relation can be seen by examining a collision in the Breit frame of the current and parton. This frame is defined as that in which the momentum of the scattered parton is reversed and its magnitude is unchanged, i.e. :

$$\underline{p}_i + \underline{p}_i' = 0 \quad . \tag{1.15}$$

If we neglect any change in the parton mass then the energy

of the parton is also unchanged in the Breit frame and :

$$p_i' = (\zeta_i p, \underline{0}, -\zeta_i p) \quad . \tag{1.16}$$

Thus from (1.14) and (1.16) the momentum transfer, q, is given by :

$$q = p_i - p_i' = (0, \underline{0}, 2\zeta_i p) \quad . \tag{1.17}$$

Therefore:

$$Q = |\underline{q}| = 2\zeta_i p \quad . \tag{1.18}$$

The 4-momentum of the nucleon is given by :

$$p_N = (\sqrt{p^2 + M_N^2}, \underline{0}, p) \quad , \tag{1.19}$$

so using (1.2), (1.17) and (1.19), we have :

$$\nu = \frac{p_N \cdot q}{M_N} = \frac{2\zeta_i p^2}{M_N} \quad , \tag{1.20}$$

and from (1.6) and (1.18) :

$$x = \frac{Q^2}{2M_N \nu} = \zeta_i \quad . \tag{1.21}$$

Hence x represents the fraction of the nucleons momentum carried by the struck parton.

It is usually assumed that the partons are in fact the spin-½ quarks predicted by Gell-Mann and Zweig. Baryons are believed to be composed of three valence quarks with a sea of quark-antiquark pairs. The quarks are supposed to be bound together by the exchange of vector gluons which carry a "colour" quantum number and only couple to the quarks by strong interactions.

I.4.1 The Quark-Parton Model in Neutrino Scattering

The quarks are assumed to couple to the lepton vertex by a first order V-A interaction. Then, analogously to the case for neutrino-electron scattering the differential cross-section for interaction of a neutrino and a quark can be written as :

$$\frac{d\sigma}{d\cos\theta^*} = \frac{G^2 S}{2\pi} \quad , \tag{1.22}$$

in the approximation that all the rest masses can be ignored. Here θ^* is the centre of mass scattering angle and S is the square of the centre of mass energy of the neutrino and quark. The corresponding relation for antineutrino-quark scattering (or neutrino-antiquark scattering) is :

$$\frac{d\sigma}{d\cos\theta^*} = \frac{G^2}{2\pi} \quad \frac{S}{4} \quad (1 - \cos\theta^*)^2 \quad . \tag{1.23}$$

The $(1 - \cos\theta^*)^2$ factor in this case is the result of helicity conservation and the fact that in the limit of zero

mass fermions are observed to couple to one another only in a left-handed state (anti-fermions have right-handed couplings). In the neutrino-quark case the spins of the interacting fermions are opposed, leading to no preferred orientation and an isotropic angular distribution, whereas in the neutrino-antiquark case the spins are aligned in the same direction requiring a total angular momentum of one leading to the rotation matrix factor which suppresses 180^{o} scattering.

Ignoring the contribution of strangeness or charm changing currents the basic charged current interactions that can occur are :

$$\nu + d \rightarrow \mu^{-} + u \quad , \tag{1.24a}$$

$$\nu + \bar{u} \rightarrow \mu^{-} + \bar{d} \quad , \tag{1.24b}$$

for neutrinos, and :

$$\bar{\nu} + u \rightarrow \mu^{+} + d \quad , \tag{1.25a}$$

$$\bar{\nu} + \bar{d} \rightarrow \mu^{+} + \bar{u} \quad , \tag{1.25b}$$

for antineutrinos. In the neutrino-quark centre of mass frame :

$$y = \tfrac{1}{2} + \tfrac{1}{2} \cos \theta^{*} \quad , \tag{1.26}$$

hence the differential cross-section formulae (1.22) and (1.23) become :

$$\frac{d\sigma^{\nu d}}{dy} = \frac{G^{2}S}{\pi} \quad , \tag{1.27}$$

$$\frac{d\sigma^{\bar{\nu}u}}{dy} = \frac{G^2 S}{\pi} (1 - y)^2 \quad , \tag{1.28}$$

for the interaction of a neutrino (antineutrino) and a quark. Defining the probabilities of finding an up quark or a down quark in a proton with momentum fraction x as u(x) and d(x), the cross-section for νp scattering is :

$$\frac{d^2\sigma^{\nu p}}{dxdy} = \frac{G^2 S}{\pi} \times \left[d(x) + (1-y)^2 \bar{u}(x) \right] \quad , \tag{1.29}$$

where $\bar{u}(x)$ is the corresponding probability of finding an anti up-quark. The cross-section for scattering from a neutron can be obtained by the use of I-spin symmetry and interchanging the u-quark and d-quark distributions. For an isoscalar target consisting of equal numbers of protons and neutrons the result becomes :

$$\frac{d^2\sigma^{\nu N}}{dxdy} = \frac{G^2 M_N E_\nu}{\pi} \left[q(x) + (1-y)^2 \bar{q}(x) \right] \quad , \tag{1.30}$$

$$\text{and } \frac{d^2\sigma^{\bar{\nu}N}}{dxdy} = \frac{G^2 M_N E\nu}{\pi} \left[\bar{q}(x) + (1-y)^2 q(x) \right] \quad , \tag{1.31}$$

$$\text{where } q(x) = x\,(u(x) + d(x)) \quad , \tag{1.32a}$$

$$\bar{q}(x) = x\,(\bar{u}(x) + \bar{d}(x)) \quad . \tag{1.32b}$$

Equation (1.32) represents the momentum fraction carried by

non-strange quarks and antiquarks. Equations (1.30) and (1.31) can be re-arranged to give :

$$\frac{d^2\sigma^{\nu,\bar{\nu}}}{dxdy} = \frac{G^2 M_N E_\nu}{\pi}\left[(q(x) + \bar{q}(x))(1+\frac{y^2}{2} - y) \pm (q(x) - \bar{q}(x))(y-\frac{y^2}{2})\right]. \quad (1.33)$$

Comparing Equation (1.33) with (1.10) it can be seen that the cross-section fom the quark parton model is of the same form as the general scaling hypothesis cross-section. We have from these equations :

$$2xF_1(x) = F_2(x) \quad . \quad (1.34)$$

This is the Callan-Gross relation[10] and is a consequence of the fact that the partons are assumed to be spin-½ particles. Also :

$$F_2(x) = q(x) + \bar{q}(x) \quad , \quad (1.35)$$

which implies that :

$$\int_0^1 F_2(x)\, dx \quad ,$$

represents the fraction of the nucleon momentum carried by quarks and antiquarks. This integral is experimentally found to be ~ 0.5 and it is assumed that the rest of the momentum is carried by gluons. Finally we have :

$$-x F_3(x) = q(x) - \bar{q}(x) \quad , \quad (1.36)$$

$$\text{hence} \quad -\int_0^1 F_3(x)\,dx = \int_0^1 \left[q(x) - \bar{q}(x) \right] \frac{dx}{x} \quad , \tag{1.37}$$

measures the difference in the number of quarks and antiquarks in the nucleon, i.e. the number of valence quarks. The prediction $-\int_0^1 F_3(x)\,dx = 3$ is known as the Gross-Llewellyn-Smith sum rule[11]. This relation is difficult to test experimentally, requiring the measurement of the difference of neutrino and antineutrino cross-sections. Also, since there is a large contribution to the cross-section from low x values the requirement of $Q^2 \gtrsim 1\ \text{GeV}^2/c^2$ to satisfy the scaling hypothesis requires very high neutrino energies.

I.4.2 Scaling Violations and QCD

Deviations from the scaling hypothesis and the simple predictions of the quark parton model are expected in Quantum Chromodynamics (QCD), an asymptotically free gauge theory of strong interaction dynamics. Such deviations from the quark parton model can be naively viewed as "radiative corrections" in analogy with the higher order Feynman diagrams of QED. The usual quark parton diagrams are the zeroth order diagrams in QCD.

One may consider by the uncertainty principle that for a given value of Q^2 (Equation (1.1)) the interaction is probing a distance scale $r \sim 1/Q$ which decreases as Q^2 increases. At high Q^2 values one would expect to be sensitive to finer detail, for example the emission by a quark of a gluon before being struck by the intermediate vector boson. This would

lead to the struck quark possessing a lower fraction of the nucleon momentum x than expected on the quark parton model. Thus as Q^2 increases the structure functions F_2 and $x F_3$ would be expected to fall at large x and rise at low x as observed by the ABCLOS collaboration.[4]

The final chapters of this thesis discuss the production of di-lepton events and the charge retention properties of the hadronic system of charged current events in the context of the quark parton model. In particular, the elementary neutrino-quark cross-sections and the concept of the quark-antiquark sea are invoked.

CHAPTER II

EXPERIMENTAL DETAILS

This chapter describes the experimental details of the CERN SPS narrow band neutrino beam and the bubble chamber BEBC with reference to the problems of hadronic energy resolution. The data discussed were taken at the beginning of 1977. At that time BEBC was equipped with a single plane external muon identifier which is described separately in Chapter IV.

II.1 The Neutrino Beam

The main sources of high energy neutrino beams are the decays :

$$\pi^{\pm} \rightarrow \mu^{\pm} + \nu(\bar{\nu}) \quad \text{and}$$

$$K^{\pm} \rightarrow \mu^{\pm} + \nu(\bar{\nu}) \quad .$$

Since these are both two body decays they produce neutrino spectra which are flat with a laboratory range of energies :

$$0 < E\nu/E_{\pi,K} < 1 - m_{\mu}^{2}/m_{\pi,K}^{2} \quad .$$

The largest background to this spectrum comes from the decays :

$$K \rightarrow \pi + \mu + \nu_{\mu} \quad \text{and}$$

$$K \rightarrow \pi + e + \nu_{e} \quad ,$$

which both occur at a level of a few percent. Of the two background decays the first is the more serious since electrons can be readily identified in the bubble chamber and the electron neutrino events removed from the analysis.

II.2 General Features of the Beam

The broad layout of CERN SPS neutrino beam facilities is outlined in Fig. 2.1. For the narrow band beam protons were extracted from the SPS at 400 GeV/c in a short spill of 2ms and steered to the T11 target to produce secondary hadrons. The proton beam strikes the target at an angle of 15 mrad so that any neutrinos produced before momentum and sign selection of the secondaries will not reach the detectors downstream. The secondary hadron beam is momentum selected to $\Delta P/P = 0.05$ at a transport momentum of 200 GeV/c after being accepted into an aperture of 2 mrad in the horizontal and vertical planes and doubly focussed onto a momentum slit. It is finally made parallel to $\pm$ 0.2 mrad and directed towards the detectors. The bending and focussing of the beam is shown schematically in Fig. 2.2.

After formation the hadron beam enters a 300m long evacuated decay tunnel where about 3% of the π's and 32% of the K's decay producing neutrinos. At the end of the decay tunnel there is 400m of shielding composed partly of iron but chiefly rock and earth in order to absorb the remaining hadrons. At various depths in the shielding are pits containing arrays of solid-state counters which measure the

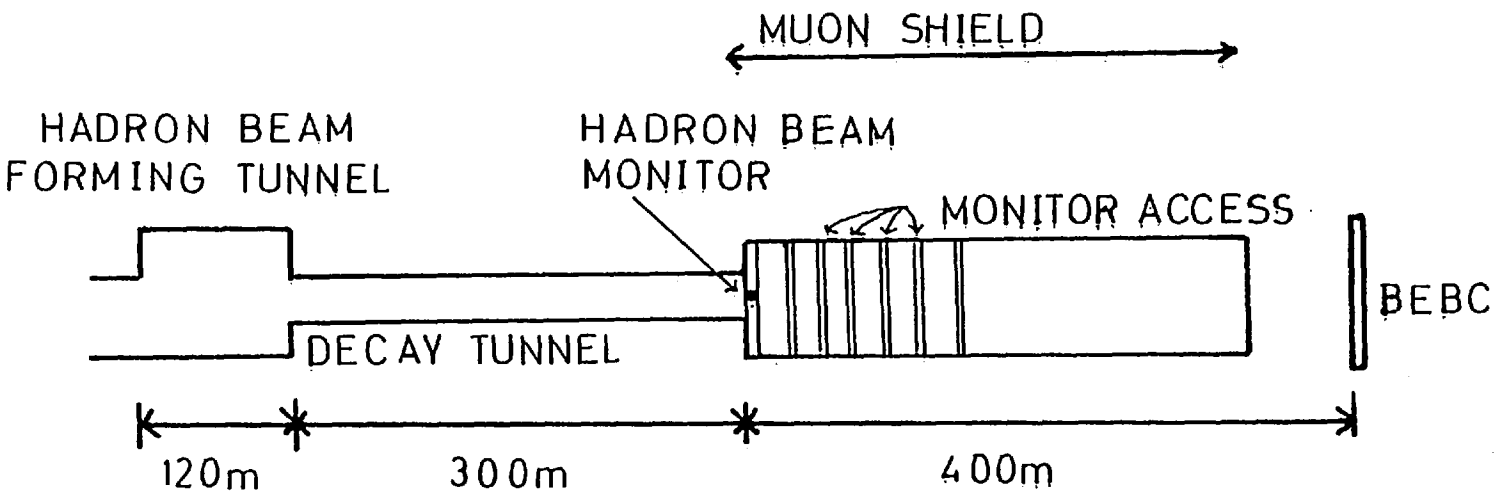

GENERAL FEATURES OF NEUTRINO BEAM LINE

FIG. 2.1

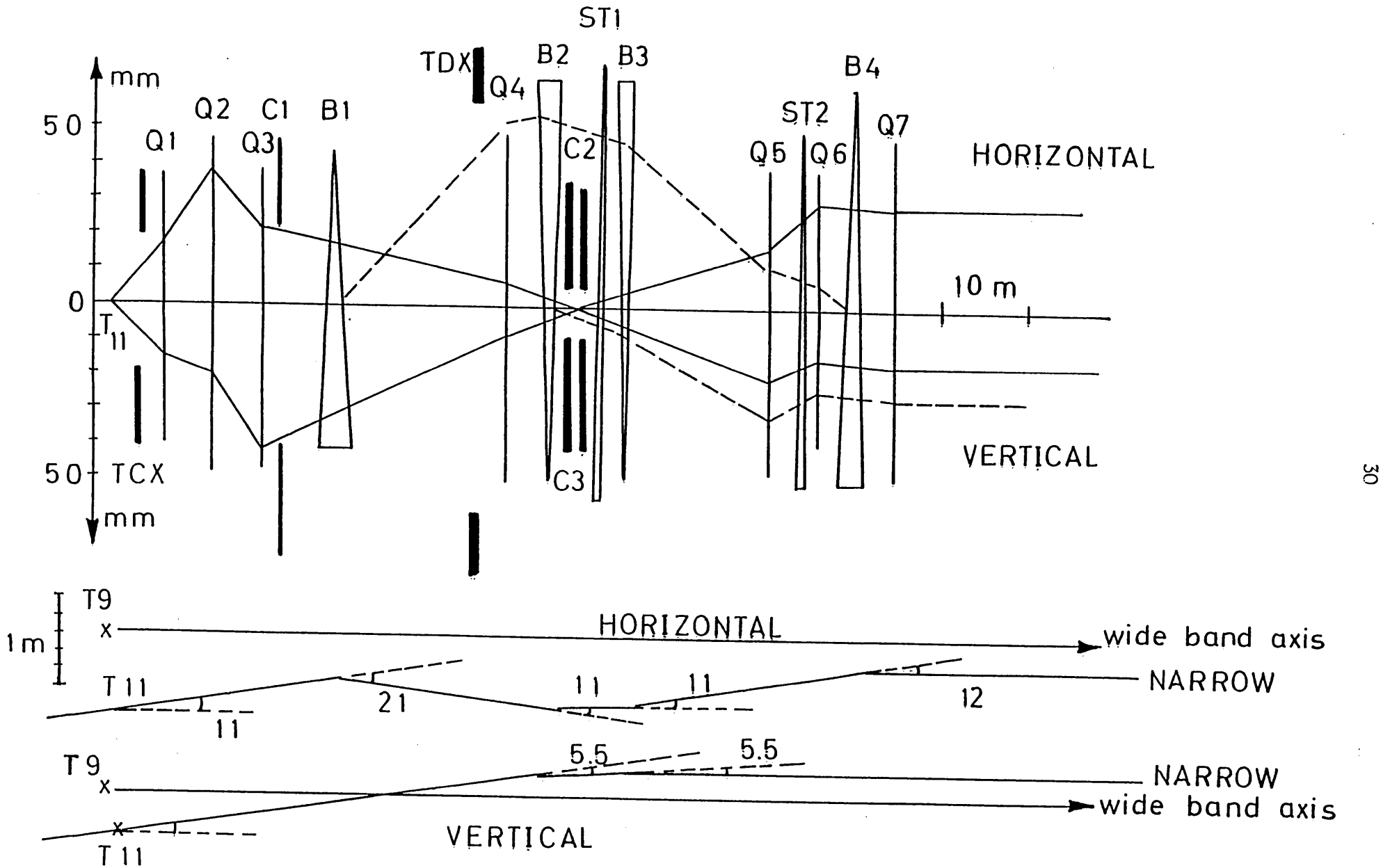
ST1
TDX
B2
B3
B4
mm
Q2
C1
B1
Q4
ST2
Q7
50
Q1
Q3
C2
Q5
Q6
HORIZONTAL
10 m
0
T11
50
TCX
C3
VERTICAL
mm
T9
1m
x
HORIZONTAL
wide band axis
T11
11
21
11
11
12
NARROW
5.5
5.5
T9
x
NARROW
wide band axis
VERTICAL
T11

FIG. 2.2

penetration of the muons produced with the neutrinos at various transverse distances from the beam axis. The detectors in each gap are calibrated by a single moveable detector which may be placed in front of each of the fixed detectors in turn. This is in turn calibrated by counting tracks in nuclear emulsion. The distribution of the muons thus obtained, together with a knowledge of the K/π composition of the beam, allows the absolute neutrino fluxes to be calculated.

Additionally, the total hadron beam current is measured on each SPS pulse by a magnetic induction device, the beam current transformer (BCT). The K/π ratio of the beam is determined by measuring the total light output from a differential Cerenkov counter as a function of gas pressure.

II.3 Neutrino Beam Kinematics

As mentioned above, the two body decay of the π's and K's in the beam leads to a flat energy spectrum for the neutrino beam extending almost from zero to 95% of the hadron energy in the case of the K's and 43% in the case of the π's. This has the advantage that the whole range of neutrino energies can be studied in one experiment. Also the two body decay kinematics mean that the direction of the produced neutrino is precisely related to its energy, which can therefore be inferred by the radial displacement from the beam axis of the event seen in the bubble chamber, subject to the ambiguity between π's and K's. See Fig. 2.3. The uncertainties in this method of determining the neutrino

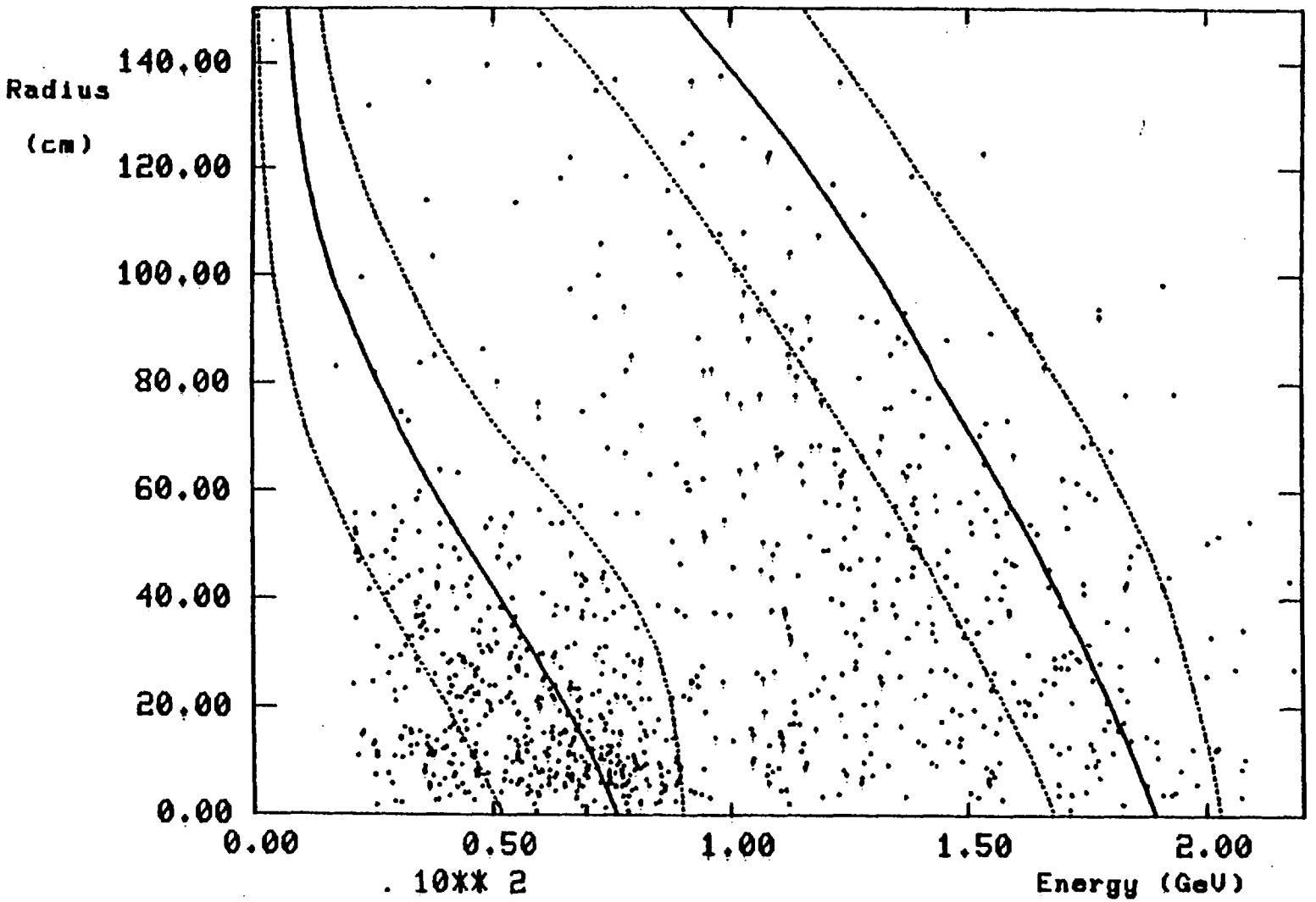
Radius
(cm)
140.00
120.00
100.00
80.00
60.00
40.00
20.00
0.00
0.00
0.50
1.00
1.50
2.00
. 10** 2
Energy (GeV)

FIG. 2.3

energy are introduced by :

(i) the momentum spread of the hadron beam, ± 5%,

(ii) the angular spread of the hadron beam, ± 0.2 mrad,

(iii) the finite length of the decay tunnel.

Fig. 2.3 shows the expected correlations between event energy and radial displacement from the beam axis for π-neutrino and K-neutrino events in BEBC. The dotted lines represent the regions in which 95% of the events should lie. The points show the actual positions of the charged current events whose energies are obtained from the measured energy with a correction for missing neutral hadrons.

II.4 Advantages of the Narrow Band Beam

Fig. 2.4 shows a comparison of the narrow band beam spectrum compared with the wide band horn-focussed beam. It will be seen that the wide band beam has a steeply falling spectrum peaked at about 25 GeV, whereas the narrow band spectrum is flat out to 200 GeV. The narrow band beam therefore has the following important advantages :

(i) Uniform event samples over the full energy range.

(ii) A higher proportion than for the wide band beam of high energy events with

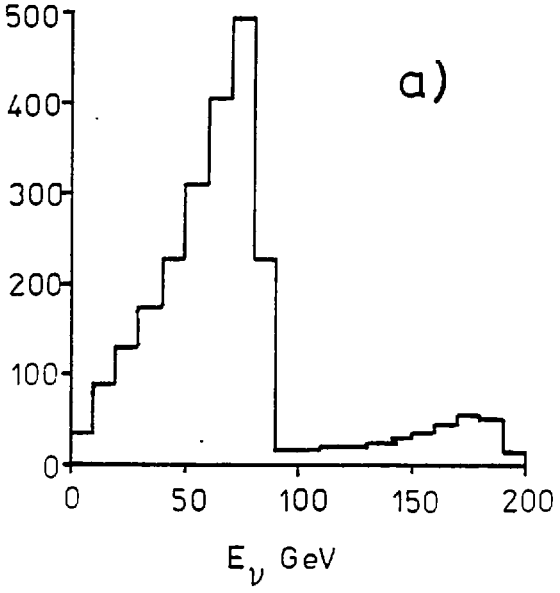
500
400
300
200
100
0
a)
0
50
100
150
200
E_ν GeV

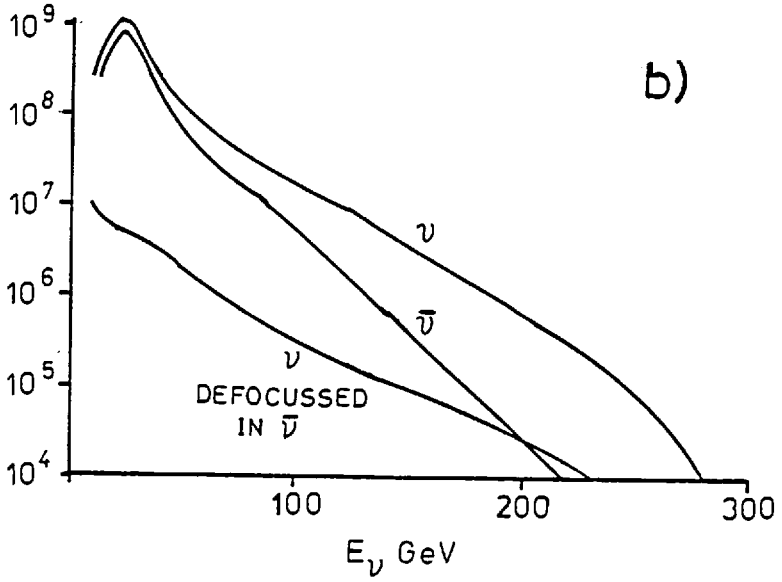
10^9
10^8
10^7
10^6
10^5
10^4
b)
ν
$\bar{\nu}$
ν
DEFOCUSSED
IN $\bar{\nu}$
100
200
300
E_ν GeV

FIG. 2.4

potential new physics information on such topics as multi-lepton production and phenomena related to QCD.

(iii) The flat energy spectrum of the narrow band beam reduces systematic biases in the determination of event energies and thus in cross-section determinations. In addition, the large momentum range of the parent hadron beam in the wide band case means that no correlation between event energy and vertex position exists. For the determination of neutral current cross-sections this is an essential feature of the narrow band beam since the energy of the outgoing neutrino cannot be measured.

II.5 The Bubble Chamber

BEBC, the bubble chamber used in this experiment, is basically a cylinder 3.7m in diameter and 4m in height equipped with four stero views with fisheye optics, the fifth camera port being reserved for observing the conditions of the chamber during running. The chamber is immersed in a 3.5 T magnetic field provided by two superconducting coils to achieve good momentum resolution.

The filling used was a 74% molar Ne/H_2 mixture with a

density of 0.71 gm ml^{-1} giving a radiation length of 42cm and an interaction length of 140cm. A fiducial volume of $17m^3$ (target mass 12 tonnes) was chosen such that the minimum downstream path from an interaction was 50cm. Under these conditions an average momentum resolution of $\Delta P/P = 4\%$ was obtained for tracks of 100 GeV/c momentum. In addition, BEBC was equipped with a single plane external muon identifier which was also employed to improve upon the bubble chamber measurements of the identified muons as described in Chapter IV.

The heavy Ne/H_2 filling used for BEBC has a number of advantages and disadvantages. The principal advantage over hydrogen or deuterium is the higher event rate due to the greater density. The other main advantages are the ability to convert a large fraction of the neutral hadronic energy of events in the form of gammas and neutron stars and the superior particle identification. In particular, electrons are identified with high efficiency allowing accurate separation of electron-neutrino induced events as well as events with the charm signature of $\nu + N \rightarrow \mu + e + X$. By the same token converted gammas are very rarely ambiguous with V^o's. Such ambiguity normally only arises for gammas produced near the downstream end of BEBC such that the electron tracks leave the chamber before exhibiting any identifying characteristic. In addition, the short interaction length means that many hadrons will undergo a secondary interaction within the chamber thus reducing the number of candidate muon tracks.

Unfortunately these advantages can also be disadvantages at the same time. Many of the high energy gammas which are converted in BEBC undergo large energy losses by Bremsstrahlung processes which can lead to the build up of a large electromagnetic shower obscuring the event and reducing the measureable length of the electron tracks from the initial primary gammas. A large gamma shower can also make searching for V^o's very difficult. Hadrons also suffer similar problems. Since the interaction length in the heavy neon mix is so short tracks will often re-interact before providing sufficient length to determine their momentum or even their charge. In these cases the secondary tracks from the interaction must be measured to obtain a lower estimate of the energy of the incoming track. These secondary tracks can themselves greatly increase the confusion in an event. As well as multi-prong inelastic scatters many elastic two-prong scatters occur where the recoil track is so short that it is not seen. These scatters appear just like kinks due to strange particle decay in flight which means that such kinks cannot be used to identify strange particles as for hydrogen filled chambers. Because the neon nucleus may fragment after a neutrino interaction with one of the nucleons the constraint of charge balance at the event vertex is automatically restricted to the statement that the net charge of an event must be greater than or equal to zero.

II.6 Hadronic Energy Resolution

The greatest advantage of bubble chambers over

electronic detectors in neutrino experiments is the ability to study the details of the hadronic system. Massive calorimeter devices are only capable of measuring the total hadronic energy and its direction. They are, however, much better at measuring the total energy of the events at high energy since they are capable of depositing almost all of it within the apparatus.

In BEBC filled with neon we can measure essentially all the charged energy and estimate that we measure 83 ± 3% of the total hadronic energy on average with an r.m.s. spread of 20%. Thus in estimating the total energy of an event the hadronic energy is multiplied by a correction factor of 1.2. The loss derives not so much from the escape of neutral hadrons and gammas from the chamber but from the difficulty of positively associating them with the primary vertex when it is far upstream. The danger, particularly with gammas, is that of double counting (i.e. measuring Bremsstrahlung gammas from primary gammas whose energy has already been determined).

The energy loss factor has been determined in two different ways. The first method is to study the imbalance in transverse momentum within the plane defined by the incoming neutrino and the outgoing muon for charged current events. With the assumption that the direction of the measured hadrons lies close to the direction of the total hadron vector the measured hadronic momentum vector can be scaled up to balance transverse momentum. However, due to Fermi motion in the neon nucleus this method cannot provide an individual correction on

an event-by-event basis but can only provide an average correction determined from a large number of events where the random effects of fermi motion cancel out. The second method was to measure a sample of events of the type $\pi^- + N \rightarrow X$ at 70 GeV/c incident π^- momentum in BEBC filled with the same mixture. It was found, applying the same measurement criteria as for neutrino events, that on average the charged energy accounted for about 2/3 of the total and that about 50% of the neutral energy was missed in agreement with the results from transverse momentum balance. Taking this energy loss into account the CC event sample was found to be in good agreement with the theoretical narrow band beam spectrum.

CHAPTER III DATA PROCESSING

III.1 Scanning

The film was initially double scanned on at least two views for events occuring anywhere within the visible volume of BEBC. Isolated one prong events were not scanned for due to the difficuly in spotting them which would result in an unreliable scanning efficiency.

An event with at least two prongs was recorded as a neutrino event if it satisfied the following criteria :

(1) There should be at least one minimum-ionizing track going forward or sideways from the event vertex and having a radius of curvature greater than a template the size of the BEBC piston, corresponding to a momentum of 1 GeV/c in the beam plane, or :

(2) if there is no track as in (1) then there should be an associated e^+e^- pair with at least one track straighter than a half-piston template.

(3) The events should not be a background event of the type X or Y as described below.

(4) There should not be a wallon on the frame in the entry region of the beam.

A wallon is defined here to be three or more incoming tracks, at least one of which must kink or interact, whose entry points must be within a distance of one schotchlite

panel horizontally and vertically (28 cm). If any wallon is found in the most upstream quarter of the chamber wall any other event on that frame is ignored and only the presence of the wallon is recorded. If a wallon is found in any other region, for example in the side wall, then other events occurring in the chamber volume may be recorded if they are unassociated with the wallon.

In addition to wallons, three other types of background event are recorded.

An X type event is one in which a track is clearly seen to be incoming to the event vertex by a delta ray indicating its direction.

A Y type event has a fast backward track which is straighter than a "3 x piston" template but whose direction is not signed by a delta ray. The track must lie within $\pm 75^{o}$ of the backward direction.

A Z type event is one which fails to satisfy the energy requirement described above for a neutrino event, i.e. it does not have a fast forward track or high momentum gamma associated to it.

For any frame having a genuine neutrino event any Z type event occurring on the frame is also recorded in full detail as an associated event as are one prong or multi-prong stars and V^{o}'s. V^{o}'s may also be considered as possible two-prong neutrino events. The linking or exclusion of associated vertices is performed at the analysis stage.

After the first two independent scans a check scan

was done under physicist control to compare events found on the previous scans for a determination of the scanning efficiency and also to prepare genuine events for measurement. The overall efficiency for the double scan was found to be 98%.

Preparation of events for measurement consisted of making a tracing of each event and labelling all vertices and tracks to guide the measurers. The nature of the end point of all tracks was also recorded (such as stopping, leaving, interacting etc.). For short tracks which interact before showing a measurable curvature the secondary tracks from the interaction were also drawn and labelled for measurement to gain a lower estimate of the momentum of the interacting track. In addition a photographic print was made at this stage and kept with the drawings for reference.

III.2 Scanning for Direct Electrons

All frames possessing neutrino events were re-scanned to look for direct electrons (of either sign) from the primary vertex. This was done to find events with the charm signature of a muon and electron (μ-e events) and to estimate the K_{e3} decay contribution to the event sample. In addition to searching for direct single electrons three sources of background were noted :

(1) Dalitz pairs from π^0 or η^0 decay at the vertex;

(2) close in pairs converted within 3 cm from the primary vertex on a Bessy scanning table

(18 x magnification);

(3) delta rays with diameter greater than 1 cm within 6 cm of the primary vertex.

A separate scan for primary gammas was done to determine the electron identification efficiency in BEBC (i.e. the efficiency with which an electron produces a characteristic identifier). The following identifiers were used to define an electron :

(1) sudden change of curvature;

(2) production of a Bremsstrahlung gamma pointing tangentially to the track at a kink;

(3) trident production with the e^+e^- pair taking at least 10% of the track's energy;

(4) a delta ray taking at least 50% of the electron's energy;

(5) positron annihilation accompanied by one or two converted gammas.

The identifier of spiralization was not used as a sufficient identifier alone to avoid confusion with unseen π-μ-e decays.

Analysis of the results of the gamma scan show that the above mentioned criteria for electron (positron) identification lead to an identification efficiency of 90 ± 5% for tracks

above 1 GeV and up to $\sim$ 10 GeV energy. For tracks between 0.3 and 1 GeV the figure is 85 ± 5%. From the original double scan of the film and the special electron scan the overall efficiency for finding prompt electron candidates is estimated to be 95 ± 5%.

As well as satisfying one of the criteria for identification a candidate electron track must also be clearly visible right down to the primary vertex on at least one view. Very often there exists a "distance of confusion" from the primary vertex within which individual tracks cannot be followed. The rejection of electron candidates on such events leads to a loss of events rather than a background source. An analysis of the distribution of distances of confusion leads to an estimated correction factor for lost events of 1.3 ± 0.2. This, together with the scanning and identification losses, leads to an overall correction factor for electrons of 1.5 ± 0.3.

Details of muon-electron events found may be seen in Table 5.1 together with dimuon events.

III.3 Measuring

At Imperial College all measurements were done on a film-plane digitizing manual measuring machine controlled by a PDP8L mini-computer which was in turn linked to a PDP10 computer. This system allowed geometrical reconstruction on-line of each track as it was measured. Due to the complexity of the events in the heavy neon-hydrogen

mixture of BEBC and the time needed to measure each event it was necessary to have the detailed checks provided by on-line geometry at the measuring stage in order to avoid endless failures and re-measures.

Geometrical reconstruction of the events was performed by standard HYDRA hydrogen geometry on-line and by HYDRA heavy liquid geometry off-line. Events were measured on a frame by frame basis such that multiple events on a single frame were measured as a single, large multi-vertex event. This was done to avoid the problem of associating different neutral vertices by eye at the scanning stage and also because the EMI program operates on a frame by frame basis. Communication with the measurer is performed by a control program which receives and outputs messages via a teletype and which does the input and output operations on the measurements. Under this system each measuring machine has its own associated control program but the on-line geometry program OLGA is shared and may be accessed by each measuring machine independently.

In the heavy liquid mixture most tracks possess a clear means of identification at an end point, such as an interaction, kink or decay. This fact, together with a heavy comment system, has been used to advantage in the measuring procedure. Normally each track is measured individually on three views along with a corresponding point at the end. These measurements are then presented to the on-line geometry program which performs the reconstruction for that single track. The results of the reconstruction

are returned to the control program and thence to the measurer. If the measurements are acceptable they are written out to disk on a temporary file for that event. If not, then the program requests a re-measure and causes the PDP8L computer to drive the film stages to point to the item to be re-measured. Only after each item has been measured correctly does the program move onto the next. This procedure and the use of corresponding points where possible greatly reduces the amount of work which must be done by the track matching processors of HYDRA which would otherwise have great difficulty with the many fast, close tracks characteristic of high energy events.

Additional features allow the measurement of multi-prong secondary interactions and one arm gammas or Compton electrons. Also on confused events tracks may be measured backwards from the end point where the track is clear. The measurer is in all cases guided along the track by a second-order extrapolation from the previous measured points by the control program which drives the stages.

III.4 Post-Measurement Checking and Processing

After measurement the resulting output was processed by HYDRA off-line geometry which performed kinematical reconstruction of measured V^0's and gammas, associating them where possible to primary or secondary vertices. Standard mass hypotheses for primary charged tracks (e.g. p, π, k, μ) were also generated where appropriate. No attempt was made at this stage to link associated

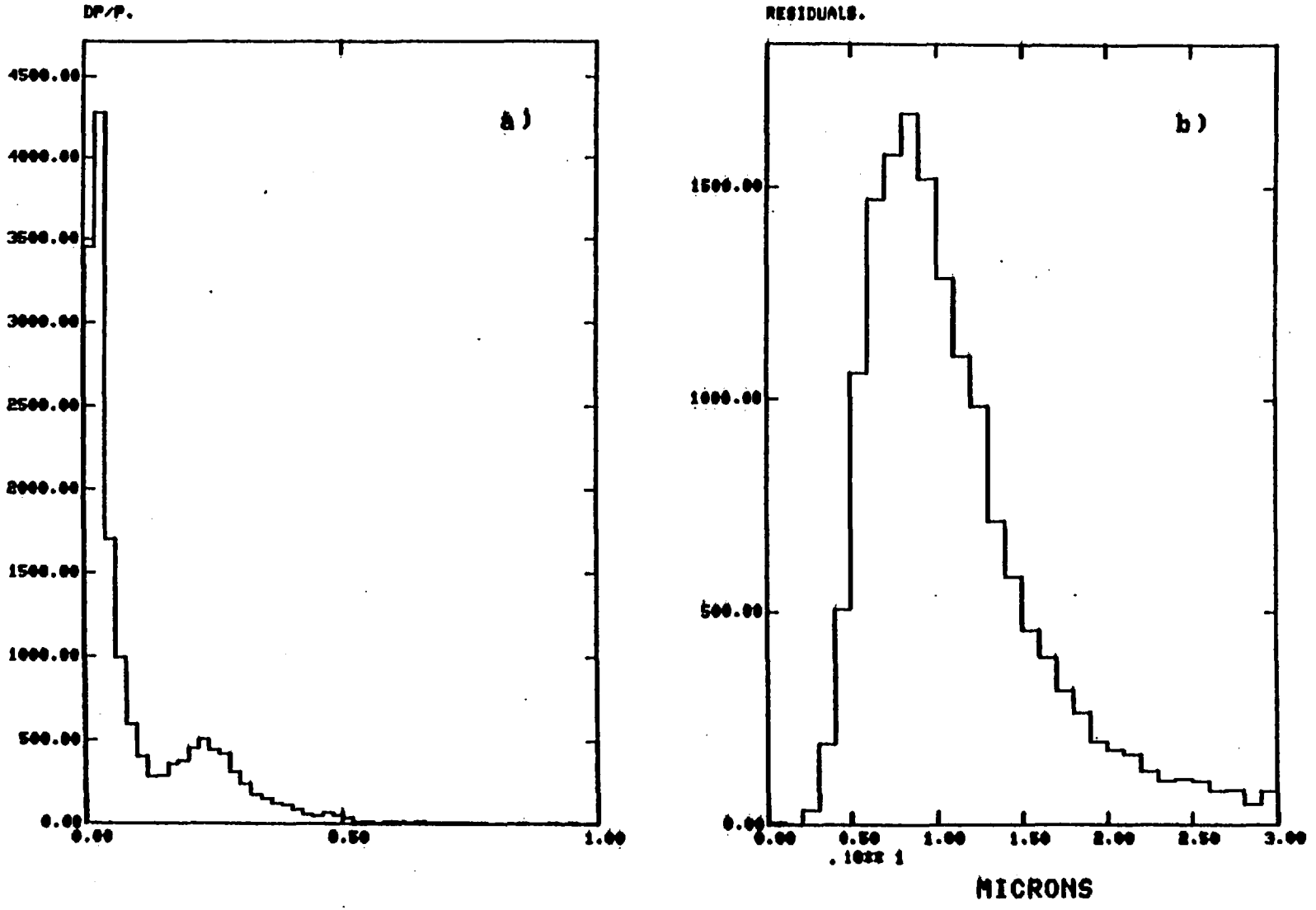
DP/P.
4500.00
4000.00
3500.00
3000.00
2500.00
2000.00
1500.00
1000.00
500.00
0.00
0.00
0.50
1.00
a)
RESIDUALS.
1500.00
1000.00
500.00
0.00
0.00
0.50
1.00
1.50
2.00
2.50
3.00
.1000 1
MICRONS
b)

FIG. 3.1

neutral star vertices to the most upstream primary vertex.

Fig. (3.1) shows the distribution of fractional momentum error ($\Delta P/P$) of tracks after reconstruction by geometry. The peak at 0.25 is due to the electron tracks from gammas which are much more difficult to measure than hadrons due to the problems of Bremsstrahlung and spiralization. Very often only a short section of electron track can be measured and the resulting large errors may cause the kinematic reconstruction of a gamma to fail. In such cases a straight connecting track to the primary vertex is created by simply summing the magnitudes of the measured momenta of the individual tracks.

The results from off-line geometry were then used as input to the EMI off-line program along with the EMI raw data tapes. The output from this program consisted of the original geometry output banks with the EMI results added in additional banks. The operation of the EMI program is described separately in Chapter IV. Printed output which summarized the geometry and EMI results together was used subsequently at the scanning tables along with the drawings made at the check scan stage to verify that the events had been measured correctly and to make decisions on the validity of the muon candidates. A graphical reconstruction of the events was also used to help in spotting any problems with the event reconstruction. The main physicist checks at the fourth scan stage were the following :

(i) All charged primary tracks should have been measured and correctly reconstructed (momentum and error should be reasonable).

(ii) The correct end-type comment should be present (e.g. leaving, interacting, stopping). This is particularly important for the EMI program.

(iii) The secondary tracks from interacting primary tracks with unmeasurable momentum should have been measured.

(iv) Any V^o's should have been correctly measured.

(v) Primary electron tracks should be correctly commented (otherwise the electron hypothesis is not generated by geometry).

(vi) All non-interacting tracks which leave the chamber should be checked for associations to EMI hits and the best candidate selected. In the case of dimuon candidates both tracks should be associated to different hits on the EMI within the same time-slot.

(vii) As much of the primary neutral energy as possible should have been measured (i.e. until an electromagnetic shower makes further measurement impossible).

Events failing the above criteria were sent back for either complete or partial re-measurement. All other events were then classified as being "complete" or "partial". To be considered as complete at least 95% of the visible hadronic energy must have been measured, the remainder being unmeasurable. This assignment is of course largely subjective and is not critical to any analysis so far performed on the data since the energy loss accounted for by the partial events can only make a small contribution to the loss in all events, represented by the global correction factor of 1.2 applied to the measured hadronic energy of every event.

III.5 GST Format for Interchange of Data

The final form in which it was chosen to interchange data between the collaborating laboratories was a slightly modified form of the CERN Geometry Summary Tape format (GST) which has previously been used in Gargamelle neutrino experiments.[12] In this format the data is represented as a series of 80 column card images, the detailed specifications of which can be found in Ref. (12). In the later stages of the experiment the GST was converted to a PATCHY4 PAM-file and subsequent minor corrections to individual events were made by adding correction cards to a standard cradle. The merged geometry and EMI information were converted into GST form by a program supplied by CERN.

EXAMPLES OF VERTEX TYPE DEFINITIONS

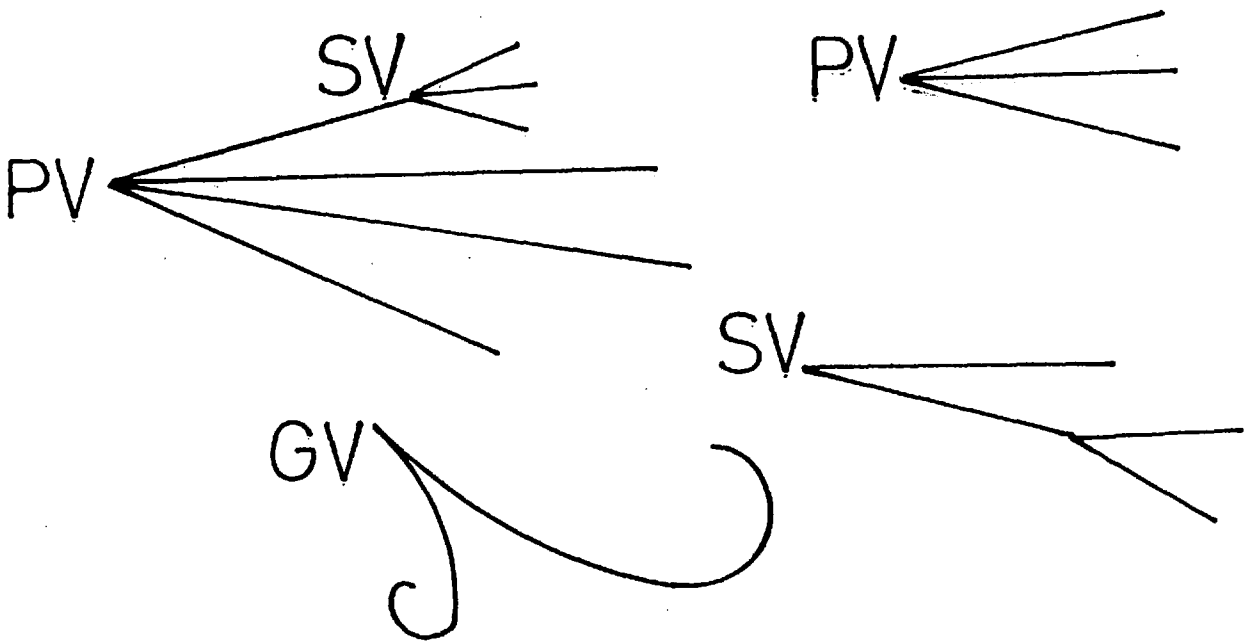

FIG. 3.2

III.6 Criteria applied in the Production and Analysis of the GST

At this point some discussion is relevant of the criteria applied in the production, editing and analysis of the GST. One of the main problems in analysing the data is to decide on the association or exclusion of several neutral vertices on the same frame. Fig. (3.2) illustrates this problem and the vertex definition criteria applied. Any vertex which could have resulted from a neutrino interaction is given a primary (PV) classification. This applies also to neutron star vertices of sufficient energy. Apart from isolated e^+, e^- tracks and gamma vertices (GV), all other vertices - V^o origins and charged track end points - are classified as secondary vertices (SV). V^o vertices may also be classified as PV. All PV and SV vertices may be considered as candidate origins in V^o and gamma fitting so the SV vertices of stopping protons are suppressed.

III.7 Treatment of End Point Comments

As mentioned in Section III.3 on measuring the end points of tracks are measured and commented where possible (the end point must be visible on at least two views and the track must not turn through an angle greater than 120^o from beginning to end). The following definitions and checks apply.

Stop : All hadron mass fits are applied (p, k, π) plus the μ mass fit. If all

hypotheses are incompatible with range the type is changed to "interaction" and the μ hypothesis suppressed. If the end point is found to be on the wall the type is changed to "leaving".

Proton : Only the proton hypothesis is tried. This applies to short tracks too straight to give a momentum from curvature which stop and are heavily ionizing. Segments of track are combined regardless of P_T.

Decay : Observed decay at rest of k, π or μ. Proton hypothesis suppressed.

Capture : Recoil proton seen at the end of a stopping π^-. Only π^- hypothesis tried.

Electron : Definite electron (i.e. at gamma vertices).

Possible electron : Track from a hadronic vertex. Hadron hypotheses are also tried. All such tracks are carefully examined.

Interaction : μ hypothesis is suppressed.

Kink : In general, small angle one pronged interactions are called kinks. The high probability of secondary interactions means that kinks cannot be used as a sign of strange

particle decay as in hydrogen filled chambers. In the case that a kink to be measured past is visible on only one view the position of the kink is signalled by means of a "special kink" button. The geometry program then splits the measurements on the other views at the expected position of the kink and reconstruct each segment separately. The decision to combine the segments or take only the first is made on the basis of the transverse momentum at the kink. If the segments are combined the result is a weighted average of the momentum and error of the individual segments. If the P_T is greater than 100 MeV/c the type is re-named as an interaction and the μ hypothesis suppressed.

III.8 Association of Neutral Vertices

In analysing the events appropriate neutral corrections must be made to neutron star vertices, V^o's and gammas. The problem is the same for the three cases : to determine whether the vertex belongs to the main event at all or whether it is due to a neutron or strange particle incoming from interactions in the shielding upstream of the chamber. If the vertex is associated to the main event the problem is then to decide unambiguously which vertex (PV or SV) it comes from since there are often many secondary interactions which appear equally probable as origins.

The treatment of neutrons differs from that of V^o's

and gammas in that 3C fits to specific origins are attempted in the latter two cases. For each successful fit to an origin a neutral track card and a scan card is output. In the case of V^o's separate cards are output for each mass hypothesis which is successful (K^o, Λ or $\bar{\Lambda}$) and the V^o vertex is classified as a secondary vertex. For gammas there also exists a gamma synthesis card GS which may be used to specify an additional two alternative origins as well as the best one. The analysis program[13] selects the origin for which the fit has the smallest chi-squared in cases of ambiguity and it is up to the physicists checking the events to remove spurious associations as well as ensuring that double counting does not occur (e.g. any gamma pointing to a Bremsstrahlung kink or another gamma whose energy is already measured should be removed). V^o's which fail to fit to an origin are classified as primary vertices and the event category is set to 'V' if a 1C fit is compatible with a V^o mass. For gammas which do not fit to an origin a special label in the range 90 to 99 is put as the best origin on the GS card and a PV card is generated with the same label and the spatial co-ordinates of the gamma vertex.

For neutrons the best vertex is selected by finding the one for which the angle between the supposed line of flight and the sum of the momenta of the outgoing tracks is a minimum. The longitudinal and transverse momenta with respect to the line of flight are calculated and the association is retained provided the longitudinal momentum is greater than zero and the transverse momentum is less

than 5 GeV/c. If the neutron fails these criteria the vertex is discarded unless it satisfies the minimum criteria for inclusion as a separate neutrino event.

CHAPTER IV

THE EXTERNAL MUON IDENTIFIER

IV.1 Introduction

The nature of charged current neutrino interactions is such that identification of the muon coming from the lepton vertex is essential in any physics analysis. It is also desirable since the discovery of neutral current interactions in the Gargamelle bubble chamber in 1973[7] and of dimuon events at FNAL in 1975[14] to be able to identify these types of events. In previous low energy bubble chamber experiments the task of muon identification could be performed adequately from the bubble chamber information alone since only muons could penetrate long distances without undergoing secondary interactions and due to the kinematics of the charged current interaction they also carried off on average half the energy of the events and had high transverse momenta with respect to the final state hadrons. In high energy events however, many of the final state hadrons may leave the visible chamber volume before interacting, and kinematic selection of muons is no use in identifying neutral current events or multi-muon events. Therefore, in experiment WA19/22 the CERN External Muon Identifier (EMI) played an essential role.

In this chapter the operation of the EMI is outlined. General features of the construction and readout system are described. The overall performance of the EMI is discussed in terms of background sources and identification efficiency. The authors work on the on-line program for control of an automatic voltage monitoring system and the implementation and testing of a method

of improving muon momentum measurements using EMI information is described. The construction of the EMI and associated electronics and the monte-carlo background calculation are not the work of the author.

IV.1.1 Principles of Muon Identification

The technique used by the CERN EMI is essentially the same as that used in the EMI at the 15' chamber[15]. The EMI consists of a large detector wall located behind many collision lengths of iron. It is not possible to identify muons on the basis of completely absorbing the hadron shower since too great a thickness of absorber would be required and extra hadrons would also be generated by neutrino interactions inside the absorber. The principle used is that after many collision lengths only muons will remain close to their original trajectory. All other tracks will either be scattered through large angles or more probably undergo secondary interactions producing a large number of low momentum tracks which are unlikely to follow closely the direction of the original track.

The analysis of the bubble chamber data in combination with data from the EMI was performed using a HYDRA application program from the PAM files USBEMI and THIRA[16]. The general procedure is as follows:

a) The HYDRA geometry output for an event is scanned for all tracks, attached to primary vertices, which are identified as leaving the chamber volume.

b) Each track in turn is extrapolated in small steps through the BEBC structure, adding at each step the thickness of matter traversed and the contribution to the multiple scattering error over the step.

c) The extrapolation stops when one of the following conditions is met:

(i) The tracks stops in the magnet coils or the iron shielding,

(ii) the track exceeds a maximum number of turns (spirals),

(iii) the track re-enters the visible chamber volume,

(iv) the track misses the EMI,

(v) the track hits the EMI.

d) For each track which is predicted to hit the EMI the hit chamber is determined and the predicted hit position is expressed in the coordinate system of that chamber.

e) The EMI data for the event are read in and scanned for the chambers with predicted hits. Hit points are reconstructed from hits on overlapping anode wires and cathode strips.

f) The distances of the predicted hits from the reconstructed hits are computed and if one is found within a 2σ multiple scattering ellipse the track is considered to be a muon.

g) For the case of dimuon events there is the extra constraint that the hits for both candidate tracks must be coincident in time. How the time coincidence is measured is described in section IV.2.

IV.2 Layout and Operation of the EMI

The layout of the single plane version of the EMI as used in this experiment is shown in Fig. 4.1. It consists of a double row of 49 multi-wire proportional chambers, each of dimensions 3m x 1m, arranged in a semi-circle around BEBC at a distance of just over 7m from the centre of BEBC. Also shown is the additional iron shielding in the forward direction where the highest concentration of background hits occurs. As shown in Fig. 4.2 5 chambers in

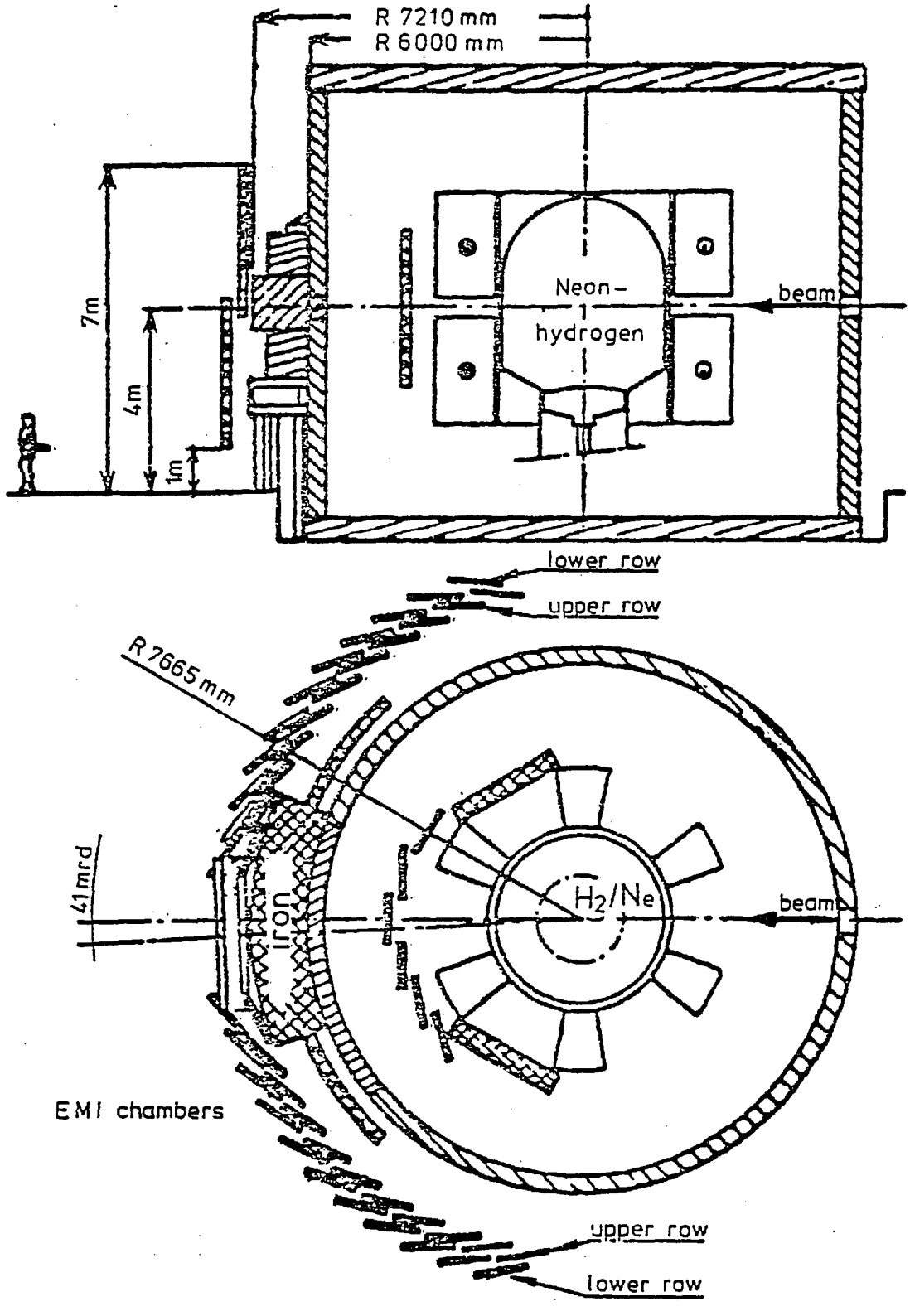
R 7210 mm
R 6000 mm
7m
4m
1m
Neon-
hydrogen
beam
lower row
upper row
R 7665 mm
41 mrd
iron
H_2/Ne
beam
EMI chambers
upper row
lower row

Fig. 4.1

a)

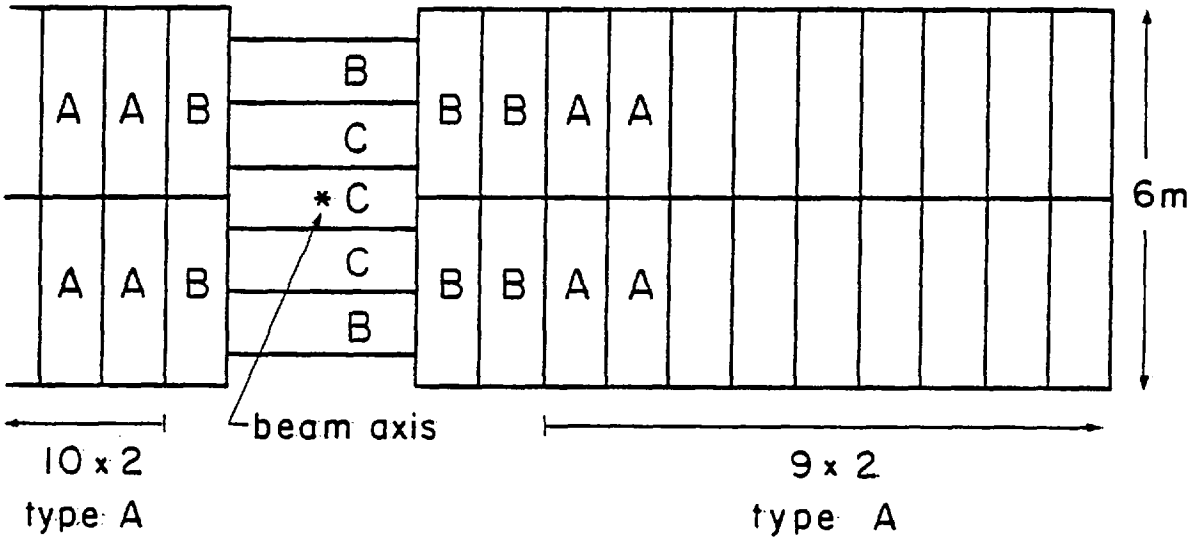

b)

chamber type	anodes one amplifier is connected to	cathode I one amplifier is connected to
A	8 wires	2 strips
B	4 -"-	1 -"-
C	2 -"-	1 -"-

Fig. 4.2

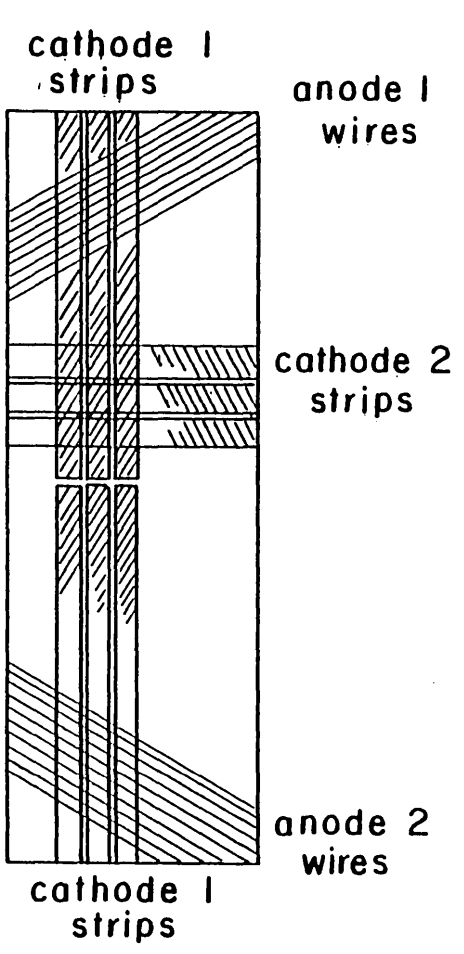
cathode 1
strips
anode 1
wires
cathode 2
strips
anode 2
wires
cathode 1
strips

a)

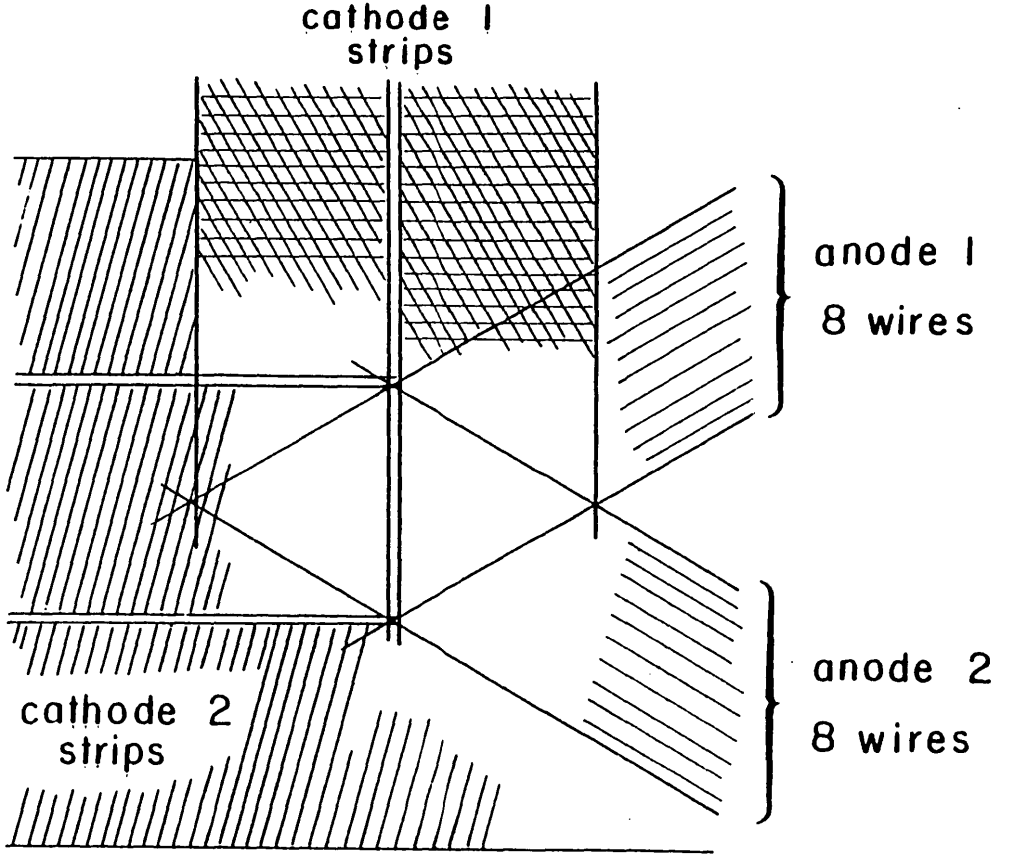
cathode 1
strips
anode 1
8 wires
cathode 2
strips
anode 2
8 wires

b)

Fig. 4.3

the central region are suspended with the 1m side vertical and the remaining 44 with the 3m side vertical. There is an overlap of a few cm of all adjacent chambers so that no dead zone occurs at the edges. An additional advantage of the overlap is that hits at the edge of any chamber may be correlated with hits in a nearby chamber. This information has been used to help determine accurately the positions of the chambers with respect to each other.

IV.2.1 General Structural Features of the Chambers

Fig. 4.2 also shows the location of the three different types of chamber adapted to meet the varying spatial resolution requirements of different parts of the detector. The physical construction of each chamber is the same; two anode wire planes oriented at $\pm 30^{o}$ to the 1m side and two orthogonal sets of cathode strips parallel to the sides. The strips parallel to the 3m side are split in the middle and read out independently to either end. The second cathode plane is not read out but reserved for possible future use. The orientation of the sense planes is shown in Fig. 4.3.

The variation in spatial resolution is achieved by coupling together different numbers of anode wires and cathode strips into a single electronic channel (Fig. 4.3b)).

IV.2.2 Principles of Readout Electronics

Data from the EMI are read out in digital form. The raw wire hits accumulated during the beam spill are stored in 40 bit shift register buffers and re-formatted and transferred to a magnetic tape during the time between spills. Each chamber possess a buffer containing one shift register for each electronic channel. The individual chamber buffers are connected to a 1k main buffer which records which chambers suffered hits at a given time during the beam spill, a hit being defined as a signal on each anode plane

of a chamber simultaneously. Fig. 4.4 shows the correlation between the main buffer and the chamber buffers for a hypothetical beam spill. Fig. 4.5 shows diagrammatically how the separate chambers are synchronised with one another and with the main buffer.

The important points to note about this system are the following:

(i) Events are stored without dead time losses irrespective of the hit rate on the chambers.

(ii) The whole system can record events occurring in 1023 different timeslots at arbitrary times during the beam spill.

(iii) The time resolution of the EMI (timeslot width) is determined by the speed of the shift registers (2MHz).

(iv) Each individual chamber can record up to 39 events during a beam spill with no restrictions on the number of wires hit.

The transfer of data to tape takes only a minute fraction of the inter-spill time (less than 100ms under heavy background conditions) leaving the on-line computer free to perform other tasks during most of this period.

IV.3 Data Acquisition Computer and On-line Software

As outlined in section IV.1 the EMI data is used off-line with the geometry reconstruction of the bubble chamber tracks. Hence, no direct monitoring of the EMI performance by sample data analysis is possible. For this reason test features were incorporated into the electronics to enable digital checking of the storage buffers and the whole readout chain as well as checking the EMI chambers with cosmic rays. In order to ensure efficient and reliable running of the EMI while operated by visiting groups it was considered

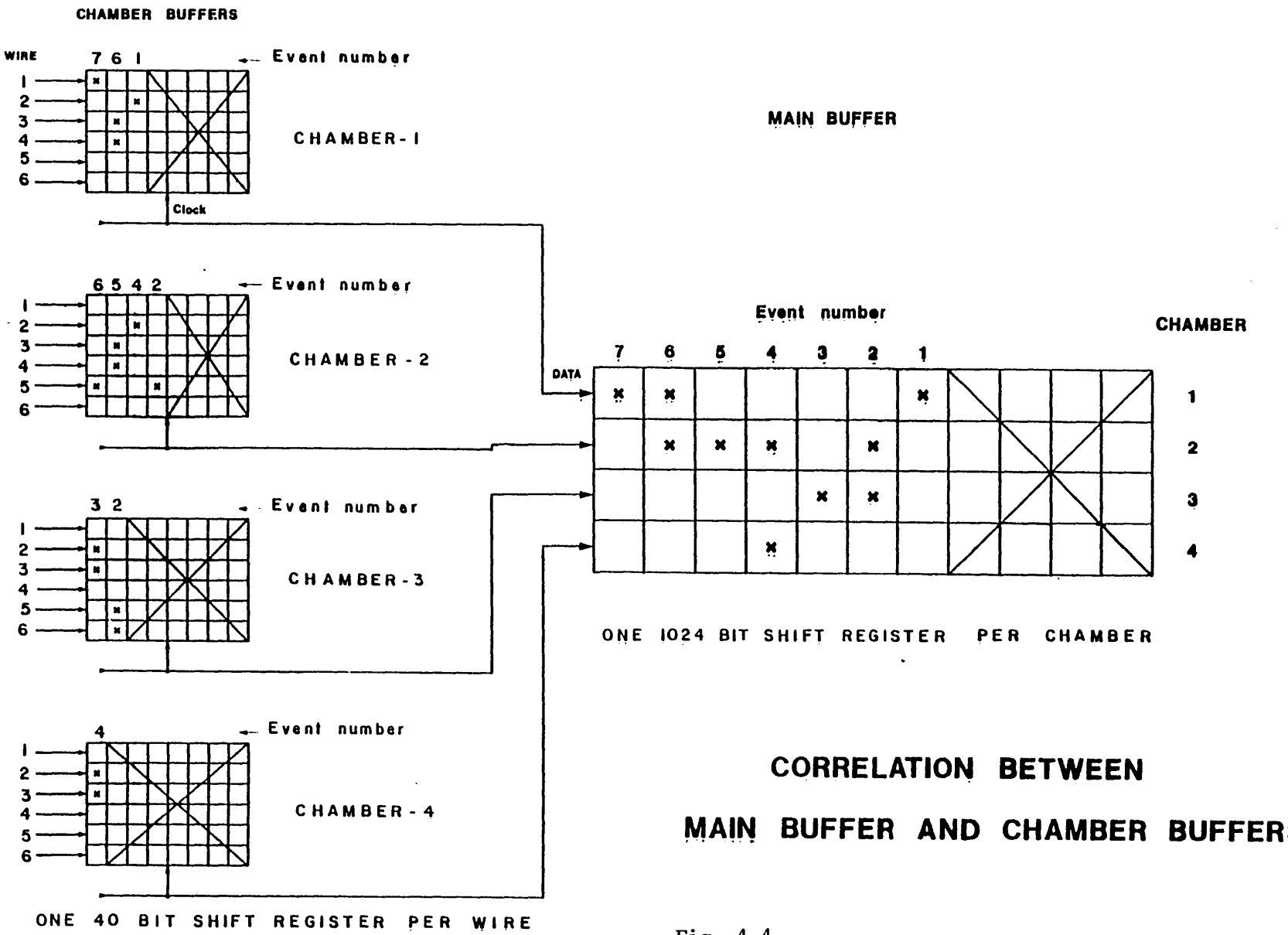

CORRELATION BETWEEN

MAIN BUFFER AND CHAMBER BUFFERS

Fig. 4.4

SYNCHRONISATION BETWEEN CHAMBER BUFFER AND MAIN BUFFER

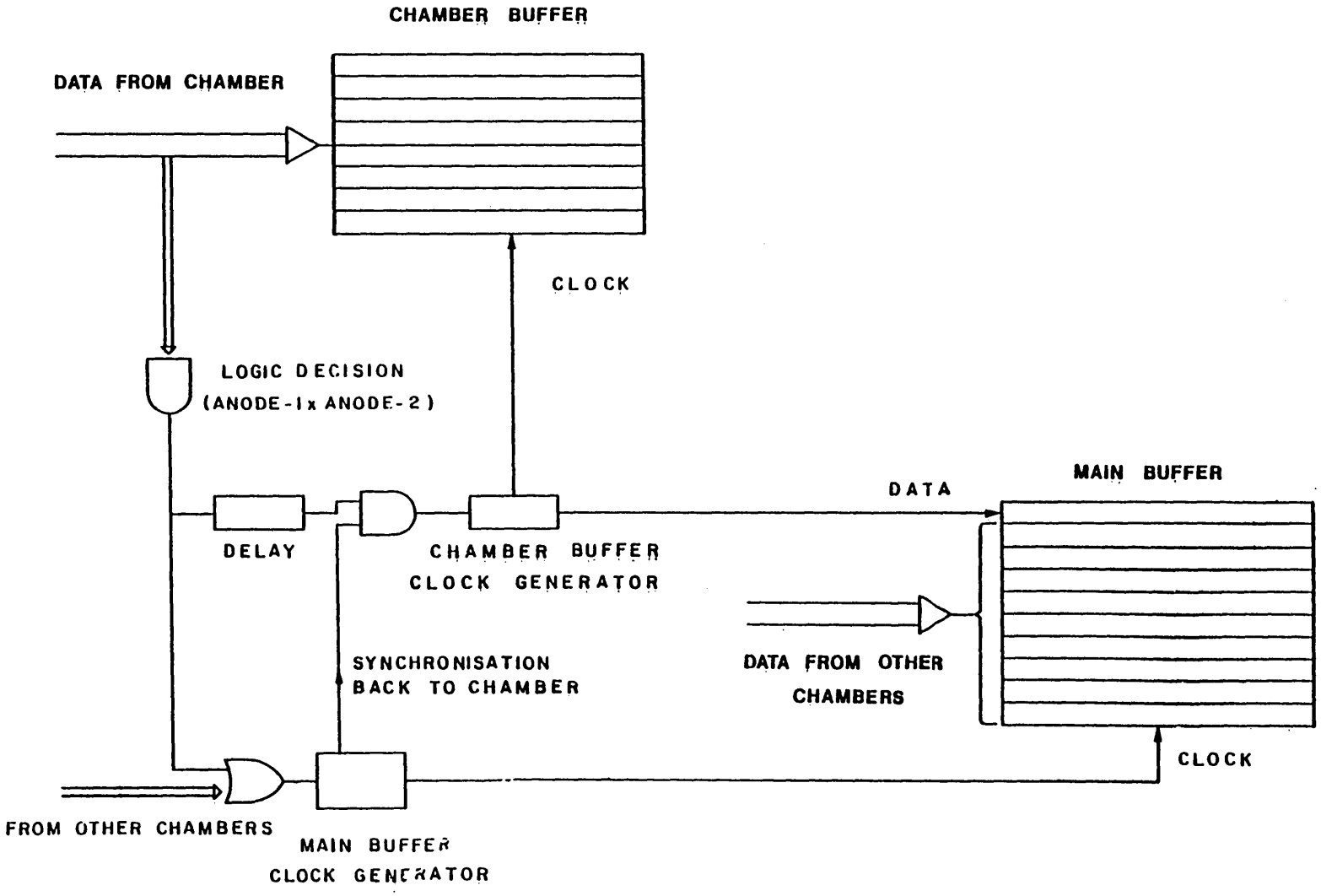

Fig. 4.5

necessary to monitor automatically as many parameters of the system as possible.

The computer chosen to fulfill these tasks was a NORD-10 possessing a flexible disc-based real-time operating system (SINTRAN III). The hardware interface is provided by CAMAC and direct memory access.

IV.3.1 Structure of the On-line Software

The on-line software splits naturally into a number of well defined functions e.g. EMI data input, histogramming, magtape output. These packages are implemented as separate real-time "tasks" scheduled by a set of control routines or by real-time interrupts generated by specific conditions in the hardware e.g. ν beam pre-pulse or readout triggered by chamber buffer overflow in cosmics test mode. The tasks communicate with each other by accessing a common data area in memory and the priority levels of each task ensure that data are not lost due to competition from lower level tasks at critical times. The relationships of the different tasks are shown in Fig. 4.6.

IV.3.2 Automatic Monitoring System

While at CERN during the winter of 1976-77 the author wrote and installed a software package for automatic monitoring of the EMI associated electronics and power supplies. The principal elements of the hardware for this system are shown in Fig. 4.7. The voltage test points are connected to the inputs of a group of 16 channel multi-plexors whose outputs are connected by a common analog bus to a digital voltmeter. A control module enables readings to be taken from a particular multi-plexor channel in response to coded instructions set up in an input-output register (BORER)

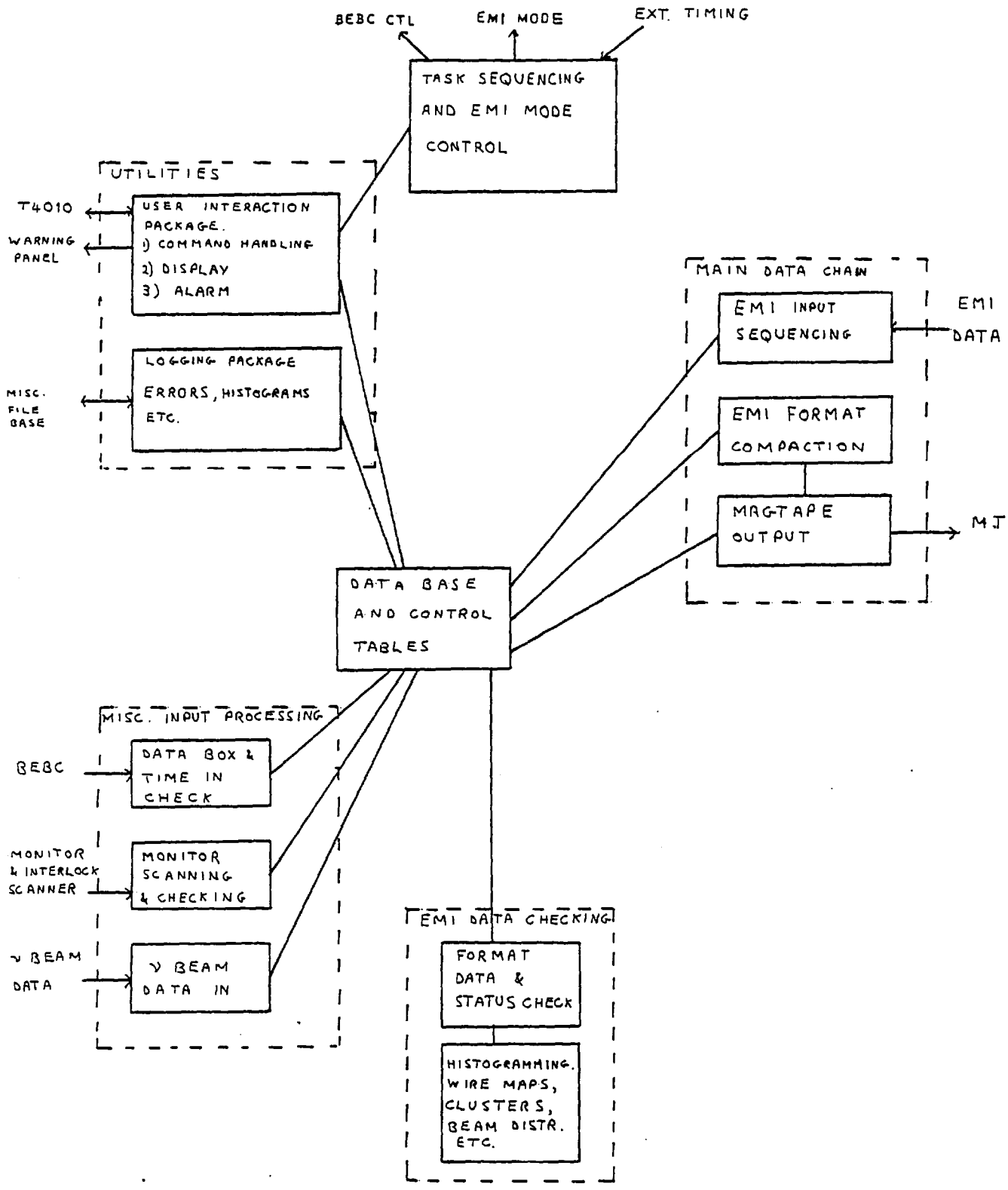

EMI ON-LINE PRODUCTION SOFTWARE

FIG. 4.6

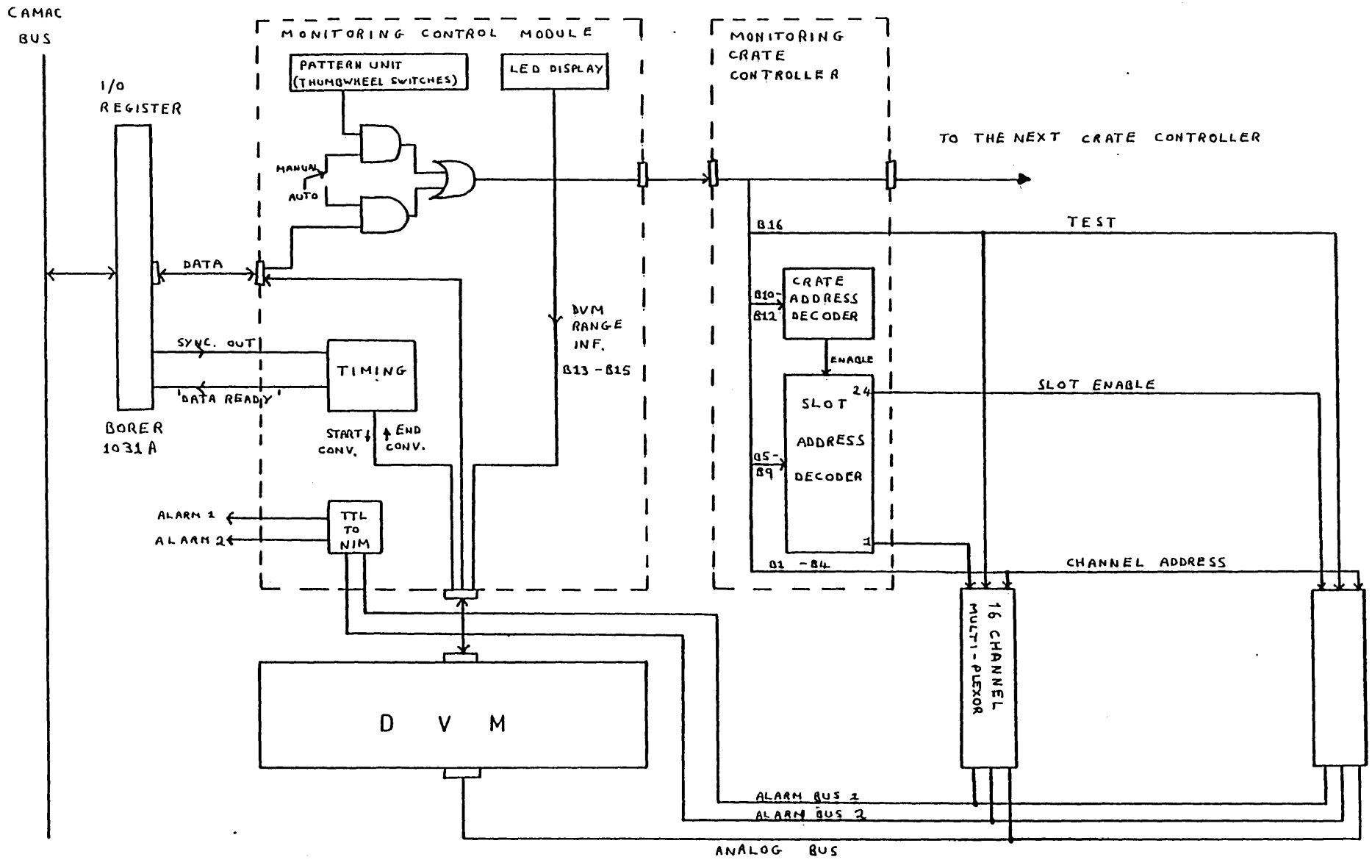

MAIN FEATURES OF EMI MONITORING HARDWARE

FIG. 4.7

OUTPUT CONTROL CODES

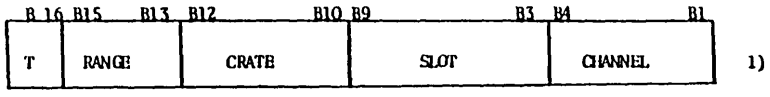

1)

T - TEST BIT. If "1" the addressed slot is disconnected from the analog bus.

RANGE - coded as follows:

0	-	1000 V
1	-	100 V
2	-	10 V
3	-	1 V
4	-	100 mV
5	-	10 mV

CRATE - Decoded from 0 to 7 (binary).

SLOT - Decoded from 0 to 24 (binary). Address 0 is for test purposes only.

CHANNEL - Decoded from 0 to 15 (binary).

The delay necessary to set up the scanner is introduced by the controller itself.

INPUT CONTROL CODES

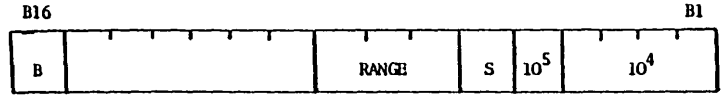

1)

2)

B - BUSY - at "1" when the DVM or scanner are busy

range - Range information feed back coded as follows:

1000 V	-	2
100 V	-	3
10 V	-	4
1 V	-	5
100 mV	-	6
10 mV	-	7

S - SIGN - at "1" when reading is positive

10^5 ... 10^0 - BCD information of the digitised analog value.

Fig. 4.8

FORMAT OF REFERENCE TABLE FOR EMI VOLTAGE MONITOR

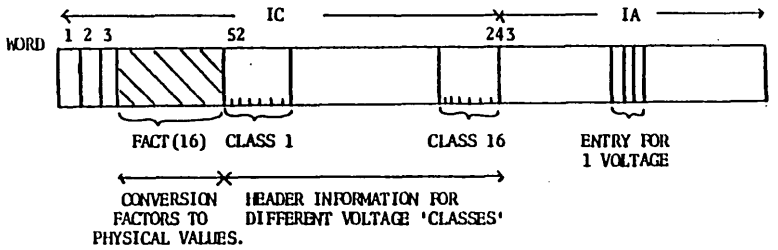

ARRAY IC

WORD

1 Number of header words per voltage class (12).

2 Number of classes (16).

3 Current number of points in monitoring table.

4 - 51 Floating point conversion factors between measured voltage and physical quantity monitored for each class. (N.B. one floating point word occupies three integer words in a NORD-10 computer).

52 - 243 Header information. 12 words for each class.

HEADER INFORMATION

WORD

1 Class number or zero if no entries exist or -1 if entries exist but monitoring is suppressed.

2 Defines positive or negative sign for upper and lower limits for class.

3 Defines DVM range to be used (currently 10 V or 100 V).

4 Power of 2 used to scale upper/lower limits stored as 10 bit integers.

5 Relative address in IA of first entry for this class.

6 Logging flag. (To indicate if long-term trends are to be recorded).

7 - 12 Text string (12 characters) to identify class on output.

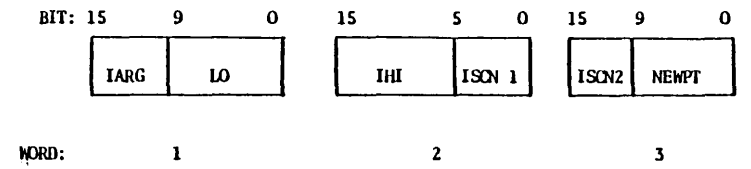

IARG = Sequence number of point in class (used internally and converted to EMI chamber number on output).

LO = Lower limit allowable for voltage.

IHI = Upper limit allowable for voltage.

ISCN 1 = 1st half of address of measurement point in CAMAC crate.

ISCN 2 = 2nd half of address.

NEWPT = Relative address in table of next point in sequence or 1023 if this is the last point.

INFORMATION STORED FOR AN INDIVIDUAL MONITORED POINT

Fig. 4.9

connected by CAMAC bus to the computer.

The monitoring program requests or receives a reading by means of Fortran-implemented calls which setup the output register and read the contents of the input register in the Borer unit. The control codes are shown in Fig. 4.8.

In addition to normal voltage readings the monitoring system handles three types of alarm state. They are: a temperature alarm on any of the storage buffer crates for the EMI, an overcurrent alarm on the HT supplies to these crates and a general interlock alarm. The temperature and overcurrent alarm levels for each individual crate are also supplied to two of the channels in the 16 channel multi-plexors so that the monitoring program may identify the individual crate generating the alarm condition. Also any of the three alarm conditions will generate a real-time interrupt to activate the monitoring program to identify the source of the trouble and will interrupt a routine voltage scan to give priority to the alarm. Under normal conditions the monitoring program checks voltages at the rate of one every second against a table of allowed ranges maintained on a disc file. Users may modify the limits set for individual voltages, remove points from the set to be examined or create new ones as may be necessary.

To maintain flexibility in changing the number of voltages to be measured, with a view to future extension, and in order to minimise the amount of core needed to store the reference table, a system of linking information by pointers was used. By thus enabling the information for any point to be stored anywhere within the table no blocks of zeros need to be carried around to represent unmeasured points. The format of the reference table is given in Fig. 4.9. In general, the same channel in different multi-plexors

is used to connect to voltages of the same type, e.g. channel 2 is used for a +5V pre-amplifier power supply. This is not a requirement of the system, since the full address is kept for each point in the table, but is merely a convenient arrangement.

The monitoring software is split into two parts. The first part is a set of three subroutines which are used directly by the main control tasks. Subroutine MINIT is called on startup of the EMI software chain and initialises automatic scanning of the monitoring system. The other two subroutines are a sub-set of the general command processing task and deal with operator instructions concerned with the monitoring program. The second part of the monitoring software is an independent real-time task, YMONTR, which performs the voltage measurements, checks the values against allowed ranges, performs any error output necessary, deals with alarms and performs any updates required in the reference table.

YMONTR normally has a priority level one less than the operator communication task but higher than other inter-spill tasks, such as efficiency checking with cosmic rays. The highest priority task is of course the beam-spill readout task. Thus the monitoring task connot block either the main data readout or the input of instructions. It would, however, block the other inter-spill tests and is therefore designed to stop after each measurement it makes in scan mode. When a measurement is complete YMONTR executes a scheduling call to restart itself after an interval of one second and the program then ends. By this means the lower priority tasks are enabled to run. The exception to the deliberate one second wait occurs on receipt of an alarm. YMONTR then runs continuously until a complete scan of all possible alarm sources has been made. The rate of continuous readings is 5 to 10 readings per second. When checking

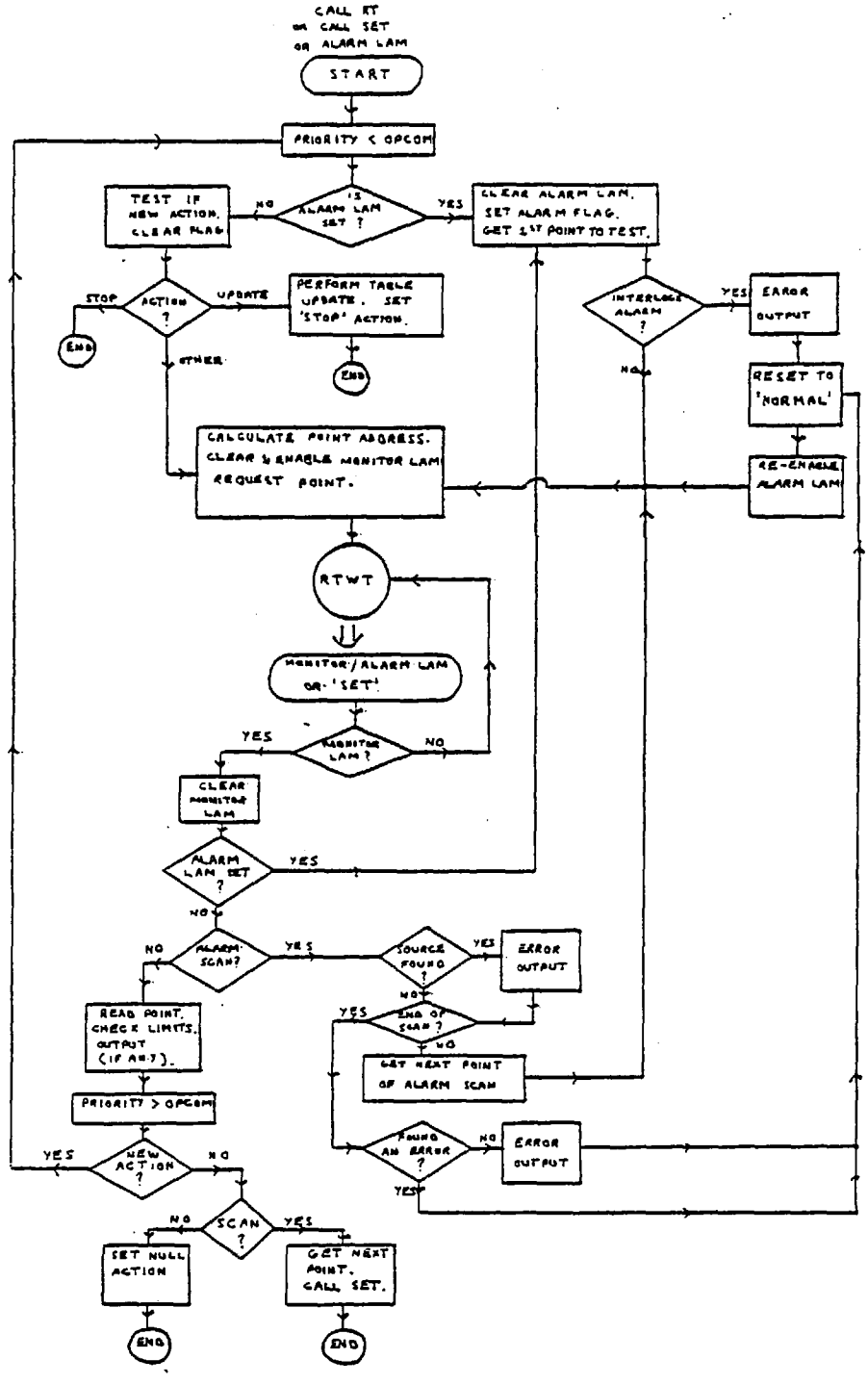
CALL RT
OR CALL SET
OR ALARM LAM
START
PRIORITY < OPCOM
TEST IF NEW ACTION. CLEAR FLAG
IS ALARM LAM SET ?
NO
YES
CLEAR ALARM LAM. SET ALARM FLAG. GET 1ST POINT TO TEST.
ACTION ?
STOP
UPDATE
OTHER
END
PERFORM TABLE UPDATE. SET 'STOP' ACTION.
END
INTERLOCK ALARM ?
YES
NO
ERROR OUTPUT
RESET TO 'NORMAL'
RE-ENABLE ALARM LAM
CALCULATE POINT ADDRESS. CLEAR & ENABLE MONITOR LAM REQUEST POINT.
RTWT
MONITOR/ALARM LAM OR 'SET'
MONITOR LAM ?
YES
NO
CLEAR MONITOR LAM
ALARM LAM SET ?
YES
NO
ALARM SCAN?
NO
YES
SOURCE FOUND ?
YES
ERROR OUTPUT
NO
END OF SCAN ?
YES
NO
READ POINT, CHECK LIMITS, OUTPUT (IF ANY).
GET NEXT POINT OF ALARM SCAN
PRIORITY > OPCOM
FOUND AN ERROR ?
NO
ERROR OUTPUT
YES
NEW ACTION ?
YES
NO
SCAN ?
NO
YES
SET NULL ACTION
END
GET NEXT POINT. CALL SET.
END

FIG. 4.10

the software flags which inform YMONTR of a new instruction priority is first raised above that of the operator communication task to prevent it from changing the flags during this time. Checking is also performed in the operator communication subroutines to ensure that issuing a new instruction does not interfere with one already being executed. Fig. 4.10 shows the main logical sequences of YMONTR.

IV.4 Performance of the EMI

The physics topics most dependent on good EMI performance are of course the studies of dimuon events and neutral current cross-section determinations[17,18] where a clean separation of CC and NC events is essential. For both these topics a careful study has been made of the EMI background levels and efficiency for identifying genuine muons.

IV.4.1 Background Rates

Most background calculations which have been performed for the EMI have been done for wide-band beam conditions in which many particles hit the EMI per beam spill and the problem of false association of tracks to background hits is rather severe. The problem of hadrons generated in the external structure of BEBC and its additional iron shielding has in fact necessitated the installation in May 1977 of a second plane of wire chambers close to the chamber body. By demanding that a candidate muon should register hits close to its extrapolated track in both planes and also within the same timeslot this difficulty can be overcome.

As stated previously only a single plane EMI was available at the time of running the WA19/22 experiment. However, in the narrow-band beam operation the background rate on the EMI is negligible.

Typically only 5 to 10 hits will be registered on the whole of the EMI ($150m^2$) per beam spill. The probability of falsely identifying a track as a muon by association with a random hit has been determined as $\sim$3% per leaving hadron with momentum greater than 5 GeV/c by attempting to match leaving tracks from events on one frame with the EMI data from the following beam pulse.

Hadron punch-through to the EMI is completely negligible ($\sim e^{-10}$) due to the thickness of iron absorber present, 1200 - 2100 gm cm^{-2}, but there exist the possibilities of $\pi \to \mu$ or $k \to \mu$ decay in flight, the muon subsequently reaching the EMI or hadron cascades in the absorber with one of the secondary particles produced hitting the EMI close to the predicted hit position of one of the tracks leaving the bubble chamber. These effects have been estimated by a monte-carlo program[19] to assess the background of false muons in the dimuon sample. The results are shown in Fig. 4.11a) for ν and Fig. 4.11b) for $\bar{\nu}$. The numbers are consistent within errors with the number of "wrong-sign" events observed in the CC sample. Of course for dimuon events the probability of association of the second muon with a spurious hit not caused by the event is even smaller than for the CC sample due to the added constraint that the hits for both muons must occur simultaneously.

IV.4.2 Identification Efficiency

The overall efficiency for identifying a muon in the EMI is determined by the geometrical acceptance of the detector and the electronic efficiency of the wire planes themselves. Due to the trapping of low momentum particles by the magnetic field of BEBC some muons will never reach the EMI and the geometric acceptance of the detector falls rapidly for momenta less than 5 GeV/c. Above this momentum acceptance is essentially 100% so a cut was imposed at 5 GeV/c and no EMI associations of slower tracks were

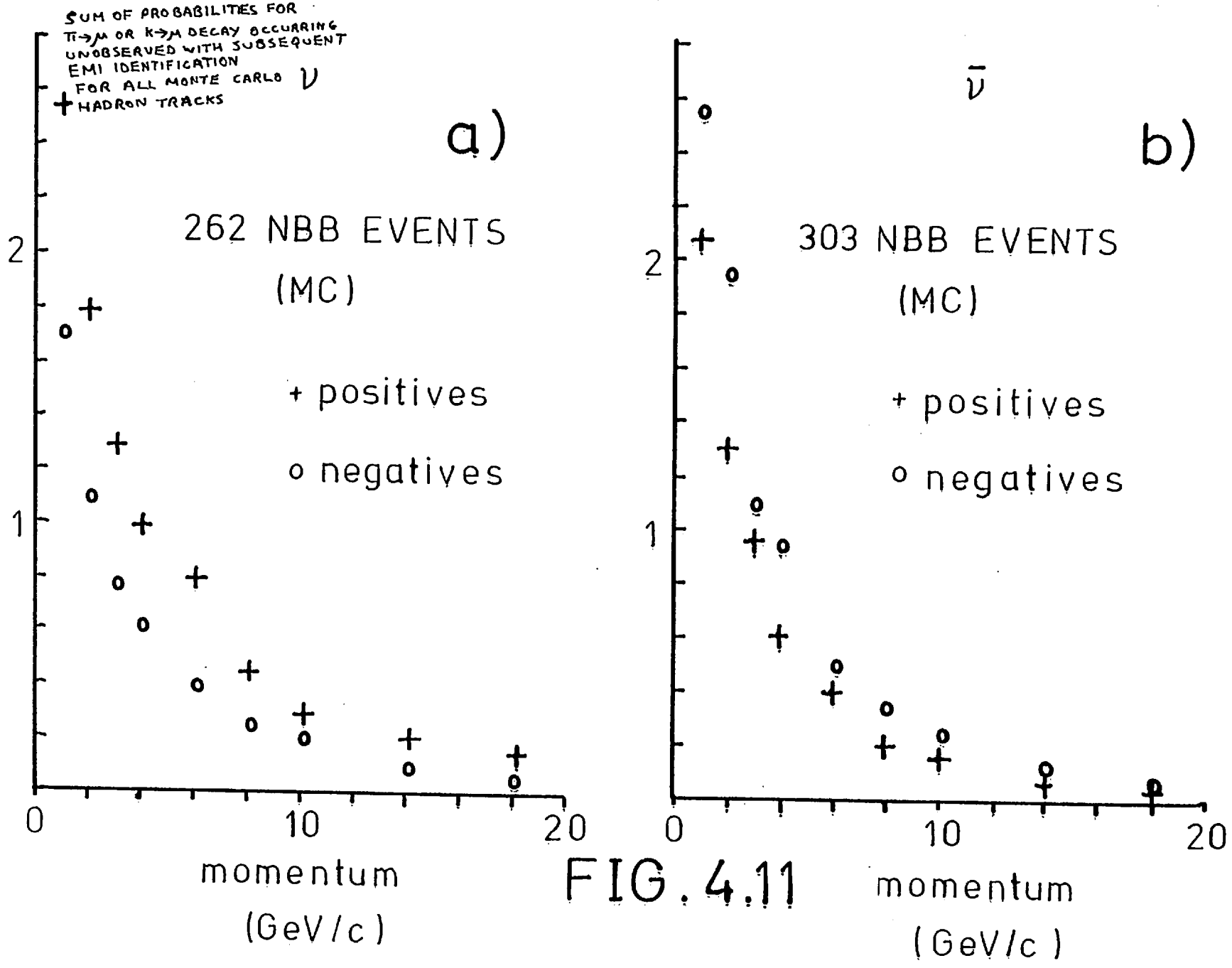
SUM OF PROBABILITIES FOR
π→μ OR K→μ DECAY OCCURRING
UNOBSERVED WITH SUBSEQUENT
EMI IDENTIFICATION
FOR ALL MONTE CARLO ν
+ HADRON TRACKS
a)
262 NBB EVENTS
(MC)
+ positives
o negatives
2
1
0
10
20
momentum
(GeV/c)
ν̄
b)
303 NBB EVENTS
(MC)
+ positives
o negatives
2
1
0
10
20
momentum
(GeV/c)

FIG. 4.11

accepted with the exception of additional candidate muons in the dimuon events. Here a cut of 4 GeV/c was imposed for any additional muons. This cut still maintains 95% geometrical acceptance and the time coincidence requirement reduces the uncertainty of association of slow additional muons. For the determinations of CC and NC cross-sections and the evaluation of the nucleon structure functions[3,18,4] corrections were made for CC events assigned as NC as a result of the above cut by assuming a flat y distribution for neutrinos and a $(1-y)^2$ distribution for antineutrinos.

The electronic efficiency of the EMI is mainly determined by the small percentage of dead channels in the wire chambers[20]. This factor has been determined in two independent ways. The first method consisted of measuring a sample of about 2000 beam associated muons and simply counting the number of tracks which associated to EMI hits and the number which did not. A lower momentum cut on these tracks of 40 GeV/c was used, with additional cuts on dip and azimuth, to ensure that the tracks really were muons associated with the beam spill and not tracks due to cosmic rays. This method suffers from two major disadvantages. First, the rather severe cuts on momentum and angles meant that the tracks passed through the most central EMI chambers lying along the beam axis. Thus the efficiencies of these chambers were well determined but the efficiencies of the outermost chambers were very badly known and reliance had to be placed on the comparison of hit rates from cosmic ray sources accumulated between the beam spills. Secondly, all the data on through going muons came from the earliest part of the runs so there was no information on any possible degradation of performance with time. Again, the on-line checking with cosmic rays was the only means of testing this.

The second method overcomes both of these difficulties since it employs the event sample used in the analysis thereby contriving to cover the full period of data taking and the full range of solid angle utilised. The method consists of comparing the transverse momentum distribution (p_T) of the leaving tracks in the candidate NC events for positive and negative particles separately. An excess of particles at high p_T in the right-sign sample (-ve in ν_μ +ve in $\bar{\nu}$) was interpreted as being due to unrecognised muons in CC events. The results of this method agree with those of the first method and the overall identification efficiency above 5 GeV/c muon momentum is determined to be 97.5%.

IV.5 Muon Momentum Improvement Using EMI Information

The fiducial volume in BEBC was chosen such that the potential length of any track going forward from a neutrino interaction would be at least 50cm. This choice is necessarily a compromise between retaining as many events as possible for physics analysis and allowing sufficient track length to be able to perform accurate geometrical reconstruction of the accepted events. As a result of this decision high energy events occurring near the end of the fiducial volume are subject to large momentum uncertainties. In the case of charged current events most of the uncertainty usually comes from the muon.

For EMI identified muons the associated hit position provides a constraint which can be used to improve upon the value and error of the momentum obtained by measurement of the bubble chamber film. This is possible due to the large distance (~7.6m) of the EMI outer plane from BEBC, which provides a much greater "lever arm" than the available length inside the bubble chamber.

In addition the low rate of background hits in the 200 GeV/c narrowband beam (~5-10 hits/150m^2) ensures that this technique is reliable due to the small probability of associating a track with a wrong EMI hit.

IV.5.1 Method of Momentum Correction

The momentum correction formulae outlined here correspond to a simplified solution for a single plane EMI where the magnetic field is assumed to be entirely parallel to the z axis (vertical) and angle errors of tracks are assumed to be negligible compared with the momentum error[21]. The formulae are the result of the minimisation of a chi-squared function involving the displacement of the EMI reconstructed hit from the extrapolated track, a magnetic field integral along the tracks path, the momentum error of the track determined by geometry, the positional error due to multiple scattering of the track and the error in the reconstructed hit position on the EMI.

Extrapolation of tracks is done in terms of transverse track parameters and the final result of the momentum correction formulae is expressed using these parameters. The transverse track parameters express the position and direction of a track at any point along its length with respect to the position and direction of a reference trajectory corresponding to the path followed in a magnetic field ignoring multiple scattering. In two dimensions the parameters are the distance, t, from the reference trajectory and the angle, α, between the track and the reference trajectory. In three dimensions there are two orthogonal sets of transverse track parameters. The "horizontal" parameters are parallel to the (x,y) plane and the "vertical" parameters are perpendicular to both the track

direction and the horizontal parameters. The advantage of this system is that the error matrix for the track parameters has no correlations between the horizontal and vertical components so only the horizontal components appear in the correction formulae, given the assumption of magnetic field parallel to the z axis. The final formulae obtained are[21]

$$\delta\tfrac{1}{p} = \frac{-I\,\mathrm{Cos}\lambda\; t_\alpha\; (\Delta\tfrac{1}{p})^2}{(\Delta t_{ms})^2 + (\Delta v_\alpha)^2 + I^2\mathrm{Cos}^2\lambda(\Delta\tfrac{1}{p})^2} \qquad (4.1)$$

for the correction to add to $\tfrac{1}{p}$ and

$$\frac{1}{\Delta(1/p)^2_{fit}} = \frac{1}{\Delta(1/p)^2} + \frac{I^2\mathrm{Cos}^2\lambda}{(\Delta t_{ms})^2 + (\Delta v_\alpha)^2} \qquad (4.2)$$

for the error on the new value of 1/p. In the above equations λ is the dip of the track, t_α is the horizontal displacement between the reconstructed hit on the EMI and the predicted hit of the track, Δv_α is the error on the horizontal position of the reconstructed hit and Δt_{ms} corresponds to the width of the multiple scattering circle at the position of the EMI. I is a field integral term given by

$$I = LI_o - I_1$$

where $I_o = \int_0^L H(l)dl$, $I_1 = \int_0^L lH(l)dl$,

L is the total track length followed in the extrapolation and H(l) is the magnetic field at a distance l along the track.

IV.5.2 Tests of the Reliability of Momentum Improvement

To establish absence of systematic biases in the momentum improvement technique the author made a series of tests using a sample of about 2000 beam-associated tracks which traversed the entire length of the BEBC chamber. A sub-sample of these tracks having momenta above 40 GeV/c were originally used for surveying the chambers of the outer plane of the EMI which lie close to the beam direction. This enabled the external measurements of the position of the EMI chambers to be related to the optical coordinate system of the BEBC chamber[22].

The reason for using this sample of tracks to check the accuracy of the momentum improvement technique was the same as that for the EMI survey, namely the fact that the geometrical parameters of these tracks (especially the momenta) were known to high accuracy due to the length of the tracks which could be measured (3.5m).

IV.5.3 Procedure

As outlined above the tracks most in need of momentum improvement are likely to be those from events near the downstream end of the fiducial volume. Therefore in order to test the technique errors were increased and momenta shifted to simulate the results of measuring only 50 cm of track length. The way to do this was determined by plotting a distribution of $\Delta p/p^2$ ($\equiv\Delta(1/p)$) against track length for tracks, taken from the event sample, which left BEBC without interacting or decaying. Since $\Delta 1/p$ for a track is related to the measurable sagitta, which is in turn related to the square of the measured length of the track, this distribution takes the form of a characteristic curve (Fig. 4.12). Thus, for

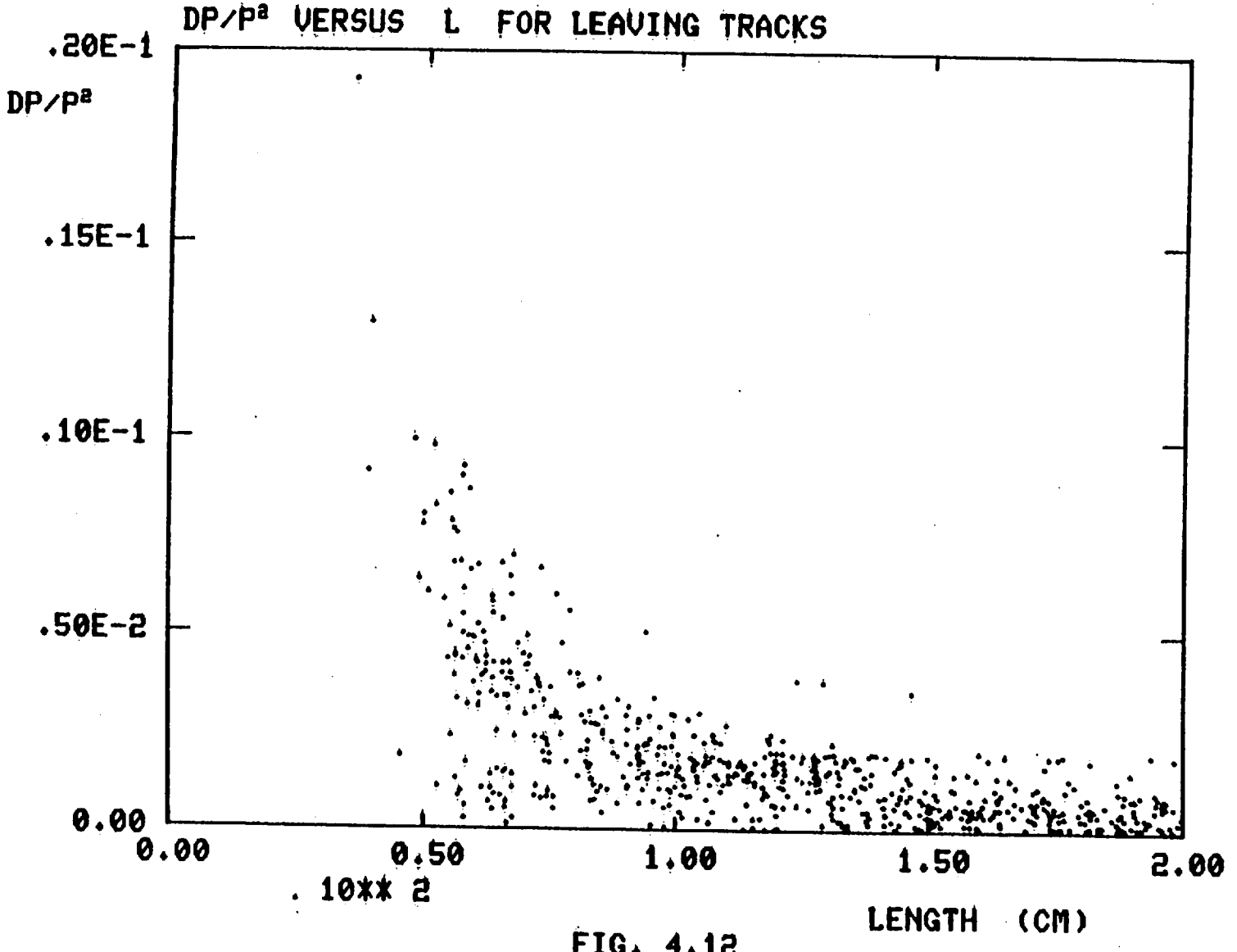
DP/P² VERSUS L FOR LEAVING TRACKS
.20E-1
DP/P²
.15E-1
.10E-1
.50E-2
0.00
0.00
0.50
1.00
1.50
2.00
. 10** 2
LENGTH (CM)

FIG. 4.12

any given length of track a 'typical' momentum error can be read off. For a track of 50 cm this value is $\Delta 1/p = 0.007$.

The procedure followed to test the momentum improvement formulae was then as follows. For each individual track,

(i) the measurement error $\Delta 1/p$ was set equal to 0.007,

(ii) the value of $1/p$ was shifted by the new $\Delta 1/p$ in one direction,

(iii) the track was extrapolated to the EMI using the new parameters.

(iv) If a good association to an EMI hit was found the correction was applied.

(v) The corrected values of $1/p$ and $\Delta 1/p$ were compared to the initial well determined measurement.

This procedure was applied separately for shifts of $+\Delta 1/p$ and $-\Delta 1/p$ to isolate any systematic shifting of the momenta introduced by the correction. Figs. 4.13-4.14 show the results of these tests. It is evident that the correction to the shifted momenta brings the values of $1/p$ back towards their initial well measured values although the distribution of tracks after correction is not precisely centered on the 'true values'. This is because the 'improved momentum' value is essentially a weighted combination of the 'badly measured' value and the EMI constraint. However, it can be seen that the improved momenta are less biased than the 'badly measured' momenta.

The cutoff at 40 GeV/c is mainly due to the need to reduce the computing time required. The distribution of momenta of the through-going track sample peaks well below 40 GeV/c and among the low momentum tracks less than 1 in 5 produce an acceptable association to an EMI hit. Many of these low momentum tracks will

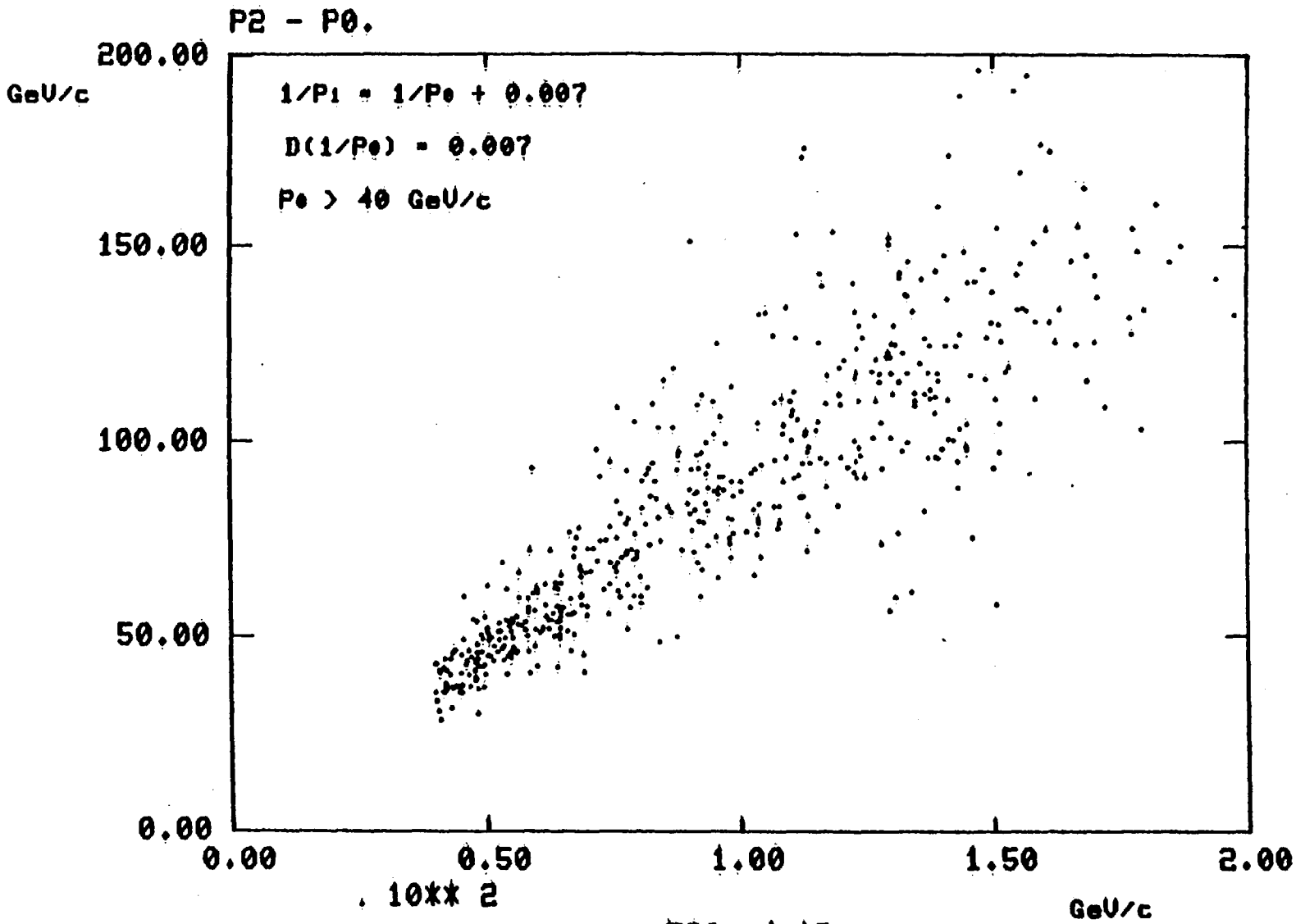
P2 - P0.
200.00
GeV/c
1/P1 = 1/Pe + 0.007
D(1/Pe) = 0.007
Pe > 40 GeV/c
150.00
100.00
50.00
0.00
0.00
0.50
1.00
1.50
2.00
10** 2
GeV/c

FIG. 4.13

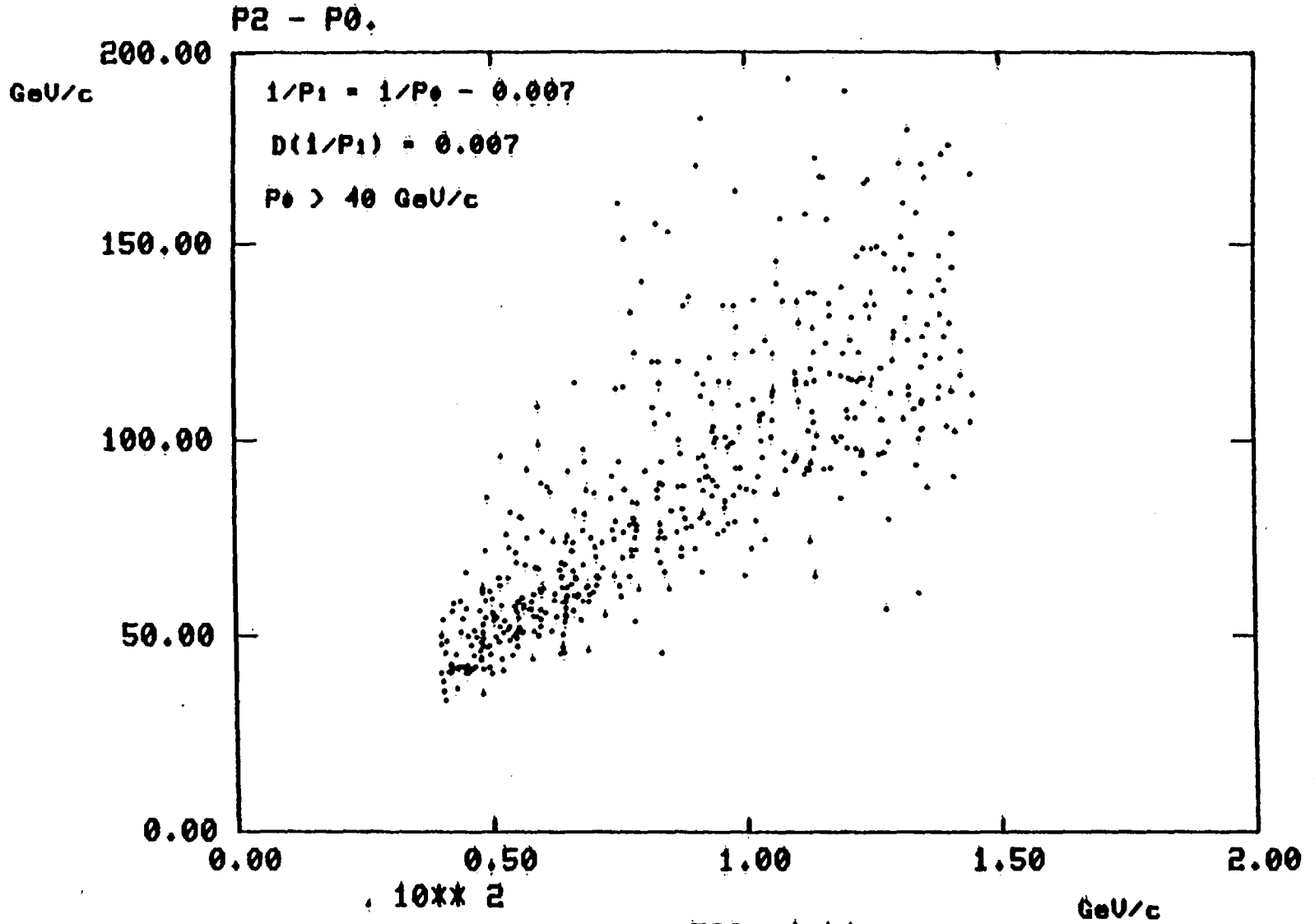
P2 - P0.
200.00
GeV/c
1/P1 = 1/P0 - 0.007
D(1/P1) = 0.007
P0 > 40 GeV/c
150.00
100.00
50.00
0.00
0.00
0.50
1.00
1.50
2.00
10** 2
GeV/c

FIG. 4.14

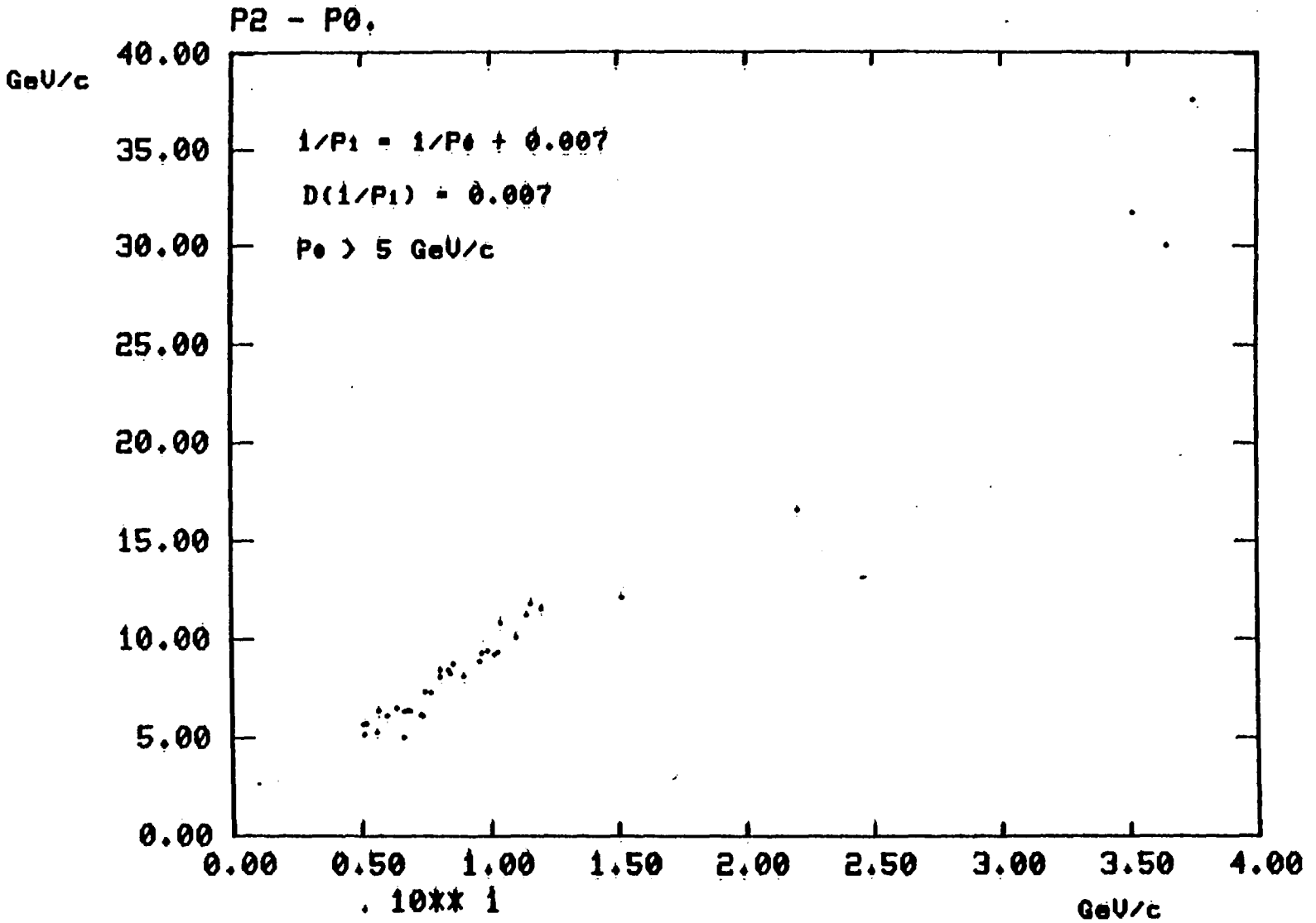
P2 - P0.
GeV/c
40.00
35.00
30.00
25.00
20.00
15.00
10.00
5.00
0.00
1/P1 = 1/P0 + 0.007
D(1/P1) = 0.007
P0 > 5 GeV/c
0.00
0.50
1.00
1.50
2.00
2.50
3.00
3.50
4.00
. 10** 1
GeV/c

FIG. 4.15

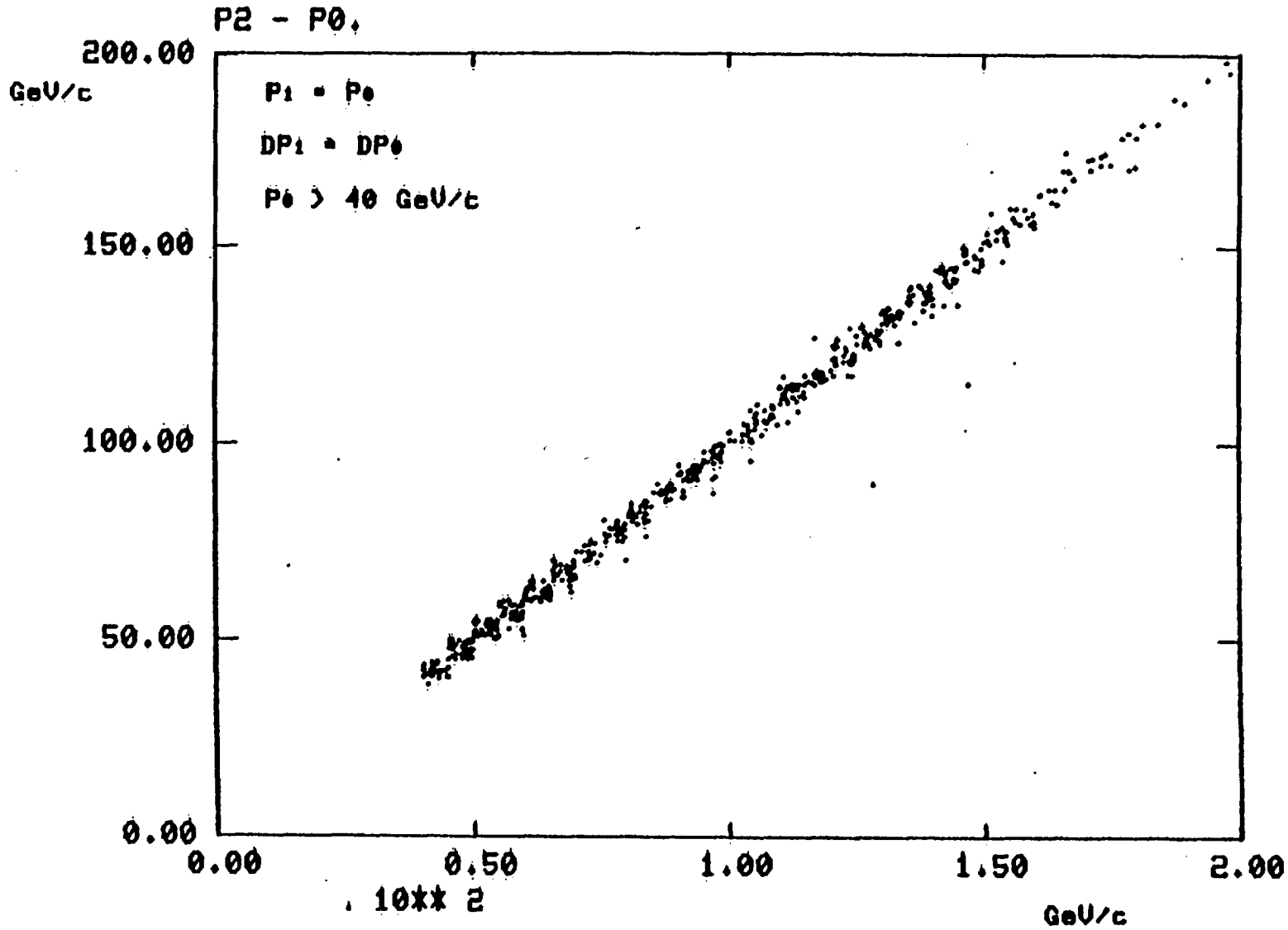
P2 - P0.
200.00
GeV/c
P1 = P0
DP1 = DP0
P0 > 40 GeV/c
150.00
100.00
50.00
0.00
0.00
0.50
1.00
1.50
2.00
. 10** 2
GeV/c

FIG. 4.16

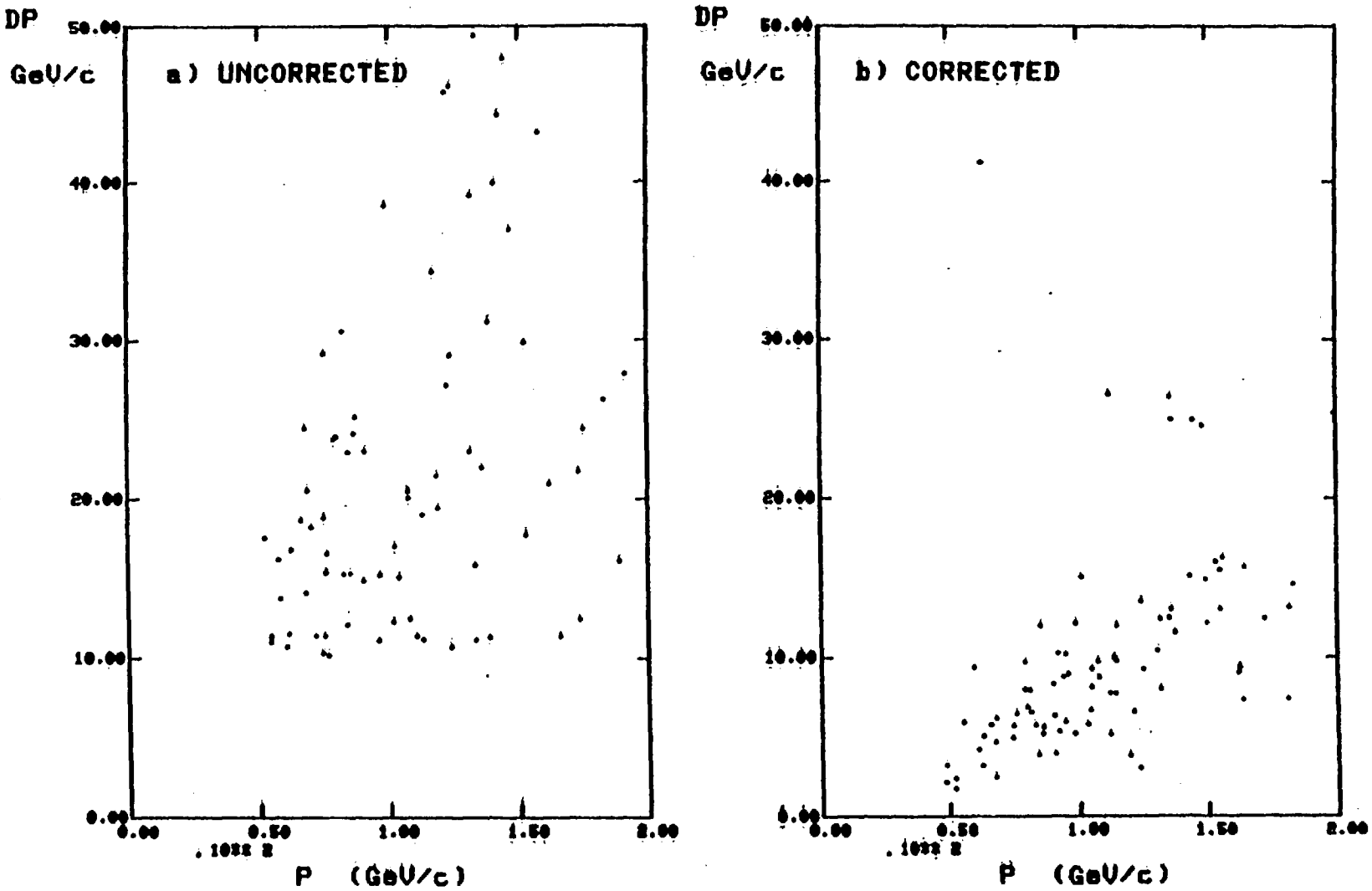
DP
GeV/c
a) UNCORRECTED
50.00
40.00
30.00
20.00
10.00
0.00
0.00
0.50
1.00
1.50
2.00
P (GeV/c)
DP
GeV/c
b) CORRECTED
50.00
40.00
30.00
20.00
10.00
0.00
0.00
0.50
1.00
1.50
2.00
P (GeV/c)

FIG. 4.17

not be muons, but hadrons produced in neutrino interactions in the structure of BEBC or the shielding immediately upstream. Therefore the inclusion of all tracks down to 5 GeV/c momentum would require many hours of computer time to achieve the same statistics at the high momentum end of the spectrum. However, a separate test was done on a limited sample of tracks down to 5 GeV/c and no difference was observed from the results obtained at higher momenta.

Figs. 4.13 and 4.14 show the results of the correction on tracks above 40 GeV/c for an increased error, $\Delta 1/p = 0.007$, combined with a one standard deviation shift in 1/p upwards and downwards respectively. In the latter case, corresponding to an increase in momentum, there is a cutoff at about 140 GeV/c at which point the shifted momentum, p_1, becomes 'unmeasured' since 1/p is zero. Fig. 4.15 shows results for the sample down to a 5 GeV/c cutoff and Fig. 4.16 shows the effect of the correction applied to the initial well measured values of the tracks above 40 GeV/c. In this case the dominant factor is the small error on the initial momenta which makes the correction (equation 4.1) small.

IV.5.4 Implementation of Momentum Improvement in the CC Data Sample

Having determined the unbiased nature of the technique and given the fact that when it was applied to muons with large momentum errors the errors were greatly reduced it was decided to apply the correction to all muon tracks whose momentum error was greater than 10 GeV/c.

This was done at the GST stage by providing an extra track card for the muons concerned. The original track cards were given

an exclusion flag and the new cards, identified by a fit code 'EM', were given a 'best hypothesis' flag and otherwise differed only in the values of momentum and error. By this means the original geometry-only momentum could be regained if required. Fig. 4.17 demonstrates the improvement made to muons in the CC data sample. Fig. 4.17a) shows the momentum error, Δp, of the muons plotted against their momentum for the original geometry-only values and Fig. 4.17b) is the corresponding plot for the combined geometry and EMI values. It can be seen that for most tracks the momentum uncertainty is dramatically improved. The number of CC events corrected in this way corresponds to about 7% of the total statistics.

CHAPTER V DI-LEPTON EVENTS

V.1 Introduction

Neutrino interactions with more than one lepton in the final state were first observed in counter experiments at FNAL[14] where events having two oppositely charged muons were found. Later the production of positrons together with negative muons in neutrino interactions was observed in the Gargamelle bubble chamber in CERN[23] and in the 15' bubble chamber at FNAL[24]. Since then the CDHS collaboration at CERN has analysed a large sample of multi-muon events including opposite sign[25] and same-sign[26] dimuons as well as trimuons.[27]

In the case of dimuon and muon-electron events the bubble chamber experiments have all observed a strong correlation with the production of strange particles in the final state which is in accord with the idea that these events are due to the production and semi-leptonic decay of charmed hadrons in normal charged current interactions.[28] This chapter describes the results of a search for multi-muon and muon-electron events in BEBC and interprets these events as having a charm origin.

V.2 Raw Event Numbers and Background Sources

Scanning for events possessing an electron of either sign from the primary vertex has been described previously in Section III.2 and will not be repeated here except to recall that the correction factor for scanning and identification

losses is 1.5 ± 0.3. Five μ^-e^+ events were found in the neutrino sample and one μ^+e^- event in the antineutrino sample. Background sources of $e^\pm$ in events already possessing an identified muon are asymmetric Daltiz pairs and gamma conversions very close to the vertex, K_{e3} decays in flight without a visible kink and $\pi_{\mu e}$ decays at rest. Also μ^+e^- events have a background from δ-rays and Compton electrons. A minimum momentum cut of 0.3 GeV/c was imposed on electron candidate tracks in order to reduce the background from asymmetric Dalitz pairs, gamma rays and Compton electrons. Dalitz pairs and close gamma conversions having less than 5 MeV/c in one track and greater than 0.3 GeV/c in the other are estimated to contribute 0.3 events and 0.1 events for neutrinos and antineutrinos respectively. (A track of 5 MeV/c or lower momentum at the vertex would be very difficult to detect). This source of background is only significant for candidate tracks below 1 GeV/c. The background from K_{e3} decays has been estimated to be $\sim 2 \times 10^{-5}$ per CC event.

All events having an EMI identified muon were examined for other candidate muon tracks which left the bubble chamber without kinking or interacting. Care was taken to ensure that all such tracks were adequately measured and reconstructed by geometry. The fastest muon of the right sign (negative in neutrinos, positive in antineutrinos) was taken to be the "leading" muon. Any other EMI identified muons were required to be associated to a reconstructed hit on the EMI occurring within the same timeslot (of width 500 ns) as the

hit associated to the leading muon. The same χ^2 restriction is placed on all muons. In the case of two or more tracks being associated to the same hit on the EMI the track with the smallest χ^2 for association is accepted and the other track is rejected. In practice no cases of ambiguity in defining the "best" muon were found. In all cases of multiple association of hits or association of tracks to hits in different timeslots only one candidate survived the χ^2 cut. The momentum of the leading muon was required to be greater than 5 GeV/c corresponding to 100% geometrical acceptance by the EMI. For additional muons a momentum cut of 4 GeV/c was imposed. With this cut 95% geometrical acceptance is still maintained. The lower momentum cut for additional muons is possible, in spite of the increased uncertainties in associating low momentum tracks, because the requirement of time-coincidence with the leading muon reduces the background due to spurious associations to a completely negligable level.

In the neutrino sample 10 $\mu^-\mu^+$, 1 $\mu^-\mu^+\mu^-$ and 3 $\mu^-\mu^-$ events were found. 2 $\mu^+\mu^-$ events were found in the antineutrino sample. No $\mu^+\mu^+$ events were found. As stated in Chapter IV the main background of falsely identified muons comes from undetected $\pi_{\mu 2}$ and $K_{\mu 2}$ decays in flight, the muon subsequently reaching the EMI. Also hadrons which leave the visible chamber volume without interacting will shower inside the iron absorber and one of the secondary tracks from the shower may penetrate to the EMI close to the position of an extrapolated hit of one of the muon

candidate tracks. These effects have been estimated by a Monte Carlo program[19] which contains a complete description of the structure of BEBC and the surrounding material. Monte Carlo events are generated using known multiplicity distributions, particle spectra, P_T distributions etc., in accordance with the energy distribution of the narrow band beam. Tracks are followed in small steps, the contributions of energy loss and multiple scattering being added at each step. The probability of decay or interaction is tested at each step. All tracks are followed until they interact or stop. Interactions are generated to exactly conserve energy, momentum, charge and baryon number.

The background of false dimuons expected in this experiment are 2.7 $\mu^-\mu^+$ and 1.7 $\mu^-\mu^-$ events in neutrinos, 0.5 $\mu^+\mu^-$ and 0.4 $\mu^+\mu^+$ in antineutrinos. Assuming there is one charged kaon per dimuon event the contribution of trimuon events due to dimuons with an additional unseen $K_{\mu 2}$ decay has been estimated to be 0.2 events. The observed trimuon has been included in the dimuon sample.

V.3 Event Rates

The main features of all the di-lepton events found having a right sign muon and at least one other lepton and a total visible energy greater than 10 GeV are listed in Table 5.1. It should be noted that the $\mu^-\mu^-$ event number 12 in the table has been eliminated as a dimuon since a careful examination of the vertex region under high magnification has revealed that the secondary muon track in

Table 5.1

Beam	Event	Type	E_{vis} (GeV)	p_1 (GeV/c)	p_2 (GeV/c)	x_{vis}	y_{vis}	$\Delta\phi$ (degrees)	$p_{2\perp\mu\nu}$ (GeV/c)	Strange particles	p_{K^o} (GeV/c)	m_{K^o} (GeV/c^2)
ν	1	$\mu^-\mu^+$	39	9.9	11.0	0.016	0.25	62	-0.52	K^o_s, $K^+_{\pi 3}$	7.95	1.45
	2	$\mu^-\mu^+\mu^-$ (a)	50	14.9	4.2	0.19	0.71	8	-0.023	-	-	-
	3	$\mu^-\mu^+$	55	32.3	13.5	0.07	0.41	27	-0.19	-	-	-
	4	"	59	37.7	10.1	0.13	0.35	180	0.01	K^o_s	3.14	2.17
	5	"	84	54.9	7.4	0.20	0.35	169	-0.25	K^o_s/Λ	6.70	1.29
	6	"	95	43.4	8.0	0.29	0.59	157	0.17	K^o_s/n^*	3.3	1.02
	7	"	100	55.7	7.0	0.07	0.44	123	0.47	-	-	-
	8	"	104	35.0	52.0	0.06	0.66	179	0.012	K^o_s	5.7	1.85
	9	"	132	112.8	6.9	0.07	0.13	145	-0.42	-	-	-
	10	"	184	80.4	14.4	0.12	0.56	180	0.002	K^o_s	11.7	1.06
	11	"	193	85.7	24.9	0.40	0.55	164	-0.26	-	-	-
		average	99.5	51.2	14.5	0.15	0.46	127	-0.091		6.4	1.47
	12	$\mu^-\mu^-$	86	7.6	5.7	0.25	0.91	99	0.43	-	-	-
	13	"	122	13.5	10.4	0.002	0.89	28	-0.98	-	-	-
	14	"	144	44.4	15.6	0.03	0.69	136	-0.18	-	-	-
		average	117	21.8	10.6	0.09	0.83	88	-0.25			
	15	μ^-e^+	59	18.6	9.6	0.14	0.70	133	0.21	K^o_s, $K^+_{\mu 2}$ (b)	9.5	0.94
	16	"	70	24.1	7.3	0.03	0.63	95	-0.49	-	-	-
	17	"	75	43.8	0.73	0.80	0.39	63	-0.16	K^o_s	7•3	0•88
	18	"	129	113.0	3.5	0.01	0.14	171	-0.02	-	-	-
	19	"	132	54.2	27.5	0.09	0.60	85	0.18	-	-	-
		average	93	50.7	9.7	0.21	0.49	109	-0.056		8.4	0.91
		average ($\mu^-\ell^+$)	97	51.0	13.0	0.17	0.47	121	-0.08		6.8	1.32
$\bar{\nu}$	20	$\mu^+\mu^-$	33	16.8	6.2	0.15	0.46	165	-0.04	-	-	-
	21	"	67	16.4	30.7	0.21	0.84	153	-0.61	-	-	-
	22	μ^+e^-	73	46.7	8.1	0.01	0.36	155	-0.53	K^o_s (c)	12.5	1.56
		average	58	26.6	15.0	0.12	0.55	158	-0.39			

(a) The momentum of the slow μ^- is 6.7 GeV/c. The event is included in the di-muon sample.
(b) This event has in addition a slow K^o_s decaying within < 5 mm from the vertex.
(c) A second K^o_s points to a secondary neutral interaction consistent with K^o_L production.

	$\frac{\mu\mu}{\mu}$ %	$\frac{\mu e}{\mu}$ %		$\frac{\mu\mu + \mu e}{\mu}$ %	$\frac{\mu\mu K^o + \mu e\ K^o}{\mu\mu + \mu e}$
	$p_{\mu 2} > 4$ GeV/c	$p_e > 0.3$ GeV/c	$p_e > 4.0$ GeV/c	$p_2 > 4$ GeV/c	$p_{\mu 2} > 4$ GeV/c $p_e > 0.3$ GeV/c
ν	0.8 ± 0.3	0.7 ± 0.3	0.5 ± 0.4	[illegible] ± 0.4	1.7 ± 0.7
$\bar{\nu}$	0.8 ± 0.6	0.6 ± 0.6		1.2 ± 0.7	1.0 ± 1.0

Table 5.2

fact undergoes a three-prong secondary interaction very close to the production vertex. Two of the three prongs appear to be stopping protons. The third track leaves the bubble chamber without undergoing any further interaction and is subsequently identified by the EMI. It is worthwhile to mention that the χ^2 for acceptance of this track as a muon was on the limit and this event was a borderline case anyway. This feature was discovered during a check on all di-lepton events for a possible gap between a di-lepton vertex and the neutrino event vertex due to the decay of a neutral long-lived heavy lepton. No other event was thrown into doubt by this check.

The rates for di-lepton events, corrected for identification efficiencies and backgrounds, relative to charged current rates are given in Table 5.2. Assuming a common production mechanism (charm) for the $\mu\mu$ and μe events the rates can be combined. Table 5.2 also shows the combined $\mu\mu$ + μe rate with a cut of 4 GeV/c on the electron momentum in the μe events. This cut also reduces the μe background to a negligible level.

Of the opposite sign di-lepton events eight out of the sixteen due to neutrinos and one of the three due to antineutrinos have an associated V^o. Seven of these fit a K^o_s, one is ambiguous between K^o_s and Λ^o and another is ambiguous between a decay and the interaction of a neutral hadron. All the V^o's were found during the general scanning of all the film before the special search for direct electrons and before the EMI analysis of the data. None of the same

sign dimuons has an associated V^o. In computing the K^o rates for di-leptons given in Table 5.2 the two ambiguous V^o's have each been counted as 0.5 K^o. The rate is corrected for the branching fraction into unseen decay modes (31%), losses due to unobserved short distance decays and interactions (10%) and an equal contribution of unobserved K_L^o.

V.4 Quark Parton Model Predictions for Di-Lepton Production

In Chapter I the cross-sections for elementary scattering processes of neutrinos and quarks were discussed (Equations (1.30), (1.31)). Integrating over x and y we have for the total charged current cross-sections :

$$\sigma_{cc}^{\nu} = \frac{G^2 M E_\nu}{\pi} \left[\int_0^1 q(x)\, dx + 1/3 \int_0^1 \bar{q}(x)\, dx \right] \qquad (5.1)$$

$$\sigma_{cc}^{\bar{\nu}} = \frac{G^2 M E_{\bar{\nu}}}{\pi} \left[\int_0^1 \bar{q}(x)\, dx + 1/3 \int_0^1 q(x)\, dx \right] \qquad (5.2)$$

where q(x) contains the contributions of all quarks (valence and sea), i.e. $q(x) = x(u(x) + d(x) + s(x) + \ldots.)$. Previously we ignored the Cabbibo mixing[29] in considering the basic scattering processes, effectively setting Cos θ_c equal to one. In the 4-quark GIM model[30] the basic doublets of u,d,s and c quarks are mixed according to :

$$\begin{pmatrix} u \\ d \cos\theta_c + s \sin\theta_c \end{pmatrix} \quad \begin{pmatrix} c \\ s \cos\theta_c - d \sin\theta_c \end{pmatrix} .$$

The amplitudes for the elementary scattering processes are multiplied by Cos θ or Sin θ as appropriate and hence the (incoherent) contributions to the cross-section become :

$$\nu + d \rightarrow \mu^- + u \quad \propto \quad x\,d(x)\cos^2\theta_c$$

$$\nu + d \rightarrow \mu^- + c \quad \propto \quad x\,d(x)\sin^2\theta_c$$

$$\nu + s \rightarrow \mu^- + u \quad \propto \quad x\,s(x)\sin^2\theta_c$$

$$\nu + s \rightarrow \mu^- + c \quad \propto \quad x\,s(x)\cos^2\theta_c$$

with similar contributions for antineutrinos.

Given assumptions for the various quark momentum distributions it is straightforward to predict the relative proportion of charm production to the total charged current cross-section. Field and Feynman's assumption for the distribution of quark momenta in the proton[31] are probably reasonable for our energy range. They are :

$$\int x\,\bar{u}\,dx \simeq \int x\,\bar{d}\,dx \simeq 2\int x\,\bar{s}\,dx \simeq 0.04\int x\,(u+d)\,dx \qquad (5.3)$$

and

$$\int x\,\bar{c}\,dx = 0. \qquad (5.4)$$

Since a proton must have $\int x\,u\,dx \simeq 2\int x\,d\,dx$, Equation (5.3) implies $\int x\,\bar{u}\,dx \simeq 0.04\int x\,(3d)\,dx$.

For an isoscalar target which has 1.5 times as many d quarks as a proton target the corresponding relation becomes :

$$\int x\,\bar{u}\,dx = 0.04\int x\,(2d)\,dx. \qquad (5.5)$$

Considering all possible elementary neutrino-quark scattering processes and using Equations (5.1) and (5.2) leads to :

$$\frac{\sigma_{cc}^{\nu N \to \text{charm}}}{\sigma_{cc}^{\nu N \to \text{All}}} = \frac{\int x\, d(x)\, dx\, \text{Sin}^2\theta_c + \int x\, s(x)\, dx\, \text{Cos}^2\theta_c}{\int x\, d(x)\, dx + \int x\, s(x)\, dx + 1/3 \int x\bar{u}(x)dx} \qquad (5.6)$$

$$\frac{\sigma_{cc}^{\bar{\nu}N \to \text{charm}}}{\sigma_{cc}^{\bar{\nu}N \to \text{All}}} = \frac{\int x\, \bar{d}(x)\, dx\, \text{Sin}^2\theta_c + \int x\, \bar{s}(x)\, dx\, \text{Cos}^2\theta_c}{\int x\, \bar{d}(x)\, dx + \int x\, \bar{s}(x)\, dx + 1/3 \int x\bar{u}(x)dx} \qquad (5.7)$$

Taking $\text{Sin}^2\theta_c = 0.05$ and using relations (5.3) to (5.5) in Equations (5.6) and (5.7) gives values of 8% and 9% for the amount of charm production by neutrinos and antineutrinos respectively.

If we further assume that the di-lepton events observed are due to the semi-leptonic decay of charmed hadrons produced in charged current events by the Cabbibo favoured processes :

$$c \to s + \ell^+ + \nu \qquad (5.8a)$$

$$\bar{c} \to \bar{s} + \ell^- + \bar{\nu} \qquad (5.8b)$$

we can calculate the strange particle multiplicity to be expected in di-lepton events (ignoring any associated production of strangeness in the hadronic cascade). The decays 5.8 give rise to one strange particle in the final state and for charm production off the strange component of the sea there is another

strange particle due to the accompanying strange quark or antiquark remaining. For antineutrinos (anti) charm production occurs only off the sea and since $\bar{d} \rightarrow \bar{c}$ is Cabbibo suppressed charm production is predominantly off $\bar{s}$ quarks leading to two strange particles in the final state. In the case of charm production from neutrinos the Cabbibo suppressed contribution from the d valance quarks is comparable to the contribution from s quarks giving an average of about 1.4 strange particles per event.

V.5 Interpretation of Di-Lepton Events

As has been outlined in Sections (V.2) and (V.3) the majority of the di-lepton events found cannot be explained by conventional background sources. In this Section the characteristics of the events will be further examined in order to determine their origin. A number of possible origins can be ruled out very quickly :

(a) The flat effective mass spectrum of the two muons for the opposite sign dimuon events (Fig. 5.2a)) rules out the possibility of the production and decay of a narrow resonance as the source. In any case, this would not contribute to the μe events.

(b) The production of a neutral heavy lepton which subsequently decays leptonically (Fig. (5.1a)) can be ruled out by the asymmetry in the observed lepton momenta. Pais and Treiman[32] have produced limits on the momentum asymmetry for the case of any neutral heavy spin $\frac{1}{2}$ lepton which decays

POSSIBLE PRODUCTION MECHANISMS FOR DI-LEPTON EVENTS

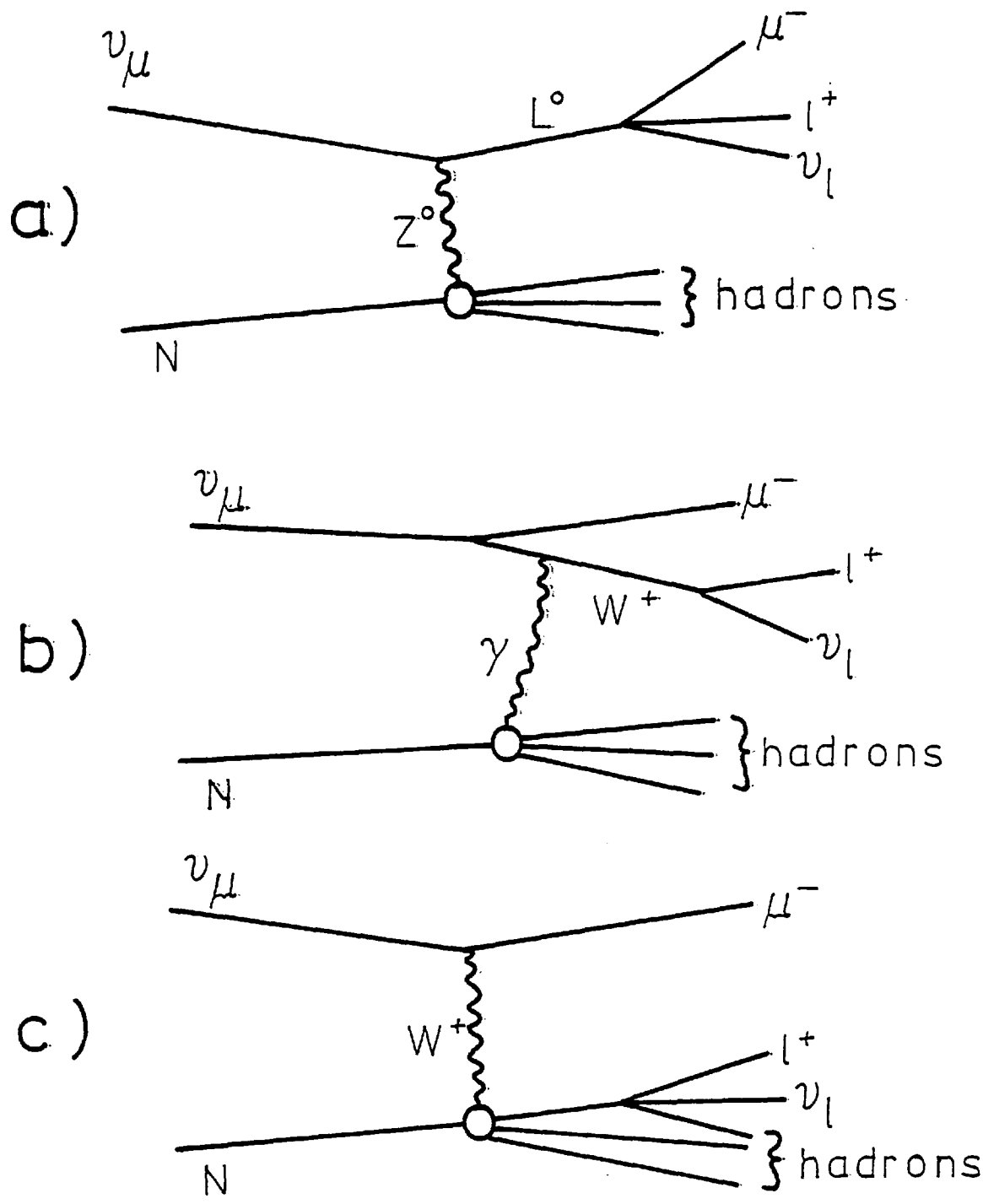

FIG. 5.1

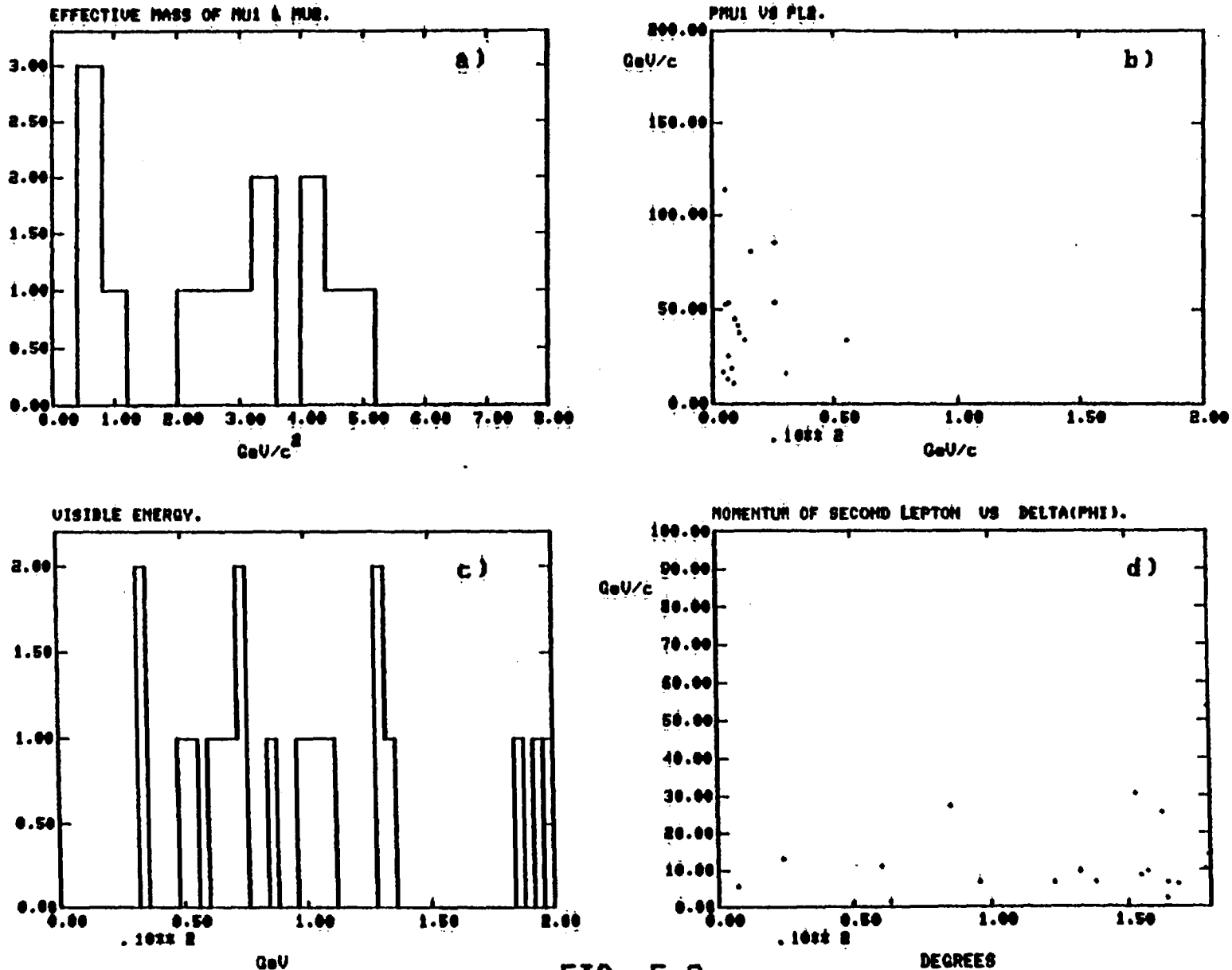
EFFECTIVE MASS OF MU1 & MU2.
a)
3.00
2.50
2.00
1.50
1.00
0.50
0.00
0.00 1.00 2.00 3.00 4.00 5.00 6.00 7.00 8.00
GeV/c²
PMU1 VS PL2.
b)
200.00
GeV/c
150.00
100.00
50.00
0.00
0.00 0.50 1.00 1.50 2.00
.10** 2
GeV/c
VISIBLE ENERGY.
c)
2.00
1.50
1.00
0.50
0.00
0.00 0.50 1.00 1.50 2.00
.10** 2
GeV
MOMENTUM OF SECOND LEPTON VS DELTA(PHI).
d)
100.00
90.00
GeV/c
80.00
70.00
60.00
50.00
40.00
30.00
20.00
10.00
0.00
0.00 0.50 1.00 1.50
.10** 2
DEGREES

FIG. 5.2

as $L^0 \to \mu^+\mu^-\nu_\mu$. Using a form of interaction with all possible couplings (V,A,S,P,T) and arbitrary strengths they find :

$$(9 - 4\sqrt{2})/7 \lesssim \langle p_\ell^- \rangle / \langle p_\ell^+ \rangle \lesssim (9 + 4\sqrt{2})/7 \ ,$$

i.e. $$0.48 \lesssim \langle p_\ell^- \rangle / \langle p_\ell^+ \rangle \lesssim 2.1.$$

The asymmetry found in this experiment is 3.9 ± 1.1. Figure (5.2b) shows the momentum of the leading muon plotted against the momentum of the second lepton.

(c) The large values of visible energy (Fig. (5.2c)) are inconsistent with the production of W^+ as in Figure (5.1b). At the threshold for W production events would be expected to have small values of hadronic energy.

The distribution of the difference in azimuthal angle of the two leptons in the plane perpendicular to the incoming neutrino direction is plotted against the momentum of the second lepton in Figure (5.2d). The tendency for the azimuthal angle difference, $\Delta\phi$, to be concentrated at values closer to the 180° than 0°, especially for large values of $p_{\ell 2}$, indicates an origin at the hadronic vertex for the second lepton. Figure (5.3) shows the transverse momentum distribution of the two leptons with respect to the direction of the meausred hadrons. Also shown for comparison are the P_T distribution of muons in ordinary charged current events and the P_T of individual hadrons with respect to the measured hadron direction. This further reinforces the idea

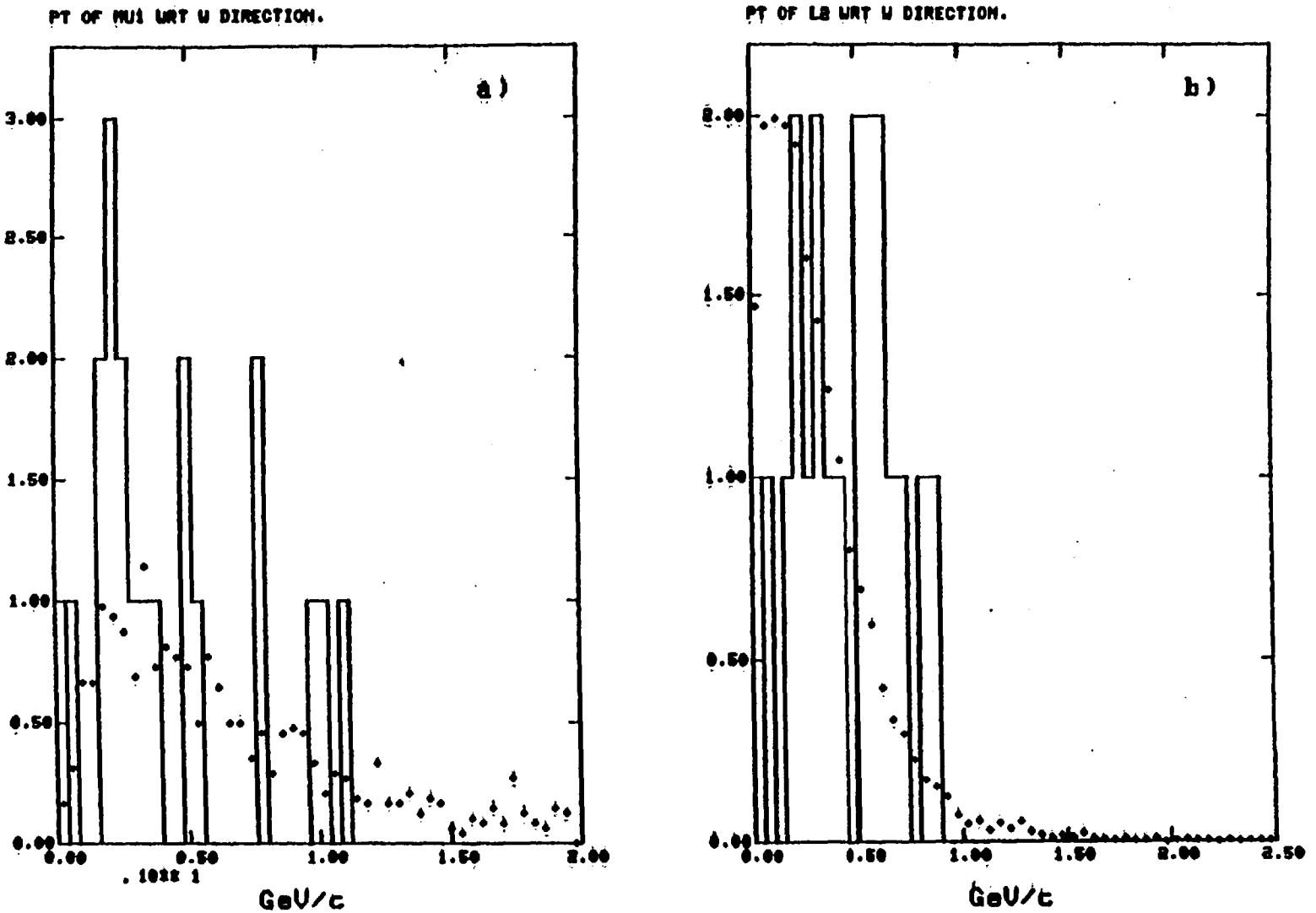
PT OF MUI WRT W DIRECTION.
a)
3.00
2.50
2.00
1.50
1.00
0.50
0.00
0.00
0.50
1.00
1.50
2.00
. 1012 1
GeV/c
PT OF LB WRT W DIRECTION.
b)
2.00
1.50
1.00
0.50
0.00
0.00
0.50
1.00
1.50
2.00
2.50
GeV/c

FIG. 5.3

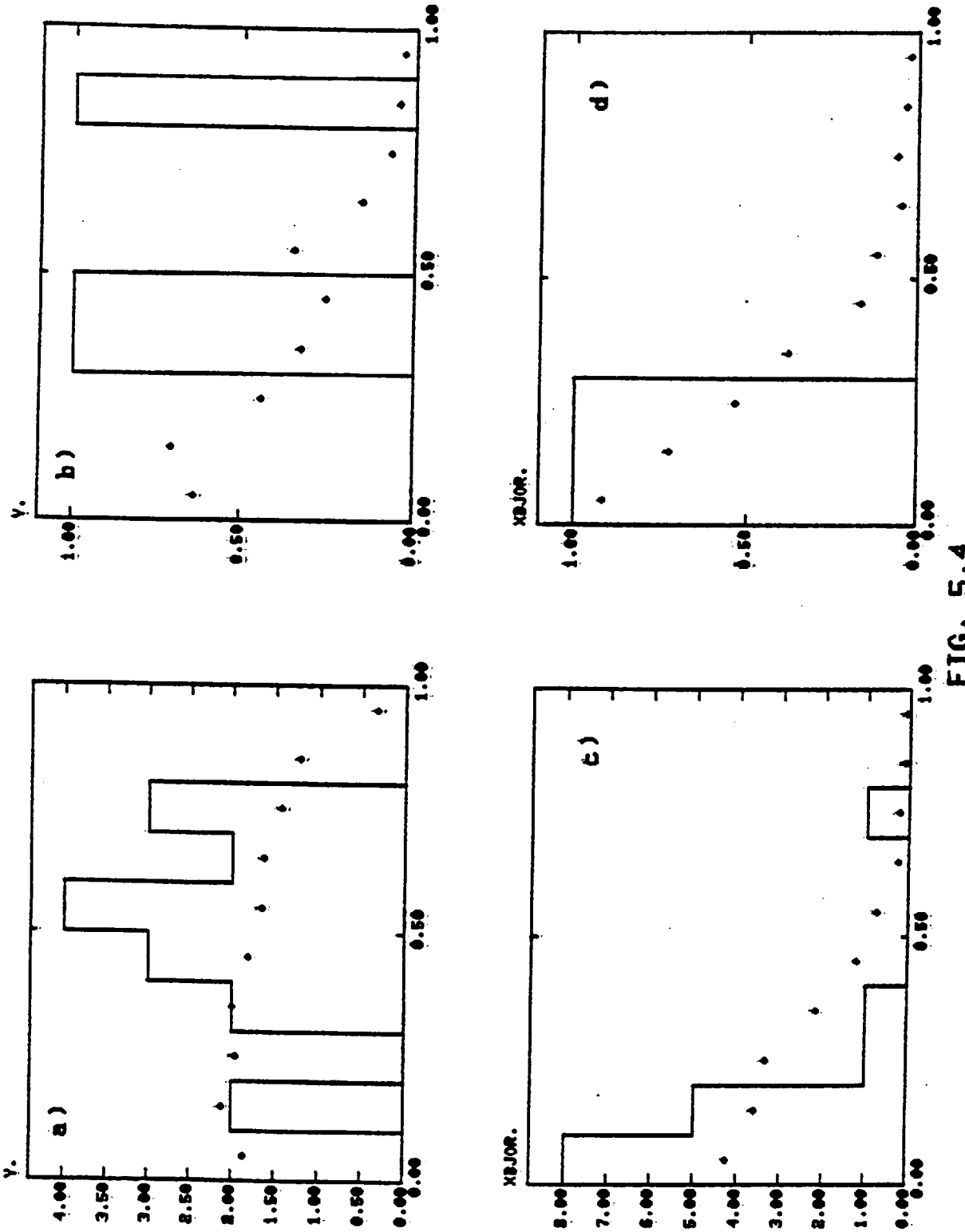

FIG. 5.4

† The distributions shown are calculated using visible energy only since the extra ν associated with the second lepton would invalidate the normal energy correction. To estimate the effect on the visible distributions due to this missing ν the relevant quantities have been recalculated using the momentum of the second lepton as a guess for the loss involved. The resulting distributions remain close to those shown (solid histograms) with only a slight shift to high y and low x.

that the leading muon is due to the usual charged current interaction, while the second lepton arises at the hadronic vertex from the semi-leptonic decay of an unstable hadron as shown in Figure (5.1c).

A QCD calculation by Goldberg[33] indicates that $c\bar{c}$ production by single gluon exchange is a factor of 10 too small to account for even the same sign dimuons and trimuons observed by the CDHS collaboration.[26,27] Figure (5.4)† shows the x and y distributions for the di-lepton events with the corresponding distributions for charged current data normalised to the same number of events superimposed. The y distribution for neutrino induced di-leptons is flat with a slight bias in favour of high y which would be expected just above the threshold for production of new hadrons. In the antineutrino case the three di-leptons found are also consistent with a flat y distribution which would be expected for production off the $\bar{s}$ component of the sea as predicted by the quark parton model description of Section V.4. Another expectation of the quark parton description is that substantial production off the sea would suppress the x distributions to small x values but this is far more difficult to show with the small number of events available.

The K^o multiplicity observed in the di-lepton events is a factor of 10 higher than that observed in ordinary cc events and is consistent with that expected from the naive argument presented above although the experimental value is a little high and still does not include any contribution from charged K's. Finally it has been noted[34,35]

† See footnote on page 107.

that if di-lepton events are due to the production and decay of charmed D mesons, then the three body decay mode :

$$D^+ \rightarrow \ell^+ \nu_e K^o \quad ,$$

allows an estimate of the D mass (assuming a similar matrix element as for K^+ decay) from the relation :

$$M_D = 1.5 < M_{\ell^+ K^o} > .$$

The value obtained from the di-lepton events with V^o's in this experiment is 1.98 GeV/c^2, reasonably close to the mass of the D meson.

V.6 Summary

Sixteen opposite sign di-lepton events due to neutrinos and three due to antineutrinos have been observed as a signal significantly above expected background levels. The events have been shown to be consistent with the production and semi-leptonic decay of charmed hadrons by a charged current interaction, both in absolute rate (assuming a 10 - 15% leptonic branching ratio) and in the characteristics of the events themselves. In particular the second lepton is shown to have an origin at the hadronic vertex and the V^o rate is broadly consistent with the expectations of a simple parton model calculation.

CHAPTER VI

Search for Retention of Quark Properties at the Hadronic Vertex

Data from e^+e^- annihilations [36], hadron - hadron collisions [37] and lepton - nucleon interactions (e p, νp) [38] have shown the production of "jets" of hadrons having small transverse momentum with repect to one another. These jets show similar characteristics and are generally believed to be the result of quark fragmentation, i.e. the cascade decay of a produced quark into stable hadrons. Much interest has been shown in the question of whether these jets retain the quantum numbers of the initiating quark, if such be their origin, and to what extent the flavour of this quark can be indentified.

VI.1 Model for Quark Jet Production

R.D. Field and R.P. Feynman [39] have produced a simple model for the production of quark jets. This model has a number of limitations and is not expected to be an accurate description of the evolution of real jets but it provides a reasonable parameterization of the properties of jets which have been observed so far and makes a number of predictions concerning the possibility of identifying a parent quark from the jet fragments.

The basic idea behind this model is that a quark produced in e^+e^- annihilation or scattered in a hadron - hadron collision etc creates a colour field causing the production of $q\bar{q}$ pairs between itself and the other interaction products (antiquark in e^+e^- processes or remaining valence quarks in hadron collisions). The

QUARK JET GENERATION SCHEME OF FIELD AND FEYNMAN

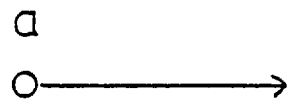

i)

Initial quark of flavour "a"

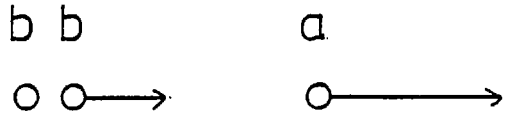

ii)

Quark-antiquark pair produced in colour field

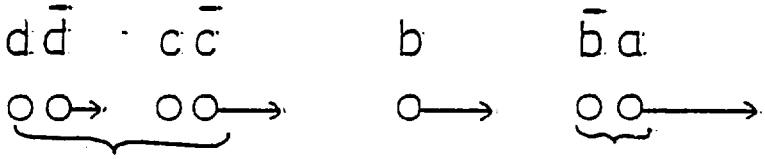

iii)

Further $q\bar{q}$ pairs of successively lower momentum.

Rank 1 primary meson of flavour $a\bar{b}$.

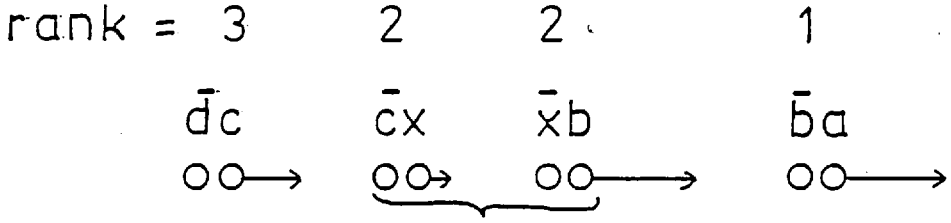

iv)

Decay products of unstable primary meson $b\bar{c}$

FIG. 6.1

antiquark of the produced $q\bar{q}$ pair will combine with the initial quark to form a meson which may be stable itself or which decays into stable mesons. Its accompanying quark will cause the generation of further $q\bar{q}$ pairs of progressively lower momentum until all the quarks and antiquarks are bound in stable hadrons (see Fig. 6.1). The last remaining quark must of course, re-combine with an antiquark or a di-quark from the target fragments. The model is parameterized by a function $f(\eta)$, the probability that the remaining jet (after the combination of a quark and antiquark to form a 'primary' meson) has a function η of the original jets momentum remaining to it. Further development of the jet proceeds in a recursive manner as an initial jet possessing the fraction η of the original momentum. Since the flavour of the produced $q\bar{q}$ pairs is random the further development of the jet is independant of the flavour of the original quark. Thus only the 'first rank' primary meson will have quantum numbers that deviate from those of the'mean quark'.

The rank of a produced meson, however, does not determine its order in rapidity. It is possible for a meson of lower rank to have higher momentum since the antiquarks of the produced pairs generally have higher momentum than the quarks , the quark contributing to a meson of lower rank than the antiquark. Only the sum of the $q\bar{q}$ momenta is required to decrease in successive ranks. This means that the fastest particle is a jet does not necessarily contain the original quark. As the fraction of the jets momentum carried by a single hadron increases, however, it becomes progressively more probable that it contains the original quark. Also the quantum numbers of the first rank primary meson will be modified by the properties of the mean antiquark it contains. The exact value depends on the relative probabilities of producing a $q\bar{q}$ pair of a particular flavour. Field and Feynman assume equal probabilities

for $u\bar{u}$ and $d\bar{d}$ production with $s\bar{s}$ suppressed by 50% by comparison. This leads, in the case of electric charge for example, to a mean antiquark charge of -1/15. Thus a jet originating from a u quark will have a mean charge of 0.6 and for a d quark or s quark - 0.4.

VI.2 Advantages of Jet Studies in νN scattering in Bubble Chambers

High energy neutrino interactions in bubble chambers are a good place to look for quark properties of hadronic jets for a number of reasons. In experiment WA19/22 all the charged products of neutrino interactions were measured with a momentum resolution of typically $\Delta p/p \lesssim 5\%$. Also about half the neutral secondaries were measured, although with larger uncertainties. Neutrino interactions have two advantages over e^+e^- or hadron - hadron collisons in this study. First, the flavour of the quark initiating the jet is known, as predominantly we have

$$\nu + d \to \mu^- + u$$

or $$\bar{\nu} + u \to \mu^+ + d$$

except for a small contribution from sea quarks. This allows us to study a clean sample of jets of known flavour and to compare with model predictions. Secondly, the jet direction is given by the dirction of the exchanged intermediate vector boson (the q-vector direction) whereas in e^+e^- annihilations no a-priori jet direction exists.

The agreement of the nucleon structure functions [4] with the quark model prediction $F_2^{\nu N} = 9/5 F_2^{ed}$ already gives support to the notion of fractionally charged quarks.

VI.3 Use of the Breit Frame for Separation of Quark Jets

In the study of quark jets produced in νN scattering the problem arises of how to separate the current fragmentation jet due to the struck quark from the target fragmentation jet due to the remaining valence quarks in the nucleon. Also, with interactions occurring in neon nucleii there is the added problem of nuclear disintegration leading mainly to the appearance of slow protons which do not belong to the current fragmentation jet, nor truly to the target fragmentation products. Nuclear fragments, however, would be expected to have an isotropic angular distribution with no correlation to the current direction. The angular distribution of slow protons in the event sample has been checked and on this basis all identified protons of less than 300 MeV/c momentum have been cut out of the analysis. (See Fig. 6.2.)

In order to separate the current fragmentation region from the target fragmentation region previous analyses [40] have imposed a cut on the variable z such that $z_i \geq 0.2$ for hadron i to be retained as part of the current fragmentation region, where

$$z_i = \frac{\text{energy of hadron i}}{\text{total hadronic energy.}} \qquad (6.1)$$

This cut, while easy to implement, is fairly arbitrary and lacks any theoretical motivation. In this analysis it has been chosen to impose a cut in the Breit frame of the q-vector and the scattered quark. (See Fig. 6.3). In this frame the momentum of the quark is reversed and, ignoring the mass difference between the incoming and

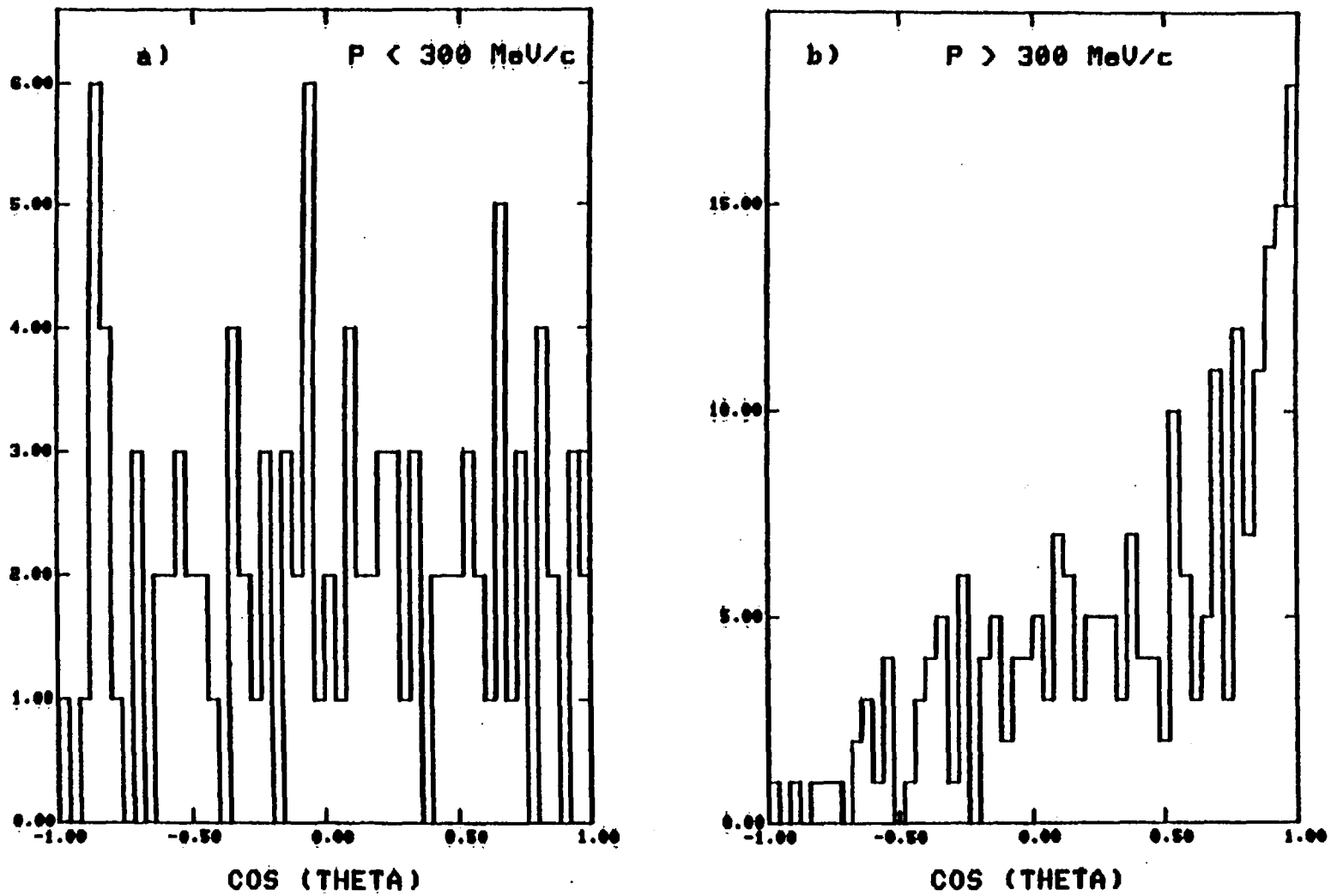
a)
P < 300 MeV/c
6.00
5.00
4.00
3.00
2.00
1.00
0.00
-1.00
-0.50
0.00
0.50
1.00
COS (THETA)
b)
P > 300 MeV/c
15.00
10.00
5.00
0.00
-1.00
-0.50
0.00
0.50
1.00
COS (THETA)

FIG. 6.2

PRODUCTION OF OPPOSITELY MOVING JETS IN THE BREIT FRAME

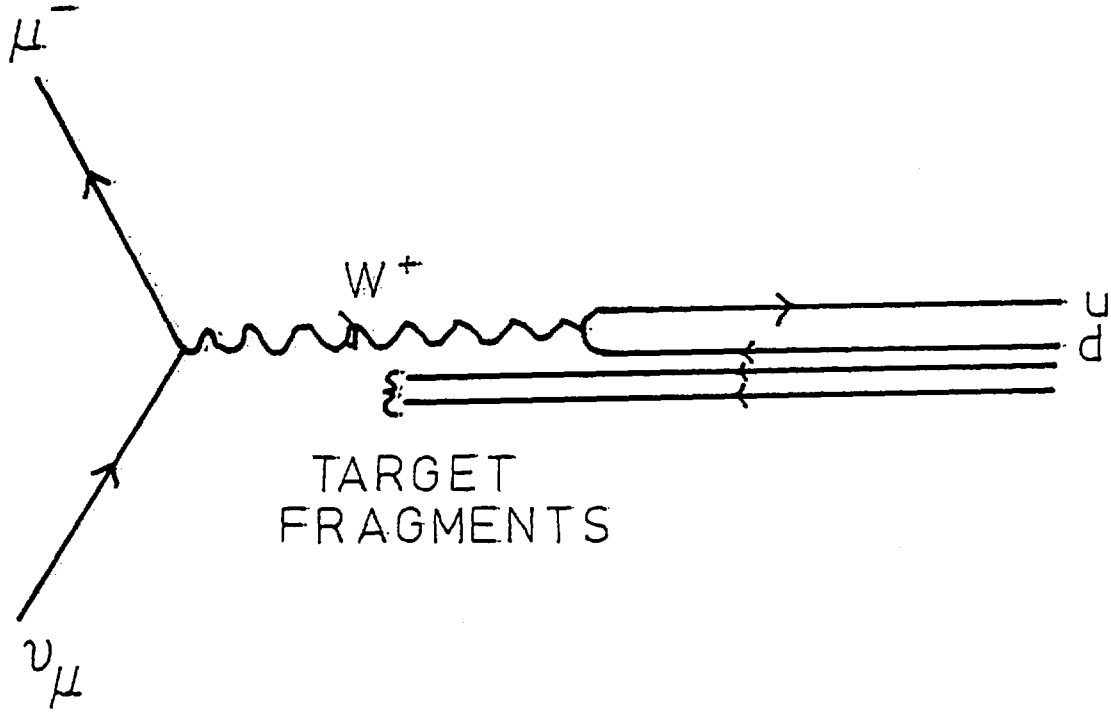

FIG. 6.3

outgoing quark, the energy transfer is zero. Therefore we have in this frame

$$q_0 = 0$$

where q_0 is the energy component of the 4 - momentum of the W^+. The lorentz transformation from the laboratory system is then given by

$$q_0 = (\nu - \beta |\underline{q}|) = 0$$

$$\text{i.e.} \quad \beta = \frac{\nu}{|\underline{q}|} \qquad (6.2)$$

where ν and $\underline{q}$ are the energy and momentum components of the 4 - momentum transfer in the lab frame as defined in chapter 1.

VI.4 Experimental Procedure and Cuts

Events selected for this analysis were required to have a muon of momentum $\geq$ 5 GeV/c identified by the EMI and of the correct charge (negative in neutrino interactions, positive in antineutrino). The total event energy was required to be at least 20 GeV and events with tracks of undetermined charge were rejected. Protons below 300 MeV/c were rejected as described above. Any remaining tracks with $\Delta p/p \geq 0.3$ were rejected. Such tracks are normally ones which have a secondary interaction after a short distance and are assigned unrealistically high momenta. Also for interacting tracks the value of $\Delta p/p$ was checked to be compatible with the sagitta obtained from the momentum and the measured length. This was done because of a small proportion of tracks which were known to have unreasonally small values of $\Delta p/p$. For these tracks a minimum momentum, p_{min}., was calculated assuming a minimum measurable sagitta of 0.5 mm and taking into account the measured length. If the measured momentum was smaller than p_{min} it was set equal to p_{min} and the error on the momentum set equal to $0.25 \times p_{min}$. This small correction was applied to less than one per cent of the tracks in the analysis. The hadronic energy obtained from

the sum of the retained tracks was corrected by a factor 1.2 to compensate for missing neutral energy as described in chapter three.

Q^2 for the events and (ν, q) of equation 6.2 were defined using the corrected hadronic energy, the measured energy and momentum of the muon and the known direction of the neutrino beam. A further cut was imposed at this stage of $Q^2 \geq 2$ GeV^2/c^2 since parton model predictions are not believed to be valid at very low Q^2. All hadron tracks were then transformed to the Breit frame using the boost given by equation 6.2. In common with previous analyses [40] the direction of the momentum transfer was taken to be along the direction of the measured hadronic momentum. The boost was performed along this direction. This was done in order to eliminate any asymmetries which would be introduced by having an incorrect hadronic energy correction for each individual event. As described in chapter three the energy correction factor has an r.m.s. spread of 20%. However, a check was made using the direction of $\underline{q}$ defined by the neutrino and muon directions and no significant difference in the results was observed. For each track in the Breit frame the quantity $z\ p_L$ was defined by

$$z\ p_L = \frac{2.0 \times p_L}{\sqrt{Q^2}} \qquad (6.3)$$

where p_L is the component of the tracks momentum along the direction of Q. Referring to figure 6.3 it can be seen that in the Breit frame, ignoring mass differences between quarks, the momentum of the forward jet predicted by the parton model is equal to $\sqrt{Q^2}/2$ where the momentum of the Q-vector is given by $\sqrt{Q^2}$ since the energy transfer is zero in this frame. Therefore the quantity z_{pL} given by equation 6.3 corresponds to the definition of z in the jet parametrization of Field and Feynman [39] and takes on values between zero and one. Tracks having values of $z_{pL} < 0$ are considered to be part of the target fragmentation jet and are excluded from the rest of the analysis.

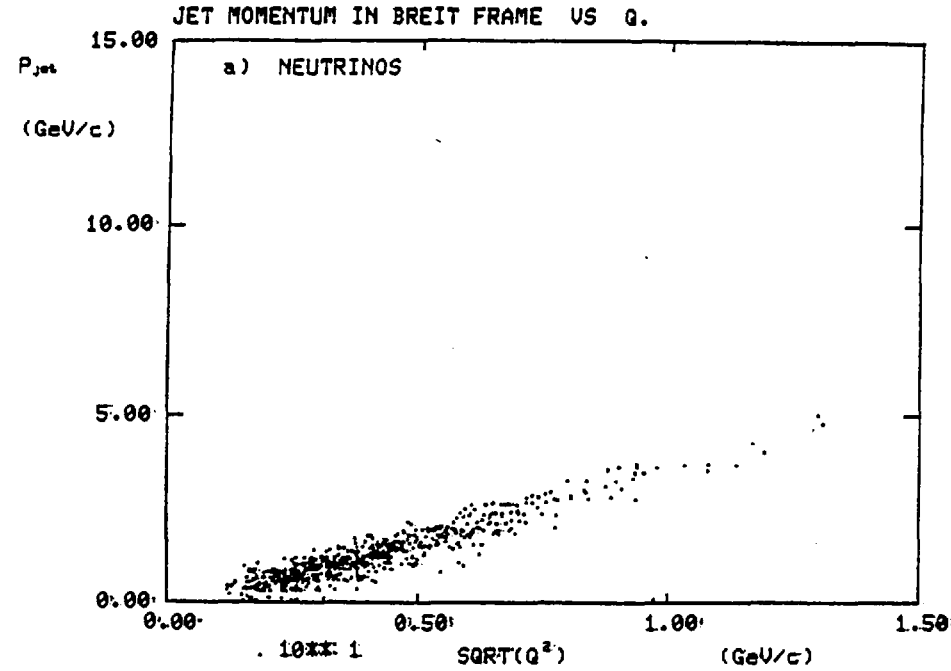
JET MOMENTUM IN BREIT FRAME VS Q.
a) NEUTRINOS
P_{jet}
(GeV/c)
15.00
10.00
5.00
0.00
0.00
0.50
1.00
1.50
. 10** 1
SQRT(Q^2)
(GeV/c)

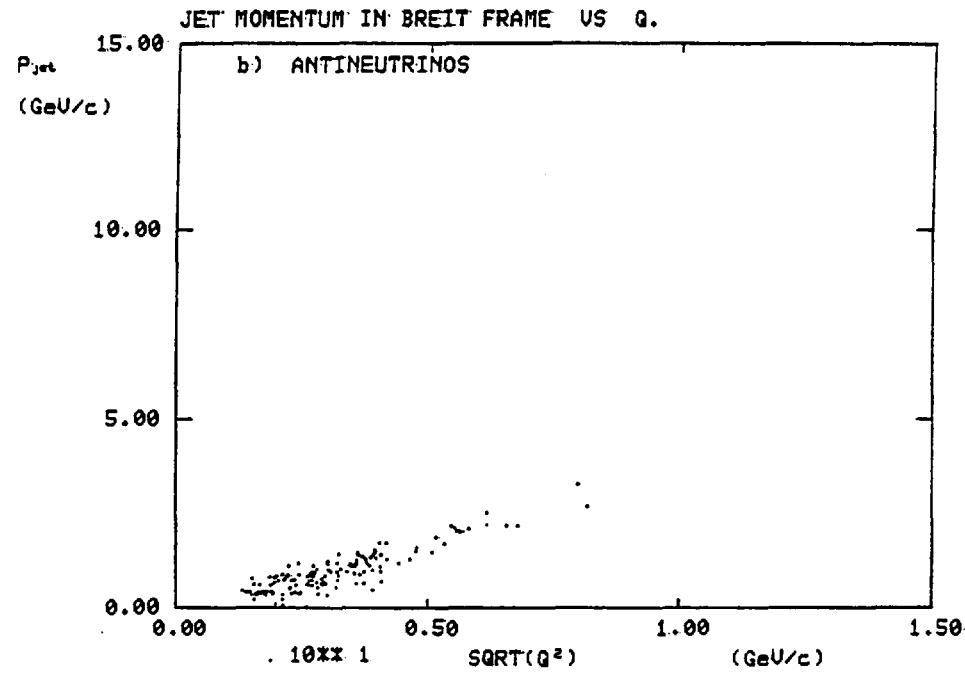
JET MOMENTUM IN BREIT FRAME VS Q.
b) ANTINEUTRINOS
P_{jet}
(GeV/c)
15.00
10.00
5.00
0.00
0.00
0.50
1.00
1.50
. 10** 1
SQRT(Q^2)
(GeV/c)

FIG. 6.4

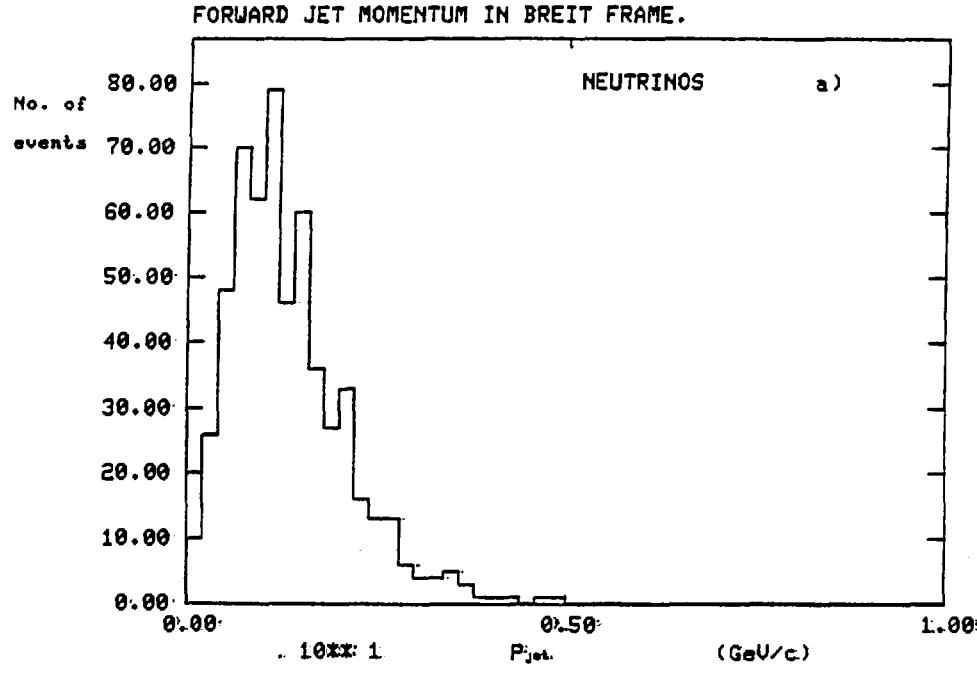
FORWARD JET MOMENTUM IN BREIT FRAME.
NEUTRINOS
a)
No. of events
80.00
70.00
60.00
50.00
40.00
30.00
20.00
10.00
0.00
0.00
0.50
1.00
. 10** 1
P_jet
(GeV/c)

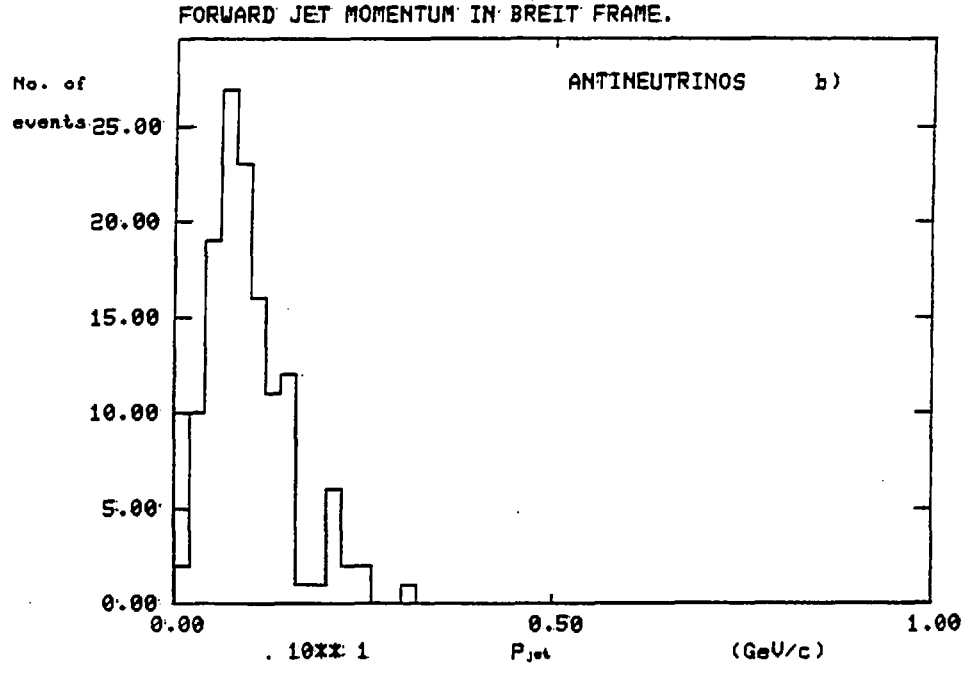
FORWARD JET MOMENTUM IN BREIT FRAME.
ANTINEUTRINOS
b)
No. of events
25.00
20.00
15.00
10.00
5.00
0.00
0.00
0.50
1.00
. 10** 1
P_jet
(GeV/c)

FIG. 6.5

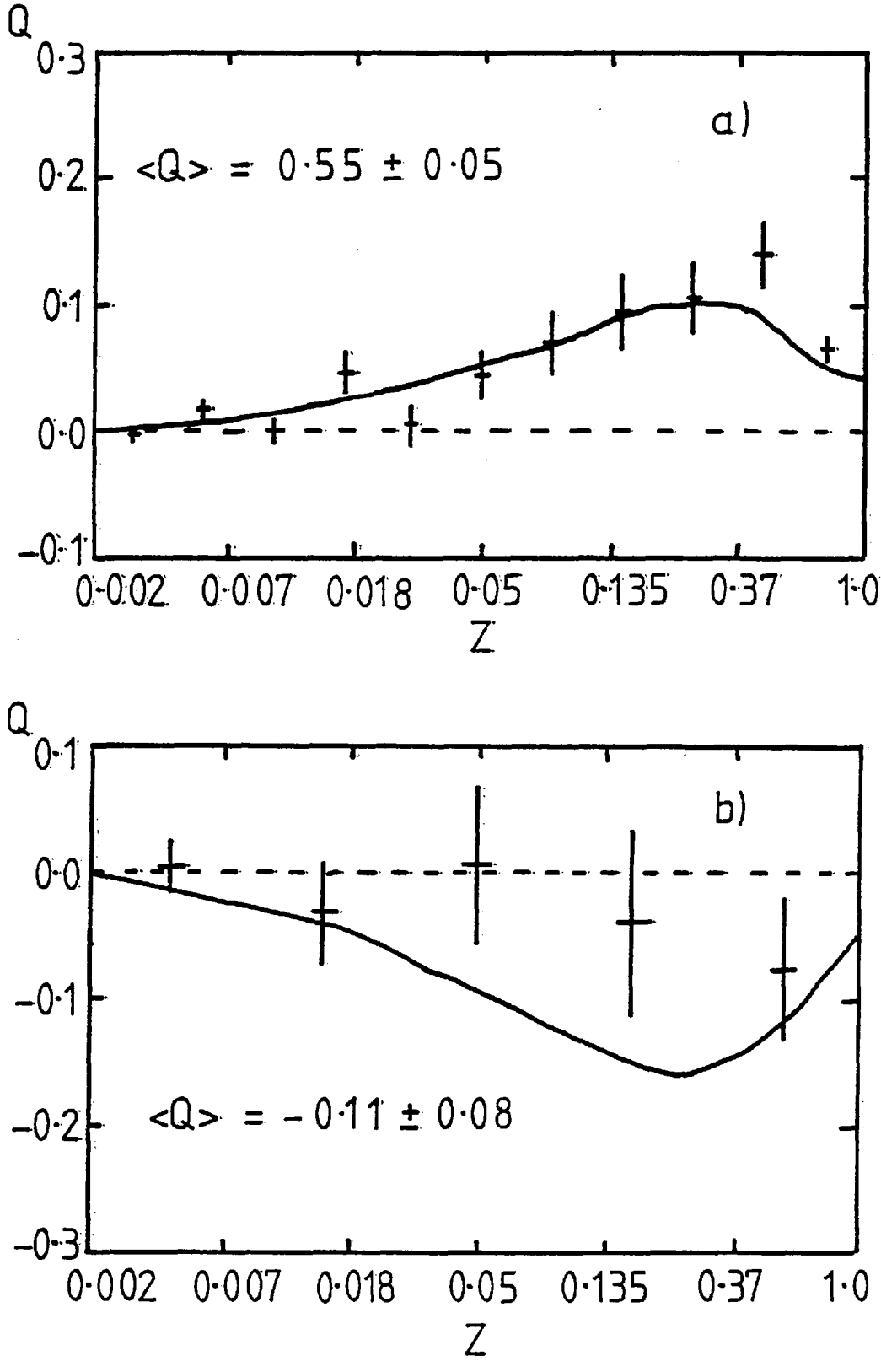
Q
0·3
0·2
0·1
0·0
−0·1
a)
<Q> = 0·55 ± 0·05
0·002
0·007
0·018
0·05
0·135
0·37
1·0
Z
Q
0·1
0·0
−0·1
−0·2
−0·3
b)
<Q> = −0·11 ± 0·08
0·002
0·007
0·018
0·05
0·135
0·37
1·0
Z

FIG. 6·6

Figure 6.4 shows the total momentum of the forward jet so defined against $\sqrt{Q^2}$ for neutrinos and antineutrinos. The parton model prediction would be for the points to lie on a straight line with a slope of $\frac{1}{2}$. The actual slope observed is close to 1/3 and the discrepancy is probably explained as resulting from the missing energy in the event. The correction factor needed to make the slopes agree with the parton model prediction would be 1.5 in this case. The larger correction factor is explainable as being due to the fact that the missing energy of the event is mainly accounted for by fast forward particles. This loss would be enhanced by the process of selecting the forward jet. Figure 6.5 shows the distribution of momenta of the forward jets selected in the neutrino and antineutrino samples. Note that the mean momentum in both cases is much lower than the 10 GeV of the monte-carlo jets of ref. 39. Figure 6.6 shows the distribution of charge versus $\ell n\ (\Sigma\ p_L)$ for events with $x_B \geq 0.1$ where x_B is the Bjorken scaling variable defined in equation 1.6. The curves are the monte-carlo prediction of ref. 39. The mean charge of the forward jet is found to be 0.553 ± 0.046 for neutrino and -0.113 ± 0.082 for antineutrino in reasonable agreement with the predicted values.

Additional predictions are made concerning the variation of observed jet charge with the number of particles in the jet. Table 6.1 shows the numbers of events observed with various numbers of charged particles for total jet charges which are greater than, less than, or equal to zero. The mean charge is also shown. The event numbers are scaled up to correspond to 10 thousand events for comparison with the jet model. The raw event numbers are also given in order to indicate the statistical limitations inherent in the data. Table 6.2 shows the same for antineutrinos.

COMPARISON OF EVENT CHARGE DISTRIBUTION FOR NEUTRINO EVENTS WITH JET MODEL PREDICTION FOR A U - QUARK JET

($z \geq 0.1$)

CHARGED PARTICLE TOPOLOGY	EVENT CHARGE	RAW EVENT TOTAL	NORMALISED EVENT TOTAL	JET MODEL PREDICTION FOR U - QUARK JET
ALL EVENTS	Q > 0	297	5121	4178
	Q < 0	83	1431	1722
	Q = 0	200	3448	3560
	< Q >	0.52	0.52	0.39
NCH = 1	Q > 0	98	1690	2624
	Q < 0	24	414	936
	< Q >	0.61	0.61	0.47
NCH = 2	Q > 0	58	1000	871
	Q < 0	21	362	229
	Q = 0	143	2466	2383
	< Q >	0.33	0.33	0.37
NCH = 3	Q > 0	102	1759	1101
	Q < 0	27	466	512
	< Q >	0.75	0.75	0.47
NCH = EVEN	Q > 0	85	1466	963
	Q < 0	25	431	260
	Q = 0	177	3052	2607
	< Q >	0.43	0.43	0.37
NCH = ODD	Q > 0	212	3655	3745
	Q < 0	58	1000	1462
	< Q >	0.67	0.67	0.47

TABLE 6.1

COMPARISON OF EVENT CHARGE DISTRIBUTION FOR ANTINEUTRINO EVENTS WITH JET MODEL FOR D - QUARK JETS

($Z \geq 0.1$)

CHARGED PARTICLE TOPOLOGY	EVENT CHARGE	RAW EVENT TOTAL	NORMALISED EVENT TOTAL	JET MODEL PREDICTION FOR D - QUARK
ALL EVENTS	Q > 0	27	2160	2110
	Q < 0	41	3280	3767
	Q = 0	57	4560	4123
	< Q >	- 0.14	- 0.14	- 0.21
NCH = 1	Q > 0	10	800	1205
	Q < 0	19	1520	2120
	< Q >	- 0.31	- 0.31	- 0.28
NCH = 2	Q > 0	6	480	309
	Q > 0	6	480	651
	Q = 0	35	2800	2557
	< Q >	0.0	0.0	- 0.19
NCH = 3	Q > 0	11	880	551
	Q < 0	13	1040	918
	< Q >	- 0.08	- 0.08	- 0.33
NCH = EVEN	Q > 0	6	480	345
	Q < 0	9	720	710
	Q = 0	45	3600	2792
	< Q >	- 0.10	- 0.10	- 0.19
NCH = ODD	Q > 0	21	1680	1765
	Q < 0	32	2560	3057
	< Q >	- 0.21	- 0.21	- 0.29

TABLE 6.2

In order to find a prescription for identifying the flavour of the initial quark in individual events Field and Feynman define a "weighted" charge which places more emphasis on the fast (high z) particles than the slower particles. The purpose of this is to try to reduce the fluctuations in total jet charge caused by the recombination of the slowest quark with an antiquark or di-quark belonging to the target fragments. The weighted charge is defined as

$$Qw\ (p) = \sum_i q_i\, e^{-(p\, Y_{Z_i})} = \sum_i z_i^p\, q_i \qquad (6.4)$$

where q_i is the charge of the i th particle and p is a variable parameter to be optimised for the most efficient and reliable separation of different quark flavours. The quantity Y_z is the so called "z - rapidity" defined by

$$Y_z = -\ln\ (z) \quad . \qquad (6.5)$$

Table 6.3 and figure 6.7 show the comparison with the jet model for values of p of 0.2 and 0.5 with and without a z cut and the actual distribution obtained for neutrinos and antineutrinos. Also shown are results obtained by defining Qw (P) for all tracks in the lab frame in order to determine whether this method successfully eliminates the effect of the target fragments. In this case events were selected having a total corrected hadronic energy, E_H, such that $5 < E_H < 40$ GeV as the jet calculation is for events of 10 GeV.

It can be seen from figure 6.8 that the distribution of weighted charge determined using lab quantities shows much more evidence for a clear single peaked structure than that determined in the Breit frame. This is accountable by the reduced multiplicity obtained by taking only forward tracks in the Breit frame leading to larger statistical fluctuations. However, table 6.3 demonstrates

COMPARISON OF FIELD AND FEYNMAN WEIGHTED CHARGE (NEUTRINOS)

WEIGHTED CHARGE	ALL z LAB FRAME $z_i = E_i/E_H$ $5 \leq E_H \leq 40$ GeV	NORMALISED EVENT Nos. (BREIT FRAME)	STANDARD U - QUARK JETS
$Q_w \geq 0$	9072	7103	7179
$P = 0.2$ $Q_w < 0$	928	2897	2737
$\langle Q_w \rangle$	0.94	0.44	0.39
σ rms			0.68
$Q_w \geq 0$	8428	7138	7172
$P = 0.5$ $Q_w < 0$	1572	2862	2762
$\langle Q_w \rangle$	0.49	0.34	0.26
σ rms			0.43
	$z \geq 0.1$		
$Q_w \geq 0$	7165	7034	6172
$P = 0.2$ $Q_w < 0$	2835	2966	2875
$\langle Q_w \rangle$	0.43	0.43	0.34
σ rms			0.76
$Q_w \geq 0$	7152	7069	6168
$P = 0.5$ $Q_w < 0$	2848	2931	2879
$\langle Q_w \rangle$	0.30	0.34	0.24
σ rms			0.52

TABLE 6.3 a)

COMPARSION OF FIELD AND FEYNMAN WEIGHTED CHARGE (ANTINEUTRINOS)

WEIGHTED CHARGE	ALL z LAB FRAME $z_i = E_i/E_H$ $5 \leq E_H \leq 40$ GeV	NORMALISED EVENT NOS.(BREIT FRAME)	STANDARD D - QUARK JETS
$Q_w \geq 0$	5247	4880	3499
$P = 0.2$ $Q_w < 0$	4753	5120	6361
$\langle Q_w \rangle$	0.09	-0.10	-0.25
σ rms			0.66
$Q_w \geq 0$	4815	4880	3601
$P = 0.5$ $Q_w < 0$	5185	5120	6259
$\langle Q_w \rangle$	0.03	-0.08	-0.15
σ rms			0.42
	$z \geq 0.1$		
$Q_w \geq 0$	4691	5040	3482
$P = 0.2$ $Q_w < 0$	5309	4960	5187
$\langle Q_w \rangle$	-0.01	-0.11	-0.19
σ rms			0.77
$Q_w \geq 0$	4630	5040	3486
$P = 0.5$ $Q_w < 0$	5370	4960	5183
$\langle Q_w \rangle$	-0.02	-0.09	-0.14
σ rms			0.53

TABLE 6.3 b)

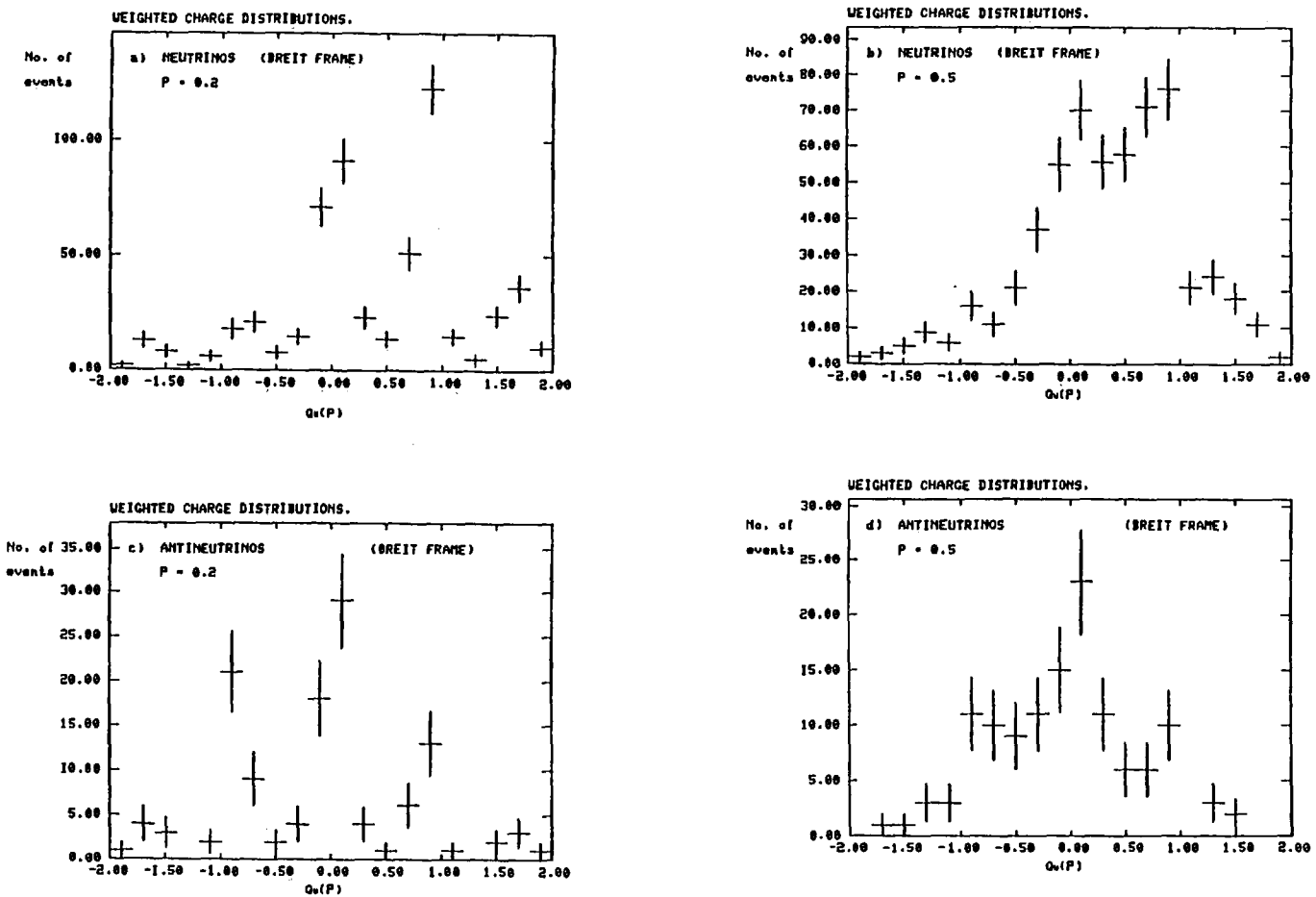
WEIGHTED CHARGE DISTRIBUTIONS.
No. of events
a) NEUTRINOS (BREIT FRAME)
P = 0.2
100.00
50.00
0.00
-2.00 -1.50 -1.00 -0.50 0.00 0.50 1.00 1.50 2.00
Qw(P)
WEIGHTED CHARGE DISTRIBUTIONS.
No. of events
b) NEUTRINOS (BREIT FRAME)
P = 0.5
90.00
80.00
70.00
60.00
50.00
40.00
30.00
20.00
10.00
0.00
-2.00 -1.50 -1.00 -0.50 0.00 0.50 1.00 1.50 2.00
Qw(P)
WEIGHTED CHARGE DISTRIBUTIONS.
No. of events
c) ANTINEUTRINOS (BREIT FRAME)
P = 0.2
35.00
30.00
25.00
20.00
15.00
10.00
5.00
0.00
-2.00 -1.50 -1.00 -0.50 0.00 0.50 1.00 1.50 2.00
Qw(P)
WEIGHTED CHARGE DISTRIBUTIONS.
No. of events
d) ANTINEUTRINOS (BREIT FRAME)
P = 0.5
30.00
25.00
20.00
15.00
10.00
5.00
0.00
-2.00 -1.50 -1.00 -0.50 0.00 0.50 1.00 1.50 2.00
Qw(P)

Fig. 6.7

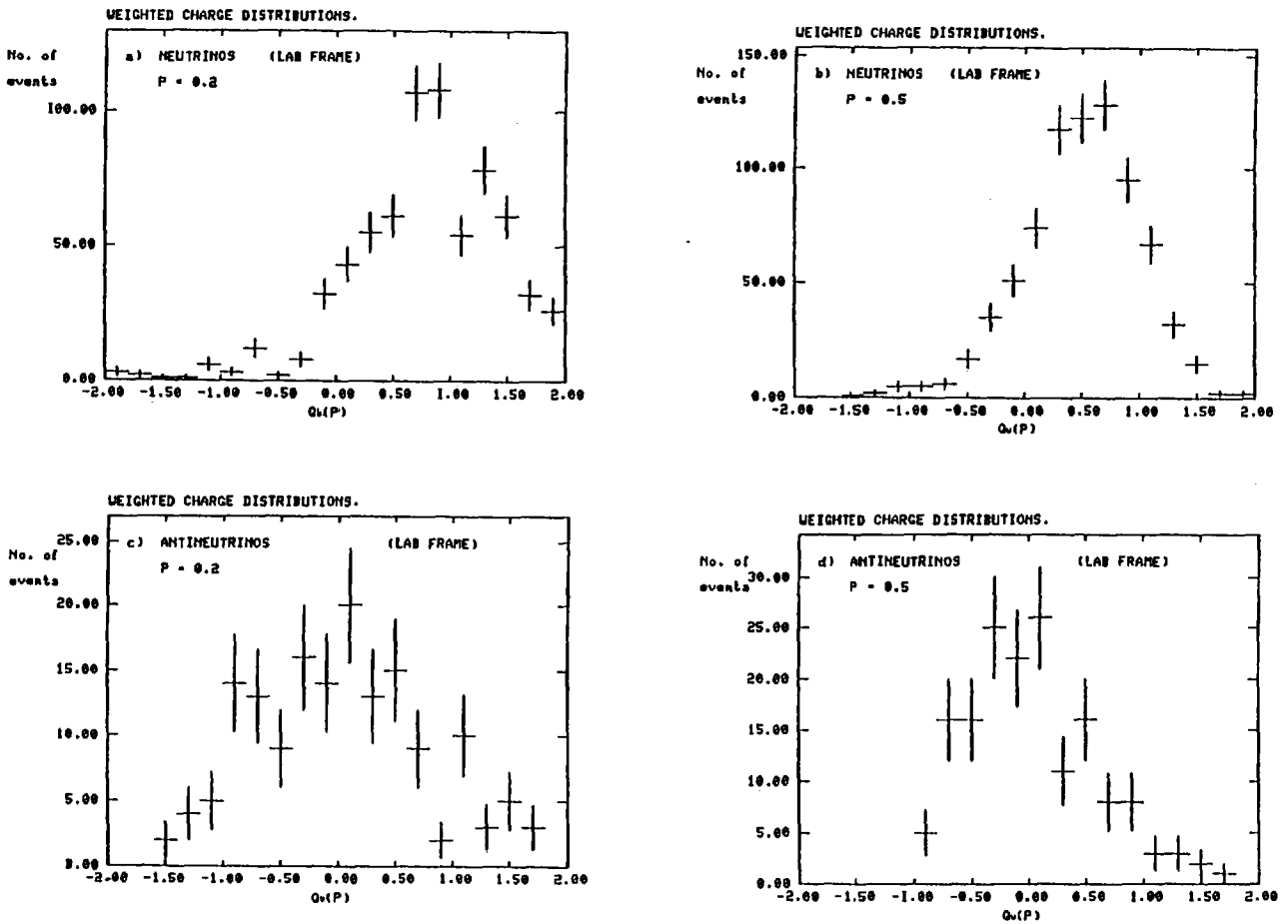
WEIGHTED CHARGE DISTRIBUTIONS.
a) NEUTRINOS (LAB FRAME)
P = 0.2
No. of events
100.00
50.00
0.00
-2.00 -1.50 -1.00 -0.50 0.00 0.50 1.00 1.50 2.00
Qν(P)
WEIGHTED CHARGE DISTRIBUTIONS.
b) NEUTRINOS (LAB FRAME)
P = 0.5
No. of events
150.00
100.00
50.00
0.00
-2.00 -1.50 -1.00 -0.50 0.00 0.50 1.00 1.50 2.00
Qν(P)
WEIGHTED CHARGE DISTRIBUTIONS.
c) ANTINEUTRINOS (LAB FRAME)
P = 0.2
No. of events
25.00
20.00
15.00
10.00
5.00
0.00
-2.00 -1.50 -1.00 -0.50 0.00 0.50 1.00 1.50 2.00
Qν(P)
WEIGHTED CHARGE DISTRIBUTIONS.
d) ANTINEUTRINOS (LAB FRAME)
P = 0.5
No. of events
30.00
25.00
20.00
15.00
10.00
5.00
0.00
-2.00 -1.50 -1.00 -0.50 0.00 0.50 1.00 1.50 2.00
Qν(P)

Fig. 6.8

that it is the weighted charge determined in the Breit frame which agrees more closely with the predictions of the jet model. It is also insensitive to the use of a minimum z cut whereas Qw (p) determined in the lab frame shows a marked disagreement with the jet model unless a z cut is imposed.

VI.5 Summary and Conclusions

The results presented here on the distribution of electric charge in the hadronic products of charged current neutrino interactions appear to be in reasonable agreement with the jet parameterization developed by Field and Feynman when examined in the Breit frame of the exchanged vector boson and struck quark. This, despite the statistical limitations of the data and the experimental uncertainties involved in the quantities calculated. The main experimental difficulty must be the transformation of the final state hadrons to the Breit frame due to the necessity of correcting all events for missing neutral energy. Also fermi motion and secondary re-interactions within the neon nucleus would tend to smear out the effects for individual events. Nevertheless there is some indication that a statistical separation of hadronic jets into catergories of differing quark origin can be made. The reliability of such a separation should improve as the event energy increases.

It has been pointed out by several sources, and for different reasons, that measuring the net charge of a hadronic jet does not provide any direct evidence for the existence of fractionally charged quarks. H.J. Lipkin [41] demonstrates that any such method would be unable to distinguish between integrally charged quarks or fractionally charged quarks since the effect of colour oscillations would be such

as to always give the appearance of 1/3 and 2/3 charged quarks as in the G/M model. Field and Feynman point out as stated above that any quark properties retained by a hadron jet must necessarily be modified by the mean antiquark properties of $q\bar{q}$ pairs in the sea. This contribution itself depends on the degree of symmetry of the sea and the number of flavours excited in the experimental energy range. More generally, it has recently been pointed out by Glashow [42] that results of 2/3 and - 1/3 obtained for u and d quarks respectively are independent of the actual quark charges and may be arrived at simply by assuming SU_3 symmetry of the sea. The u quark charge and d quark charge are then given by

$$Qu = 1 - a_1$$

$$Qd = - a_1$$

respectively, where a_1 is the probability of producing a $u\bar{u}$ pair from the sea. Looked at in this light a measurement of mean jet charge may be considered to give an indication of the quark composition of the sea in the energy range studied. The results obtained here are consistent with the assumption of Field and Feynman of a sea in which $s\bar{s}$ quarks are suppressed by 50% compared to $u\bar{u}$ and $d\bar{d}$. The weighted charge technique should be more appropriate for determining the actual quark properties but the current energy range is clearly too low to be able to make any meaningful statement.

References

1. B. Aubert et al., Phys. Rev. Lett. 33 (1974)984.
2. T. Eichten et al., Phys. Lett. 46B (1973)281;
   H. Deden et al., Nucl. Phys. B85 (1975)269.
3. P.C. Bosetti et al., Phys. Lett. 70B (1977)273.
4. P.C. Bosetti et al., Nucl. Phys. B142 (1978)1.
5. E. Fermi, Zeit.Physik 88 (1934)161;
   R.P. Feynman and M. Gell-Mann, Phys. Rev. 109 (1958)193.
6. S. Weinberg, Phys. Rev. Lett. 19 (1967)1264;
   A. Salam, Proc. 8th nobel symposium, Almqvist and Wiksell,
   Stockholm (1968)367;
   S. Weinberg, Phys. Rev. D5 (1972)1412.
7. F.J. Hasert et al., Phys. Lett. 46B (1973)138.
8. J.D. Bjorken, Phys. Rev. 179 (1969)1547.
9. R.P. Feynman, Phys. Rev. Lett. 23 (1969)1415;
   R.P. Feynman, "Photon-Hadron Interactions", Benjamin (1972).
10. C.G. Callan and D.G. Gross, Phys. Rev. Lett. 21 (1968) 211.
11. D.G. Gross and C.H. Llewellyn-Smith, Nucl. Phys. B14 (1969)337.
12. Gargamelle Users Handbook;
    CERN/EP/GM/ed 11 July 1977.
13. P. Jobin, CERN/EP/DHR 76-2 rev. 25 November 1976.
14. A. Benvenuti et al., Phys. Rev. Lett. 34 (1975)419;
    35 (1975)1199,1203,1249; 38 (1977)113;
    B.C. Barish et al.,Phys. Rev. Lett. 36 (1976)939;38 (1977)577.
15. R.J. Cence et al., Nucl. Inst. Meth. 138 (1976)2,245.
16. HYDRA application library long write-ups
    USBEMI 1-Nov-76
    THIRA 1-Nov-76

17. P.C. Bosetti et al., Phys. Lett. 73B (1978)380.

18. P.C. Bosetti et al., Phys. Lett. 76B (1978)505.

19. A.L. Grant, Nucl. Inst. Meth. 131 (1975)167.

20. R. Beuselinck et al., Nucl. Inst. Meth. 154 (1978)445.

21. L. Pape, private communication.

22. BEBC Users Handbook.

23. J. Blietschau et al., Phys. Lett. 58B (1975)361;60B (1976)207.

24. J. Von Krogh et al., Phys. Rev. Lett. 36 (1976)710;
P.C. Bosetti et al., Phys. Rev. Lett. 38 (1977)1248;
C. Baltay et al., Phys. Rev. Lett. 39 (1977)62.

25. M. Holder et al., Phys. Lett. 69B (1977)377.

26. M. Holder et al., Phys. Lett. 70B (1977)396.

27. M. Holder et al., Phys. Lett. 70B (1977)393;
T. Hansl et al.,Nucl. Phys. B142 (1978)381.

28. M.K Gaillard, B.W. Lee and J.L Rosner, Rev. Mod. Phys. 47 (1975)277;
J.D. Bjorken and S.L. Glashow, Phys. Lett. 11 (1964)255;
S.L. Glashow, J. Illiopoulos and L.Maiani, Phys. Rev. D2 (1970)1285.

29. N. Cabbibo, Phys. Rev. Lett. 10 (1963)531.

30. G.I.M., ref. 28.

31. R.D. Field and R.P. Feynman, Phys. Rev. D15 (1977)2590.

32. A. Pais and S.B. Treiman, Phys. Rev. Lett. 35 (1975)1206.

33. H. Goldberg, Phys. Rev. Lett. 39 (1977)1598.

34. M.K. Gaillard et al., ref. 28.

35. J. Von Krogh et al., ref. 24.

36. G. Hanson et al., Phys. Rev. Lett. 35 (1975)1609.

37. D. Linglin, R. Moller, invited talks at the 12th rencontre de Moriond, March 1977;
C. Bromberg et al., Phys. Rev. Lett. 38 (1977)1447.

38. H.L. Anderson et al., Phys. Rev. Lett. 36 (1976)1422;38 (1977)1450; E.M. Riordan et al., SLAC-PUB-1634 (1975).

39. R.D. Field and R.P. Feynman, Nucl. Phys. B136 (1978)1.

40. P.C. Bosetti et al., Nucl. Phys. B149 (1979)13.

41. H.J. Lipkin, Nucl. Phys. B155 (1979)104.

42. S.L. Glashow, proceedings of the Bergen neutrino conference 1979.

Acknowledgements

I would like to express my thanks to the many people whose help and encouragement in the production of this thesis and the work described herein has been invaluable:

To Professor I. Butterworth for giving me the opportunity to perform research in the HENP group of Imperial College and to the Science Research Council for their financial support.

My thanks are due to Dr. D.B. Miller for his supervision and advice and to Dr. K.W.J. Barnham who also provided much help and encouragement.

The scanning, measuring and computing staff are to be praised for their diligent efforts without which the data would not be available.

I wish to thank the EMI group at CERN for their hospitality and in particular Dr. D. Jacobs for his help and guidance.

My thanks go to Miss. L. Jones and Mrs. P. Byrne for their excellent typing of most of this thesis.

Finally I would like to thank all members of the HENP group with whom I have had many interesting informal discussions.